



저작자표시-비영리-변경금지 2.0 대한민국

이용자는 아래의 조건을 따르는 경우에 한하여 자유롭게

- 이 저작물을 복제, 배포, 전송, 전시, 공연 및 방송할 수 있습니다.

다음과 같은 조건을 따라야 합니다:



저작자표시. 귀하는 원저작자를 표시하여야 합니다.



비영리. 귀하는 이 저작물을 영리 목적으로 이용할 수 없습니다.



변경금지. 귀하는 이 저작물을 개작, 변형 또는 가공할 수 없습니다.

- 귀하는, 이 저작물의 재이용이나 배포의 경우, 이 저작물에 적용된 이용허락조건을 명확하게 나타내어야 합니다.
- 저작권자로부터 별도의 허가를 받으면 이러한 조건들은 적용되지 않습니다.

저작권법에 따른 이용자의 권리는 위의 내용에 의하여 영향을 받지 않습니다.

이것은 [이용허락규약\(Legal Code\)](#)을 이해하기 쉽게 요약한 것입니다.

[Disclaimer](#)

공학박사 학위논문

**Dosimetric Responses of  
Parallel Plate Ionization Chambers  
in a Magnetic Field**

평판형 이온전리함의  
자기장에서의 방사선량적 반응

2018 년 8 월

서울대학교 융합과학기술대학원

융합과학부 방사선융합의생명전공

이 재 기

A Dissertation for the Degree Doctor of Philosophy

**Dosimetric Responses of  
Parallel Plate Ionization Chambers  
in a Magnetic Field**

평판형 이온전리함의  
자기장에서의 방사선량적 반응

August 2018

Program in Biomedical Radiation Sciences  
Department of Transdisciplinary Studies  
Graduate School of Convergence Science and Technology  
Seoul National University

Jaegi Lee

평판형 이온전리함의  
자기장에서의 방사선량적 반응

지도 교수 예성준

이 논문을 공학박사 학위논문으로 제출함  
2018 년 4 월

서울대학교 융합과학기술대학원  
융합과학부 방사선융합의생명전공  
이 재 기

이재기의 공학박사 학위논문을 인준함  
2018 년 7 월

위원장                     최희동                    (인)

부위원장                     예성준                    (인)

위원                     이재성                    (인)

위원                     김창순                    (인)

위원                     남옥원                    (인)

# Abstract

Radiation dosimetry has been an important issue since the discovery of X-ray. These days, the primary standards dosimetry laboratories (PSDLs) and international agencies (e.g., IAEA, WHO) disseminate the international calibration standards to users through a network of the secondary standards dosimetry laboratories (SSDL). For this purpose, various dosimeters and equipment have been developed to assure the quality of calibration traceability and accuracy. Among them, an ionization chamber has become the most relevant dosimeter for measurements of radiation doses due to its high precision and reliability. Therefore, ionization chambers have been used to provide reference dosimetry calibrations for radiotherapy.

Dosimetry for magnetic resonance imaging (MRI)-guided radiotherapy has been an emerging issue in the medical radiation society. Currently developing MRI-guided radiotherapy machines adopt Co-60 or pulsed X-rays with a magnetic field of 0.35 to 1.5 T either perpendicular or parallel to the incident photon beams. The magnetic field influences the trajectories of secondary charged particles through the action of the Lorentz force such that the dose distribution in the sensitive volume of ionization chamber can be altered. Since PSDLs or SSDLs calibrate ionization chambers without a magnetic field, radiation dosimetry in a magnetic field using the ionization chambers needs an additional magnetic field correction factor. Since MRI-guided radiotherapy is still under development, these magnetic field correction factors are often calculated using Monte Carlo (MC) radiation transport codes integrated with an electromagnetic module.

In order to evaluate the accuracy of electron transport algorithms of the MC codes at a static magnetic field of 0.35 to 3.0 T, the Fano cavity theorem was tested for mono-energetic electrons with energies ranging from 0.01 to 3 MeV. Four general-purpose Monte Carlo codes (EGSnrc, PENELOPE, MCNP6, and Geant4) were validated for this purpose. With transport parameters carefully selected, PENELOPE and MCNP6 could achieve the accuracy within 1.0% and 0.4%, respectively. Geant4 showed the accuracy within 1.7% except in 3.0 T. The accuracy of EGSnrc with the enhanced electromagnetic field macros was within 0.2%. Owing to its superior accuracy, the following simulations in this study were performed using EGSnrc with the enhanced electromagnetic field macros.

The purpose of this study was to calculate magnetic field correction factors of ionization chambers for combinations of various energies of photon beams and various strengths of magnetic fields either perpendicular or parallel to the incident photon beam. Parallel plate ionization chambers are usually used to measure the absorbed dose to water at low-energy beams for radiotherapy. It is advantageous when measuring surface doses to water and doses in a high dose gradient region, and has an easy design customization and fabrication. Three commercial parallel plate ionization chambers were selected to simulate the response variations in a magnetic field. They included the IBA NACP-02, PTW Roos (Type 34001), and Exradin A11. These chambers have the same height but different radii of the sensitive volume. For radiation sources, Eldorado 6 for a Co-60 beam as well as Varian Clinac<sup>®</sup> series for 6, 10, and 15 MV photon beams were adopted. A spectral source for a 7 MV photon beam adopted in the previous study for the MRI-guided radiotherapy machine was

also simulated. The strengths of magnetic field ranged from 0.35 T to 1.5 T, which was either perpendicular or parallel to the photon beam.

The responses of the parallel plate ionization chambers in magnetic fields increased by up to 18% compared to those without a magnetic field. The magnetic field correction factors of the parallel plate ionization chambers were 0.85 to 1.0. Large beam quality dependence and variation occurred in cases of the perpendicular orientation. The larger beam quality was applied, the smaller amount of magnetic field corrections were needed. Except for a Co-60 beam, the largest magnetic field correction occurred around 1.0 T rather than 1.5 T, which was the largest magnetic field strength in this study. In cases of the parallel orientation, only small magnetic field corrections less than 1% were needed.

The MC calculations for segmentation of the sensitive volume of the ionization chamber showed a strong heterogeneity of the absorbed dose due to helical motions of secondary electrons in the sensitive volume. The sensitive volume of the Roos chamber was in silico modified by half or twice the radius or height to figure out the relationship between the sensitive volume and magnetic field correction. The ionization chamber with a small sensitive volume was less influenced by a magnetic field.

**Keyword:** Parallel plate ionization chambers, magnetic field correction, electron transport, Monte Carlo simulation, Fano cavity theorem

**Student Number :** 2011-22779

# List of Tables

<b>Table 1.</b> Summary of magnetic resonance-linear accelerator (MR-linac) in the world. .....	9
<b>Table 2.</b> Dimensions for simulation geometry of three parallel plate ionization chambers.....	15
<b>Table 3.</b> Physical dimensions of Monte Carlo simulations for different electron energies. Continuous slowing down approximation (CSDA) ranges in the National Institute of Standards and Technology (NIST) stopping-power and range tables for electrons (ESTAR) database were used.....	20
<b>Table 4.</b> Transport parameters applied to the simulations with condensed history algorithms of the four codes. ....	21
<b>Table 5.</b> Comparison of magnetic field correction factors ( $k_B^Q$ ) for the NACP-02. Perpendicular and parallel magnetic field orientations to the beam direction were denoted as ‘ $\perp$ ’ and ‘ $\parallel$ ’, respectively.....	49
<b>Table 6.</b> Comparison of magnetic field correction factors ( $k_B^Q$ ) for the Roos. Perpendicular and parallel magnetic field orientations to the beam direction were denoted as ‘ $\perp$ ’ and ‘ $\parallel$ ’, respectively.....	50
<b>Table A1.</b> Polarity correction factors ( $P_{pol}$ ) for the ionization chambers with graphene electrodes and with carbon-loaded polyethylene electrodes, and the NACP-02.....	95

**Table A2.** Ion recombination correction factors ( $P_{\text{ion}}$ ) for the ionization chambers with graphene electrodes and with carbon-loaded polyethylene electrodes, and the NACP-02..... 96

# List of Figures

- Figure 1.** International measurement system for radiation dosimetry. .... 3
- Figure 2.** MR-linac: ViewRay MRIdian<sup>®</sup> (a), Elekta<sup>™</sup> Unity MR-linac (b), Aurora RT<sup>™</sup> (c), and Australian MRI-Linac (d). Red arrows are the orientations of magnetic field, and blue arrows are the beam directions. .... 8
- Figure 3.** Full head geometries of linac (a) and Co-60 machine (b) were modeled to generate phase spaces at the surface of water. Collimated photon beams based on these phase spaces were assumed to be incident on a parallel plate ionization chamber in water (not scaled). .... 12
- Figure 4.** Simulation geometries for three parallel plate ionization chambers: the NACP-02 (a), Roos (b), and Exradin A11 (c). Red boxes are the sensitive volume of the parallel plate ionization chambers. The figures are relatively scaled. .... 14
- Figure 5.** Schematic diagrams for the Fano cavity test in a magnetic field. Black arrows are simplified electron trajectories. The original Fano cavity theorem was presented in (a), and the simplified model of the Fano cavity theorem by the reciprocal theorem was presented in (b), and the adapted Fano cavity theorem in a magnetic field was presented in (c). .... 18
- Figure 6.** Schematic diagram of electron transport simulations for Fano cavity test (not scaled). Wall thickness ( $t_{\text{wall}}$ ) was 1.4 times the continuous slowing down approximation (CSDA) range in graphite, and gas thickness ( $t_{\text{gas}}$ ) was 0.2 or 2 cm. The radius of geometry ( $r$ ) was 1.4 times the CSDA range in gas material ( $\text{CSDA}_{\text{gas}}$ ). The density of gas material was 1000 times lower than that of wall material. Isotropic and uniform mono-energetic electrons per unit mass were generated at the central axial line of the cylindrical geometry (denoted as a yellow line). .... 19

**Figure 7.** Results of the Fano cavity test using EGSnrc. The EM ESTEPE of 0.02 (a) and 0.01 (b), and the EMULMT of 0.001 (c) were used under the default electromagnetic field macro, `emf_macros.mortran`. The enhanced electromagnetic field (EEMF) macro (Malkov and Rogers, 2016), `EEMF_macros.mortran`, was applied (d)..... 32

**Figure 8.** Results of Fano cavity test in a magnetic field for the gas thickness ( $t$ ) of 0.2 cm (a) and 2 cm (b). Relative differences in dose per particle between Monte Carlo simulation and theoretical value are shown as a function of magnetic field strength in Tesla for four electron energies. Statistical uncertainties are given with a coverage factor  $k = 1$ . ..... 33

**Figure 9.** Results of the Fano cavity test using PENELOPE. Different DSMAX values of 0.02 cm (a), 0.01 cm (b), and 1  $\mu\text{m}$  (c) were applied. The other parameters were benchmarked with the previous study (Sempau and Andreo, 2006). A single scattering option without a magnetic field was also simulated for different energies of electrons (d). Statistical uncertainties were smaller than the symbol or shown as error bars with a coverage factor  $k = 2$ . ..... 35

**Figure 10.** Results of the Fano cavity test using MCNP6 code. ITS energy indexing and two different *efac* values of 0.917 (a) and 0.99 (b). Default energy indexing and *efac* value of 0.99 were applied in (c). The default ESTEP value was used in (a)-(c). With the default energy indexing and *efac* value of 0.99, ESTEP of 80 for 1 and 3 MeV was applied in (d), and ESTEP of 90 for 1 MeV and ESTEP value of 70 for 3 MeV were applied in (e). A single scattering option was turned on without a magnetic field in (f). Statistical uncertainties were smaller than the symbol or shown as error bars with a coverage factor  $k = 2$ . ..... 38

**Figure 11.** Results of the Fano cavity test using Geant4. The default parameters were used in (a), and the parameters from the previous study (O'Brien et al, 2016) were

benchmarked in (b). Statistical uncertainties were smaller than the symbol or shown as error bars with a coverage factor  $k = 2$ . ..... 40

**Figure 12.** Monte Carlo calculated beam quality conversion factors ( $k_Q$ ) for the NACP-02 (a), Roos (b), and Exradin A11 (c). Statistical uncertainties are given with a coverage factor  $k = 1$ . ..... 43

**Figure 13.** Doses to the sensitive volume of the chambers ( $D_{\text{chamber}}$ ) for the NACP-02 (a), Roos (b), and Exradin A11 (c). A magnetic field of 0.35, 0.5, 1.0 and 1.5 T was perpendicular to the incident beam direction of 5 different energies. All the responses were normalized by the corresponding values of no magnetic field. Statistical uncertainties were smaller than the symbols with a coverage factor  $k = 1$ . ..... 45

**Figure 14.** Doses to water ( $D_{\text{water}}$ ). A magnetic field of 0.35, 0.5, 1.0 and 1.5 T was perpendicular to the incident beam direction of 5 different energies. All the responses were normalized by the corresponding values of no magnetic field. Statistical uncertainties were given with a coverage factor  $k = 1$ . ..... 46

**Figure 15.** Correction factors ( $k_B^Q$ ) vs. photon beam energies for magnetic fields perpendicular to the beam direction ((a), (c), and (e)) and for magnetic fields parallel to the beam direction ((b), (d), and (f)). Statistical uncertainties were smaller than the symbols or given with a coverage factor  $k = 1$ . ..... 48

**Figure 16.** Relative dose distribution of 6 MV beam inside the sensitive volume of the Roos chamber for 0.35 T (a), 0.5 T (b), 1.0 T (c), and 1.5 T (d). Diagrams from left to right represent the four layers of the sensitive volume of the chamber from entrance of the beam to exit. A photon beam was incident from back of the figure toward the front, and a magnetic field was assumed to +Y axis (to 90°) so that the Lorentz force of electrons was mainly directed to +X axis (to 0°) in the figure. The average statistical uncertainty was 0.55%, and the maximum statistical uncertainty was 0.85% with a coverage factor  $k = 1$ . ..... 52

**Figure 17.** Same as Figure 15 but for a 15 MV beam. The average statistical uncertainty was 0.56%, and the maximum statistical uncertainty was 0.76% with a coverage factor  $k = 1$ . ..... 53

**Figure 18.** Variation of magnetic field correction factors,  $k_B^Q$  on different dimensions of the sensitive volume: height ( $h$ ) is 0.1, 0.2, and 0.4 cm, and radius ( $r$ ) is 0.5, 0.75, and 1.0 cm for Co-60 (a) and 7 MV (b) in four strengths of perpendicular magnetic fields. The Roos chamber has 0.2 cm height and 0.75cm radius (red solids). ..... 55

**Figure A1.** Cutting plane (a) and schematic diagram (b) of the NACP-02 geometry. The light orange parts are made of poly(methyl methacrylate) (PMMA), and the dark gray parts are made of graphite. The light blue color is an air cavity, and the red rectangle is the sensitive volume of the NACP-02. For the water-proof, a thin resin polyethylene terephthalate (PET) film covers the top of the entrance window... 70

**Figure A2.** 3D printing process: Computer-aided design (CAD) for generating STL file (a), G-code generator for 3D printing (b), and fused deposition modeling (FDM) 3D printing (c). ..... 72

**Figure A3.** Schematic images of the patterned monolayer graphene. .... 74

**Figure A4.** Diagram of top electrode (a), bottom electrodes (b)-(c) of the hand-made ionization chambers with graphene and carbon-loaded polyethylene electrodes. 75

**Figure A5.** Graphene electrodes on a polyethylene terephthalate (PET) plate after metal coating using shadow masks for a wire connection..... 76

**Figure A6.** Assembly diagram of the 3D-printed graphene ionization chamber (a); the front view of the ionization chamber (b); the side view of the ionization chamber (c). ..... 78

**Figure A7.** X-RAD 320 irradiator for a kilo voltaic x-ray beam (a) and clinical medical linear accelerator for mega voltaic photon and electron beams (b)..... 81

**Figure A8.** Leakage current of the graphene ionization chamber at an applied voltage of +300 V after zeroing during 50 seconds. It was almost negligible for the collected charge. .... 83

**Figure A9.** Linearity between the absorbed dose and the collected charge of the ionization chambers with graphene electrodes (a)-(b) and with carbon-loaded polyethylene electrodes (c)-(d), and the NACP-02 (e) for a kilo voltaic x-ray beam of 200 kVp. .... 86

**Figure A10.** Linearity between the absorbed dose and the collected charge of the ionization chambers with graphene electrodes (a)-(b) and with carbon-loaded polyethylene electrodes (c)-(d), and the NACP-02 (e) for mega voltaic photon and electron beams. .... 87

**Figure A11.** Dose rate dependence of the ionization chambers with graphene electrodes (a)-(b) and with carbon-loaded polyethylene electrodes (c)-(d), and the NACP-02 (e) for a kilo voltaic x-ray beam of 200 kVp. .... 88

**Figure A12.** Dose rate dependence of the ionization chambers with graphene electrodes (a)-(b) and with carbon-loaded polyethylene electrodes (c)-(d), and the NACP-02 (e) for mega voltaic photon and electron beams. .... 89

**Figure A13.** Current-voltage characteristics of the ionization chambers with graphene electrodes (a)-(b) and with carbon-loaded polyethylene electrodes (c)-(d), and the NACP-02 (e) for a kilo voltaic x-ray beam of 200 kVp. .... 91

**Figure A14.** Current-voltage characteristics of the ionization chambers with graphene electrodes (a)-(b) and with carbon-loaded polyethylene electrodes (c)-(d), and the NACP-02 (e) for mega voltaic photon and electron beams..... 92

**Figure A15.** Jaffé plots of the ionization chambers with graphene electrodes (a)-(b) and with carbon-loaded polyethylene electrodes (c)-(d), and the NACP-02 (e).. 93

# Table of Contents

<b>Abstract.....</b>	<b>i</b>
<b>List of Tables.....</b>	<b>iv</b>
<b>List of Figures .....</b>	<b>vi</b>
1. Introduction .....	1
2. Materials and Methods.....	7
2.1. MR-Linac for Radiotherapy .....	7
2.2. Simulations of Linac and Co-60 Irradiator .....	10
2.3. Parallel Plate Ionization Chambers.....	13
2.4. Fano Cavity Tests in Magnetic Fields .....	16
2.4.1. EGSnrc.....	22
2.4.2. PENELOPE.....	22
2.4.3. MCNP6 .....	23
2.4.4. Geant4.....	25
2.5. Beam Quality Specifier and Beam Quality Conversion Factors .....	26
2.6. Magnetic Field Correction Factors .....	28
2.7. Dose Heterogeneity in the Sensitive Volume of the Chambers in a Magnetic Field.....	28
3. Results.....	30
3.1. The Fano Cavity Tests .....	30
3.1.1. EGSnrc.....	30
3.1.2. PENELOPE.....	34

3.1.3. MCNP6 .....	36
3.1.4. Geant4.....	39
3.2. Summary of the Fano Cavity Tests .....	41
3.3. Simulations of the Linac and Co-60 Beams and Beam Quality Conversion Factors .....	42
3.4. Response of Parallel Plate Ionization Chambers in a Magnetic Field and Magnetic Field Correction Factors.....	44
3.5. Dose Heterogeneity within the Sensitive Volume of Chamber in a Magnetic field .....	51
4. Discussion .....	56
5. Conclusions .....	63
<b>Appendix A. Feasibility of a Parallel Plate Ionization Chamber with Graphene Electrodes .....</b>	<b>65</b>
<b>Bibliography .....</b>	<b>98</b>
<b>Abstract in Korean .....</b>	<b>108</b>

## 1. Introduction

Radiation dosimetry is very important in radiation medicine and industry and public health. In order to measure radiation doses accurately, development of an appropriate dosimeter has been pursued. Among various radiation dosimeters, an ionization chamber has become the most relevant dosimeter for the measurements of radiation doses due to its high precision and reliability (1). Therefore, an ionization chamber has been used to provide an accurate and consistent absorbed dose with a calibration factor traceable to the international metrology standards.

The primary standard dosimetry laboratories (PSDLs) designated by the governments maintain primary radiation standards by definition (2). They offer calibrations traceable to their primary standards to the secondary standard dosimetry laboratories (SSDLs). The radiation users calibrate their dosimeters by SSDL designated by competent national authorities (Figure 1). For radiotherapy beams, two types of ionization chambers are usually used for reference dosimetry; cylindrical and parallel plate ionization chambers. Generally, cylindrical ionization chambers (e.g., Farmer-type ionization chambers) are considered to measure radiation doses in water for the wide energy range of radiotherapy beams. On the contrary, the use of parallel plate ionization chambers for reference dosimetry of high-energy photon beams was not recommended due to its long-term instability (3). However, the parallel plate ionization chamber with its thin and flat entrance window would still be advantageous over the Farmer-type ionization chamber for the measurements of the surface or build-up region dose (4). Also, well-guarded parallel

plate ionization chambers are preferred for electron beams with incident energies of 10 MeV or less (5).

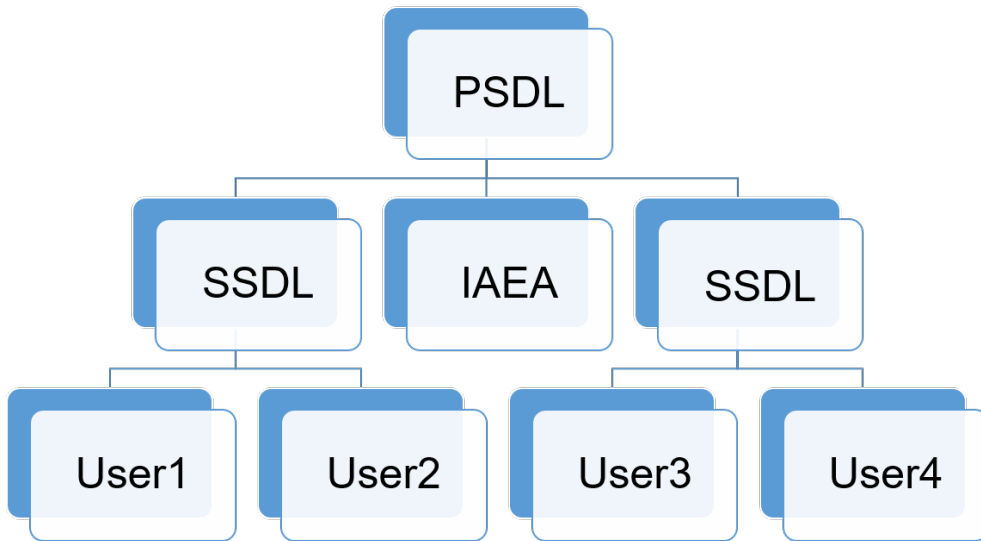


**Figure 1.** International measurement system for radiation dosimetry (Modified from <http://www-naweb.iaea.org/nahu/DMRP/ims.html>).

Recently, a new radiotherapy modality integrated with magnetic resonance imaging (MRI) has been developing worldwide (6-9). To date, there are two types of MRI-guided radiotherapy machines being developed over the world: a magnetic field perpendicular (6, 8) or parallel (7, 9) to the incident photon beam direction. With simultaneous MRI during radiation beam delivery, the tumor could be selectively targeted without additional ionizing radiation exposure. The first MRI-guided radiotherapy machine released in the clinic used three Co-60 sources combined with a 0.35 T magnetic field that can avoid the technical difficulty of accommodating electromagnetic interference with linear accelerator (linac) machinery (8). The magnetic resonance-linac (MR-linac) has been also released with a 6 or 7 MV photon beam integrated with a 0.35 or 1.5 T magnetic field. The MR-linac system with high energy photon beams would be advantageous in delivering therapeutic doses to the deep-sited target efficiently so that several recent studies have tried to show the feasibility of short waveguide for bore-type MR-linac with high-energy photon beams up to 10 MV (10-12).

Monte Carlo codes for radiation transport have become an essential tool for clinical dosimetry. In order to verify new and updated features in the Monte Carlo codes, several authors conducted comparison studies (13-20). Several general-purpose Monte Carlo codes, such as EGSnrc, PENELOPE, MCNP6 and Geant4, have implemented charged particle transport in electromagnetic fields into their own sophisticated condensed history algorithms (21-24). As a default, each code maximizes the step size while maintaining accuracy with its own sophisticated algorithm. The step size control option was also available for these codes, however, their simulation accuracy in magnetic fields has not been fully validated yet.

The Fano cavity theorem has played an important role in verifying the accuracy of the Monte Carlo codes in heterogeneous density without a magnetic field (25). It states that charged particle fluences are conservative in density variations from point to point under charged particle equilibrium and uniform atomic properties. A few studies investigated the accuracy of the Monte Carlo codes using this theorem (26-29). However, classical Fano cavity theorem is not directly applicable for charged particle transport in the presence of magnetic fields (30). With the addition of two alternative assumptions of the charged particle isotropy and the density-scaled magnetic field, the Fano cavity theorem is still available for charged particle transport even in magnetic fields (30, 31).

Up to now, there have been a few studies that had attempted to apply the Fano cavity theorem to verify the accuracy of Monte Carlo codes in magnetic fields (32-36). However, no comprehensive comparison study for the aforementioned codes has been performed yet to estimate their accuracy in magnetic fields. Moreover, the Fano cavity theorem in the presence of magnetic field has not been fully tested yet for the MCNP series. In this study, the accuracy of electron transport algorithms namely EGSnrc, PENELOPE, MCNP6, and Geant4 in magnetic fields using the Fano cavity theorem was evaluated before the dosimetric response of the parallel plate ionization chamber was investigated.

The deflection of secondary electrons caused by the Lorentz force in a magnetic field could alter the dose distribution in patients as well as the response of ionization chambers. In order to accurately calculate the dose from the response of an air-filled ionization chamber in a magnetic field, the need of an additional magnetic field correction factor for reference dosimetry was reported (37, 38). When the directions

of the magnetic field, incident beam, and chamber axis were mutually orthogonal, the response of the Farmer-type ionization chambers was increased by 8%-11% in 1.0 T, and by 3%-5% in 1.5 T (33, 35-40). It was also reported that the change in Farmer-type ionization chamber readings could be within 1.3% for the magnetic field parallel to the chamber axis (33, 35, 36, 40). In addition, the response of the Farmer-type ionization chambers was changed within 1.0% for the magnetic field parallel to the beam direction (35, 36, 39, 40).

Recent studies reported that the magnetic field correction of parallel plate ionization chambers was up to 8.9% for a 7 MV beam in 1.5 T (40, 41). Furthermore, the use of parallel plate ionization chambers for reference dosimetry of high-energy photon beams was not recommended because their long-term stability did not meet the level of reference dosimetry (3). However, the parallel plate ionization chamber with its thin sensitive volume would be still advantageous over the Farmer-type ionization chamber when measuring the steep dose variation of the buildup region especially in a magnetic field (42). Thus, a further study on the response of the parallel plate ionization chambers in a magnetic field is still worthwhile. In this study, variations in the responses of three types of parallel plate ionization chambers were investigated in numerous combinations of magnetic field strengths and orientations, and photon beam energies that might cover all MRI-guided radiotherapy machines currently available and under development.

## **2. Materials and Methods**

### **2.1. MR-Linac for Radiotherapy**

Four MR-linac machinery systems have been developing (Figure 2). Table 1 summarized the characteristics of each MR-linac system in the world. A radiotherapy machine of three Co-60 sources equipped with 0.35 T MRI system has been released prior to the MR-linac system (8). As for the MR-linac system being developed (6, 7, 9), a magnetic field is either perpendicular or parallel to the incident beam direction. Furthermore, the MR-linac system has a unique MRI system with different strengths of magnetic fields, such as 0.35, 0.5, 1.0, and 1.5 T. However, either a 6 or 7 MV photon beam has been widely adopted. We considered all combinations of magnetic field strengths and orientations, and photon beam energies mentioned above. In addition, 10 and 15 MV photon beams were considered to investigate the impact of higher-energy photon beams on the magnetic field correction.

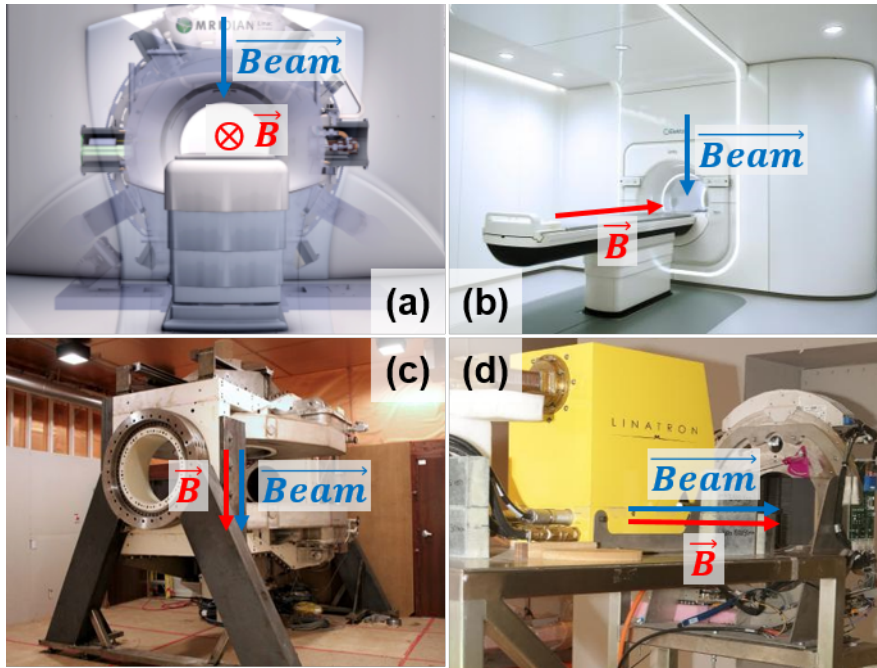


**Figure 2.** MR-linac: ViewRay MRIdian<sup>®</sup> (a), Elekta<sup>™</sup> Unity MR-linac (b), Aurora RT<sup>™</sup> (c), and Australian MRI-Linac (d). Red arrows are the orientations of magnetic field, and blue arrows are the beam directions. (<http://medicaldevicedaily.com/>, <https://www.elekta.com/>, <http://www.mp.med.ualberta.ca/>, and <https://www.dailytelegraph.com.au/>).

**Table 1.** Summary of magnetic resonance-linear accelerator (MR-linac) in the world.

	ViewRay MRIdian <sup>®</sup>	Elekta <sup>™</sup> Unity MR-linac	Aurora <sup>™</sup>	Australian MRI-Linac
B-field strength	0.35 T	1.5 T	0.5 T	1.0 T
Beam energy	Co-60/6 MV	7 MV	6 MV	6 MV
Bore size	70 cm	70 cm	85 cm	82 cm
In-line imaging	Yes	Yes	Yes	Yes
B-field orientation	$\vec{B} \perp \overrightarrow{Beam}$	$\vec{B} \perp \overrightarrow{Beam}$	$\vec{B} \parallel \overrightarrow{Beam}$	$\vec{B} \parallel \overrightarrow{Beam}$

## 2.2. Simulations of Linac and Co-60 Irradiator

A full head of the medical linac (Varian Clinac<sup>®</sup>) for 6, 10, and 15 MV photon beams was modeled by the BEAMnrc system (see Figure 3(a)). We started using the incident beam parameters from the literature where the same linac as ours was modeled (43). From the initial parameter, we tuned the incident electron energy of parallel circular beams and the full width at half-maximum of their Gaussian radial distribution in order to match the percent depth-doses and cross-beam profiles of the golden beam data from the vendor. The directional bremsstrahlung splitting (DBS) technique was applied to improve the simulation efficiency (44). The splitting field radius was 11 cm for a field size of  $10 \times 10$  cm<sup>2</sup> at a source to surface distance (SSD) of 100 cm. The DBS splitting number was set to 500. Phase spaces from the linac modeling were obtained at an SSD of 100 cm. Photon energy spectra for a field size of  $10 \times 10$  cm<sup>2</sup> at an SSD of 100 cm were extracted from the phase spaces using the BEAMDP user code. Collimated photon beams of a field size of  $10 \times 10$  cm<sup>2</sup> using these photon energy spectra were modeled by the egs\_chamber code because the full BEAMnrc model was inefficient for all of the required ionization chamber simulations and using the photon spectrum would not produce any noticeable differences for these energies and photon beam sizes. The egs\_chamber code will be further described in the following section. The transport threshold and cutoff energies (i.e., AE and Ecut for electron, AP and PCUT for photon) were set to 521 keV for electrons and 10 keV for photons. The 7 MV spectrum of Elekta<sup>™</sup> MR-linac originally generated by Ahmad et al. (45) using the Geant4 code was adopted in this study. This beam refers to as a 7 MV beam. For a Co-60 beam, the Eldorado 6 model

originally created and upgraded by G. Mora et al. (46) and Muir et al. (47) was used in this study. The same approach and codes as in the above linac simulation were employed to generate a collimated Co-60 beam (see Figure 3(b)) of a field size of  $10 \times 10 \text{ cm}^2$  at an SSD of 80.5 cm. The SSD for the collimated Co-60 beam using these spectra was extended to 100 cm for the recent version of the Co-60 irradiator. The same transport threshold and cutoff energies as used by G. Mora et al. (46) were set in this study.

This two-step simulation with variance reduction techniques was only practical to calculate the responses of three types of ionization chambers for numerous combinations of magnetic field strengths and orientations, and photon beam energies. Otherwise, the simulation of the linac and ionization chamber geometries at once was not virtually practical in terms of the computing time even with variance reduction techniques.

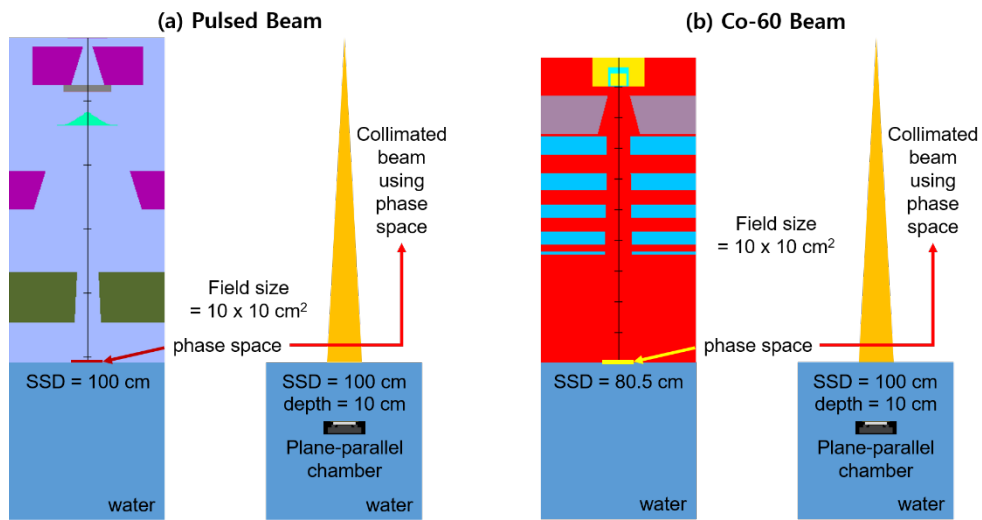


**Figure 3.** Full head geometries of linac (a) and Co-60 machine (b) were modeled to generate phase spaces at the surface of water. Collimated photon beams based on these phase spaces were assumed to be incident on a parallel plate ionization chamber in water (not scaled).

### **2.3. Parallel plate ionization chambers**

Three commercial parallel plate ionization chambers were selected for this study. They included the IBA NACP-02, PTW Roos (Type 34001), and Exradin A11. These chambers have the same height but different radii of the sensitive volume. Both collecting and polarizing electrodes of the chambers are made of graphite. In this study, the simulation details of the NACP-02 were adopted from the previous reports (3, 48, 49). The simulation geometry of the Roos was based on the technical specifications from the manufacturer. The data of the Exradin A11 modeled by Erazo et al. (50) was used. The density of graphite in the polarizing and collecting electrodes was modified using the report by Gomá et al. (51) for a coincidence to the previous data (3). The dimensions for the simulation geometry of the three parallel plate ionization chambers used in this study are given in Figure 4 and Table 2. The three parallel plate ionization chambers were drawn using the egs++ geometry package in the EGSnrc C++ class library (52).

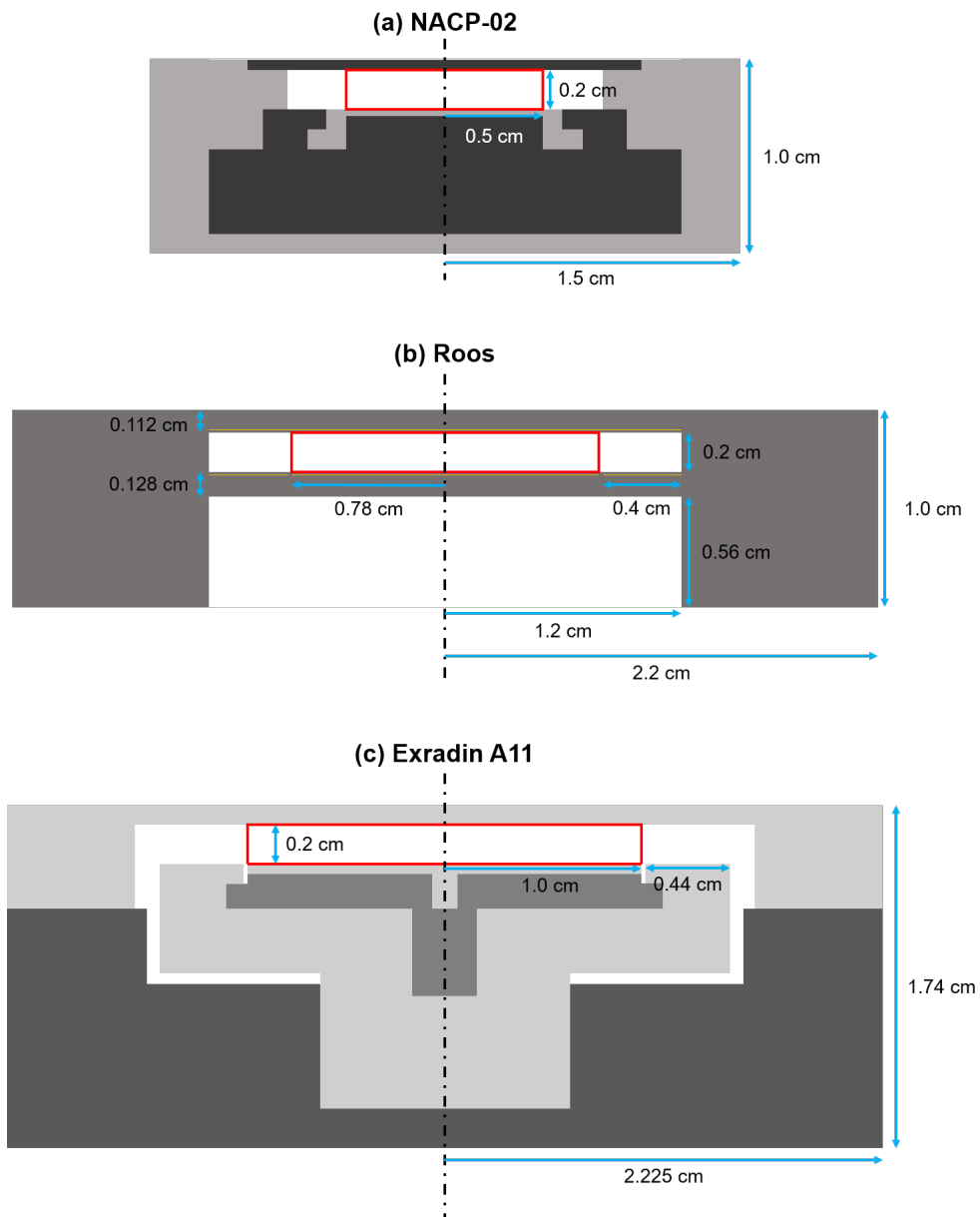


**Figure 4.** Simulation geometries for three parallel plate ionization chambers: the NACP-02 (a), Roos (b), and Exradin A11 (c). Red boxes are the sensitive volume of the parallel plate ionization chambers. The figures are relatively scaled.

**Table 2.** Dimensions for simulation geometry of three parallel plate ionization chambers.

	Sensitive volume (cm <sup>3</sup> )	Sensitive volume radius (cm)	Guard ring width (cm)	Electrode spacing (cm)
NACP-02	0.16	0.5	0.325	0.2
Roos	0.35	0.75	0.4	0.2
Exradin A11	0.62	1.0	0.44	0.2

## 2.4. Fano Cavity Tests in Magnetic Fields

Originally, the Fano cavity theorem states that the fluence of the secondary charged particles in an infinite medium is conservative after a uniform photon beam is incident on the medium (25) (Figure 5(a)). However, it is difficult to satisfy this condition without eliminating photon attenuation or the infinite size of the phantom. Instead, we benchmarked alternative simplified methods of Fano cavity test from the previous studies without photons (28, 34) (Figure 5(b)-(c)). Figure 6 showed the simulation geometry for the Fano cavity test. A circular gas disk was sandwiched between two circular solid wall disks, each of which having a radius that is 1.4 times the continuous slowing down approximation (CSDA) range in gas material. The height of the wall and gas region was set to 1.4 times the CSDA range in wall material and 0.2 cm, respectively. The thickness of 2 cm for the gas region without changing the wall region was also simulated only for EGSnrc. In order to satisfy the assumption of uniform atomic properties in the Fano cavity theorem, the elemental compositions of the gas and wall materials were assumed to be carbon. The density of the gas region was set to be 1000 times lower than the wall region. The values of the CSDA range were obtained from the National Institute of Standards and Technology (NIST) stopping-power and range tables for electrons (ESTAR) database (53). By the reciprocity theorem, a uniform electron line source per unit mass at the central axis of the cylindrical simulation geometry could be substituted for the uniform photon source incident on the top or bottom of the geometry. In order to satisfy the Fano cavity theorem in a magnetic field, electrons were isotropic at each point of the line (30). Mono-energetic electrons of 0.01, 0.1, 1, and 3 MeV were

selected as the source. Table 3 displays the physical dimensions for a Fano cavity test in this study. A uniform magnetic field was applied to the whole simulation geometry perpendicular to the central axis. The magnetic field strength was assumed to be 0, 0.35, 1.0, 1.5, and 3.0 T.

The recent versions of general-purpose Monte Carlo codes, such as EGSnrc 2017, PENELOPE 2014, MCNP6.1, and Geant4.10.03 have implemented their own electromagnetic modules. In magnetic field strengths of 0, 0.35, 1.0, 1.5, and 3.0 T, the dose per particle in the gas region ( $D$ ) was simulated using four Monte Carlo codes. As a theoretical value, the number of electrons per unit mass ( $I$ ) times the initial energy ( $E_0$ ) was manually calculated because each point in the line source in the gas region equally contributed to the dose to the gas region according to the Fano cavity theorem. Relative differences between  $D$  and  $IE_0$  were evaluated as an accuracy index of the Monte Carlo codes for electron transport in magnetic fields,

$$\text{Relative Difference} = \left( \frac{D}{IE_0} - 1 \right) \times 100\%. \quad (1)$$

In common, the electron transport cutoff was 1 keV, and no bremsstrahlung x-ray was generated by setting the photon transport cutoff higher than a simulated electron energy for EGSnrc, MCNP6, and Geant4. In PENELOPE, bremsstrahlung x-rays deposit their energy locally. Table 4 summarizes the parameter settings of the four codes controlled in this study. A coverage factor  $k = 2$  was applied in all statistical uncertainties, which has a level of confidence of approximately 95% ( $2\sigma$ ).

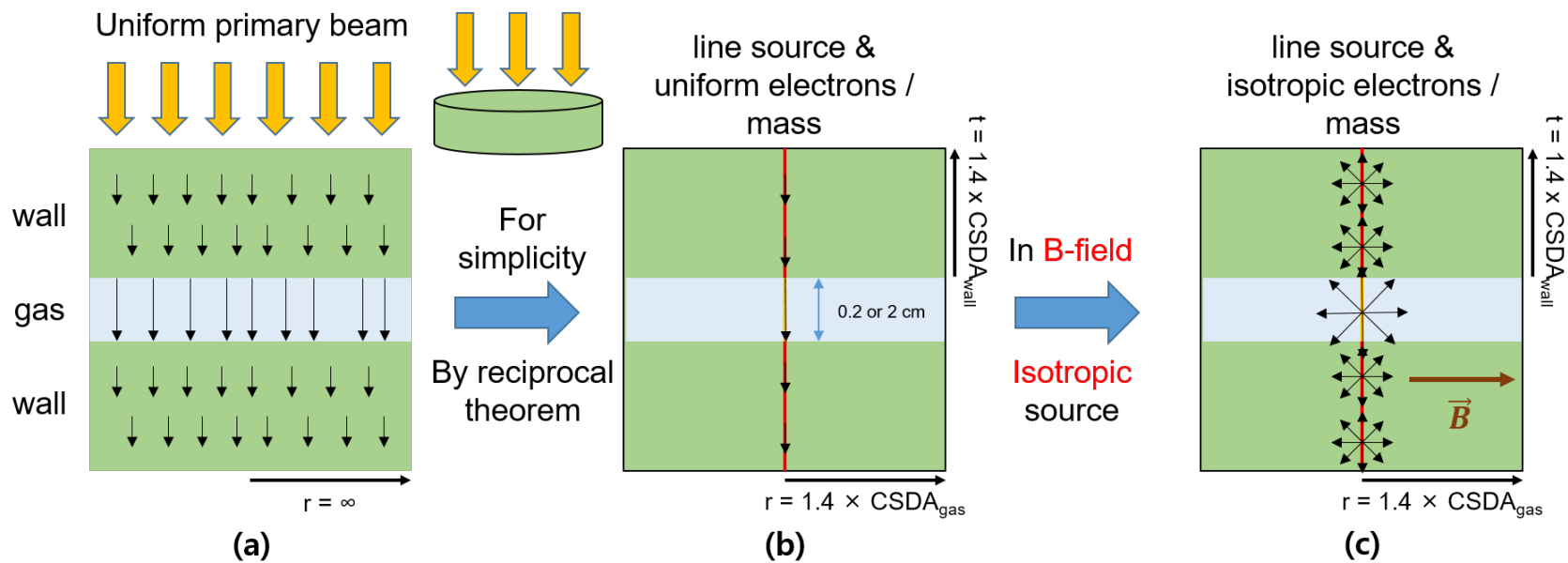


**Figure 5.** Schematic diagrams for the Fano cavity test in a magnetic field. Black arrows are simplified electron trajectories. The original Fano cavity theorem was presented in (a), and the simplified model of the Fano cavity theorem by the reciprocal theorem was presented in (b), and the adapted Fano cavity theorem in a magnetic field was presented in (c).

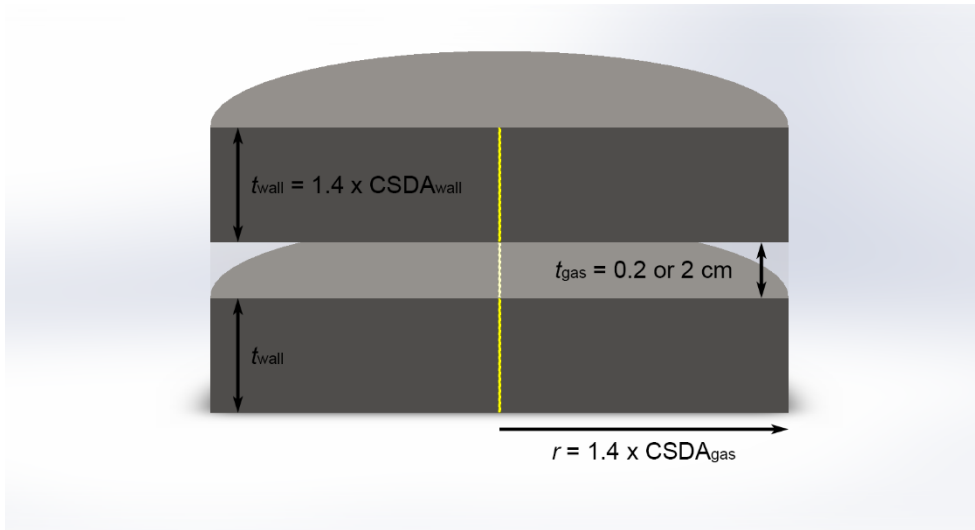


**Figure 6.** Schematic diagram of electron transport simulations for Fano cavity test (not scaled). Wall thickness ( $t_{\text{wall}}$ ) was 1.4 times the continuous slowing down approximation (CSDA) range in graphite, and gas thickness ( $t_{\text{gas}}$ ) was 0.2 or 2 cm. The radius of geometry ( $r$ ) was 1.4 times the CSDA range in gas material ( $\text{CSDA}_{\text{gas}}$ ). The density of gas material was 1000 times lower than that of wall material. Isotropic and uniform mono-energetic electrons per unit mass were generated at the central axial line of the cylindrical geometry (denoted as a yellow line).

**Table 3.** Physical dimensions of Monte Carlo simulations for different electron energies. Continuous slowing down approximation (CSDA) ranges in the National Institute of Standards and Technology (NIST) stopping-power and range tables for electrons (ESTAR) database were used.

Electron energy (MeV)	CSDA range (g/cm <sup>2</sup> )	Cylinder radius (cm)	Wall thickness (cm)	Gas thickness (cm)
0.01	$2.820 \times 10^{-4}$	$2.322 \times 10^{-1}$	$2.322 \times 10^{-4}$	0.2
0.1	$1.602 \times 10^{-2}$	$1.319 \times 10^1$	$1.319 \times 10^{-2}$	0.2
1	$4.964 \times 10^{-1}$	$4.088 \times 10^2$	$4.088 \times 10^{-1}$	0.2
3	$5.657 \times 10^0$	$1.422 \times 10^3$	$1.422 \times 10^0$	0.2

**Table 4.** Transport parameters applied to the simulations with condensed history algorithms of the four codes.

Monte Carlo codes	Default settings	Applied settings
EGSnrc	ESTEPE = 0.25, EM ESTEPE = 0.02	ESTEPE = 0.25, EM ESTEPE = 0.02 or 0.01 or EMULMT = 0.001
PENELOPE	C1 = C2 = 0.1, EABS1 = EABS3 = 0.01 × EMAX, EABS2 = 0.001 × EPMAX, W <sub>CC</sub> = EABS1,  W <sub>CR</sub> = EABS2,  DSMAX = 1 × 10 <sup>20</sup> cm,  ULDV = ULDE = ULEM = 0.02	C1 = C2 = 0.02, EABS1 = EABS3 = 1 × 10 <sup>3</sup> ,  EABS2 = EPMAX, W <sub>CC</sub> = min(2 / 1000 × E <sub>0</sub> , EABS1), W <sub>CR</sub> = min(2 / 10000 × E <sub>0</sub> , EABS2), DSMAX = 0.02, 0.01, or 1 × 10 <sup>-4</sup> cm,  ULDV = ULDE = ULEM = 0.02
MCNP6	Detailed Landau straggling sampling logic,  <i>efac</i> = 0.917, ESTEP = 3, MXDEFLEC = 10 mrad, MAXSTEP = 100 cm	Detailed Landau straggling sampling logic or Integrated Tiger Series (ITS)-style energy-indexing algorithm, <i>efac</i> = 0.99, ESTEP = 3, 70, 80, or 90, MXDEFLEC = 1 mrad, MAXSTEP = 1 cm
Geant4	G4EmStandardPhysics, G4UrbanMscModel ( <i>emstandard_opt3</i> ), <i>dRoverRange</i> = 0.2, <i>finalRange</i> = 1 mm, <i>RangeFactor</i> = 0.04, <i>GeomFactor</i> = 2.5, <i>Skin</i> = 1	G4EmStandardPhysics G4UrbanMscModel ( <i>user settings</i> ), <i>dRoverRange</i> = 0.003, <i>finalRange</i> = 1 nm, <i>RangeFactor</i> = 0.01, <i>GeomFactor</i> = 2.5, <i>Skin</i> = 2, <i>miss distance</i> = 1 μm, <i>ε<sub>min</sub></i> , <i>ε<sub>max</sub></i> = 0.00005, <i>fMinStep</i> = 1 nm, <i>fMaxStep</i> = ∞

#### **2.4.1. EGSnrc**

The EGSnrc user code, `egs_chamber`, was used in the following magnetic field simulation. The two electromagnetic field macros, default and the enhanced electromagnetic field (EEMF) macros, which were recently developed and tested by Malkov and Rogers, were applied in this study (34, 54). The default value (0.25) of the maximum fractional energy loss per step (ESTEPE) was set in both macros. The value for the step size restrictions based on energy loss, change in magnetic field strength, and direction (i.e., EM ESTEPE) varied from 0.01 to 0.02. In addition, a sub-parameter of EM ESTEPE, which imposes the upper limit on the amount of deflection in the electromagnetic field (EMULMT) was set to 0.001 in the default electromagnetic field macro as proposed in the previous study (55). The other settings were set to default values. The absorbed dose was calculated by the total of the energy deposited in the gas region.

#### **2.4.2. PENELOPE**

The “Penmain” routine from PENELOPE 2014 was employed for the Fano cavity test. This routine was modified for embedding the subroutine `penfield.f` package, which includes an electromagnetic field module. The strength and orientation of the uniform and static magnetic field were set in the `penfield.f` file. PENELOPE offers eight selectable transport parameters for each material. The absorption energy for electrons (EABS1) and positrons (EABS3) was chosen to be 1 keV. In order to eliminate bremsstrahlung interactions, the absorption energy for photons (EABS2) was set to values higher than simulated electron energies. The

maximum step length of electrons, DSMAX, in the wall and gas was an important parameter to generate statistically sufficient interactions in both regions. The DSMAX in the gas region was set to 0.02 cm, 0.01 cm and 1  $\mu\text{m}$ , while the default value of the DSMAX was used in the wall region. The fraction of the first transport mean-free path between hard elastic events, C1, and the maximum average fractional energy loss in a single step, C2, were both set to 0.02. The cutoff energy for the production of hard inelastic events ( $W_{\text{CC}}$ ) and bremsstrahlung events ( $W_{\text{CR}}$ ) were set to the minimum value between 0.2% of initial electron energies and 1 keV, and 0.02% of initial electron energies, respectively. The upper limit on the amount of deflection over the step due to the electromagnetic field, ULDV, the upper limit on the relative energy variation over the step in the electromagnetic field, ULDE, and the upper limit on the amount of change in the electromagnetic field over the step, ULEM, were set to the default value of 0.02. The absorbed dose was obtained by scoring the energy deposited by the interactions within the gas region.

### **2.4.3. MCNP6**

MCNP6.1 was chosen to be used for the Fano cavity test in a magnetic field. From the version of MCNP5, it has been possible to choose three energy indexing algorithms: bin-centered (MCNP-style), nearest group boundary (ITS-style), energy- and step-specific (Landau straggling sampling logic) treatment (23). In early versions of the MCNP series, some unphysical artifacts related to small geometric regions were found. However, Landau straggling sampling logic as a default algorithm of MCNP6.1 helps to eliminate these artifacts (56). The Integrated Tiger Series (ITS)-style energy-indexing algorithm, which was a previously preferred

option for electron transport, was also used by invoking DBCN(18) card (57). Also, the Evaluated Nuclear Data File (ENDF/B VI.8) database, which tabulates the cross sections and secondary distributions for atomic excitation, electron elastic scattering, subshell electro-ionization, and bremsstrahlung given for energies between 10 eV and 100 GeV, is available from MCNP6.1. This database remains unchanged for the energy range above 1 keV, but contains the low-energy range down to 1 eV for coherent and incoherent scattering and photoelectric absorption. To use the new data below 1 keV, the single-event method should be invoked. One can control the threshold energy for the single-event transport using the *electron\_method\_boundary* parameter in the electron physics option (PHYS:E). This method is only available for the detailed Landau straggling sampling logic in the energy-indexing algorithm. However, in this study the simulations were performed with the single-event transport turned on and off. The single-event transport from the initial electron energies were also simulated. The photon production by electrons and the creation of knock-on electrons produced in electron interactions were turned off. The stopping power energy spacing (*efac*) was set to 0.99, the highest value, or 0.917, the default value. The ESTEP value was optimized to maximize the accuracy of the Fano cavity tests after simulations with the default ESTEP value of 3 for graphite. The \*F8 tally defined as the integrated energy deposited across the gas region was used to calculate the absorbed dose in the gas region.

There are two methods to implement charged particle transport in the presence of magnetic fields using MCNP6. The first method is COSY INFINITY, which is fast and accurate (58). However, this method is only valid in a void cell. The other method is “particle ray tracing,” based on an algorithm from the MARS high-energy

particle transport code. This can be applied to both void and material cells. The particle ray tracing method was chosen in this study. The magnetic field tracking option was accessed by the BFLD card. One can control two additional parameters for static magnetic fields including the strength and direction of the magnetic field; the maximum deflection angle per step-size (MXDEFLEC), and the maximum step-size (MAXSTEP) were set to 1 mrad and 1 cm, respectively.

#### 2.4.4. Geant4

The version of Geant4.10.03 was used in this study. The simulations with the default transport parameters (*emstandard\_opt3* option) and the strict setting from the previous study that achieved 0.1% of accuracy in the Fano cavity test with the photon regeneration technique were also tested (33). The step size in Geant4 is controlled by the step function within two parameters, *dRoverRange* and *finalRange*. The *dRoverRange* refers to the maximum fractional reduction of the stopping range during a step, and the *finalRange* determines the minimum stopping range after the range reduction by *dRoverRange*. In this study, the *dRoverRange* was set to 0.2 or 0.003, and the *finalRange* was set to 1 mm or 1 nm. In the multiple scattering process in Geant4, an additional step limitation is controlled by three parameters: *RangeFactor*, *GeomFactor*, and *skin*. The *RangeFactor* limits the maximum step size to a fraction of the mean free path of particles, and was set to 0.04 or 0.01. The *GeomFactor* controls a minimum number of steps in the geometrical volume, and was set to 2.5. The *skin* determines the number of mean free path in which single scattering is applied, and was set to 1 or 2. To improve the accuracy of the electromagnetic field simulations, the *miss distance* which restricts the maximum

distance between the chords and the curved trajectories was set to 1  $\mu\text{m}$ . The *delta intersection* is the accuracy of the estimated intersection compared to the correct intersection at the boundary of the volume. The *delta one step* is the accuracy of the ordinary integrated steps at the endpoint. Both the *delta intersection* and *delta one step* were set to 1  $\mu\text{m}$ . The absorbed dose was calculated by the integration of the energy deposition at each step in the gas region.

## **2.5. Beam Quality Specifiers and Beam Quality Conversion Factors**

The `egs_chamber` code used in these simulations has been developed to meet the efficiency and accuracy of ionization chamber simulations with several variance reduction techniques (59). The true variance reduction techniques were used in the `egs_chamber` simulations (59). The intermediate phase space storage (IPSS) technique was applied to the volume of the cylindrical water that was 0.26 cm larger than the outer dimension of the parallel plate ionization chambers in radius and height. A photon cross-section enhancement (XCSE) was employed, and the XCSE region was defined as the volume with a 1 cm margin from each surface of the geometry. The XCSE factor was 128 based on the previous study using a water shell and an air sphere (59). However, the test simulations using a XCSE factor of 16 were not significantly different. Correlated sampling was applied to calculate doses to water and the sensitive volume simultaneously. The electron range-based Russian roulette technique was also employed, and the cavity geometry for this technique was the volume of 0.01 cm-thickness outside of the air volume including the guard

ring of the parallel plate ionization chambers. The survival probability was 1/128. These variance reduction techniques were applied for the simulations of the following section.

The photon component beam quality specifier ( $\%dd(10)_x$ ) was calculated as a percent depth-dose at a depth of 10 cm in water for a field size of  $10 \times 10 \text{ cm}^2$ . The collimated photon beams using energy spectra from the phase spaces were used to calculate  $\%dd(10)_x$  in a water phantom of  $30 \times 30 \times 30 \text{ cm}^3$ . The  $\%dd(10)_x$  was calculated after selecting few possible  $d_{\max}$  points instead of calculating all depth dose curve. The depth of the maximum dose ( $d_{\max}$ ) for each photon energy was searched at the nominal  $d_{\max}$  (e.g., 1.5 cm for 6 MV) and the nominal  $d_{\max} \pm 0.05$  and  $\pm 0.1$  cm. Two identical cylinders of 0.5 cm-radius and 0.25 cm-height were located at  $d_{\max}$  and a depth of 10 cm to calculate  $\%dd(10)_x$ .

The beam quality conversion factor,  $k_Q$ , can be directly calculated by MC simulations with high accuracy (60). To assure the reliability of the results from our ionization chamber modeling, we calculated the  $k_Q$ -values without a magnetic field and compared them with the published data (3). The absorbed dose to water,  $D_{\text{water}}$ , was calculated as a dose to a cylindrical water disk having a radius of 0.25 cm and a height of 0.05 cm in a water phantom of  $30 \times 30 \times 30 \text{ cm}^3$  at a depth of 10 cm. This volume of the cylindrical water disk was small enough to maintain a uniform dose distribution within 0.2%. The parallel plate ionization chamber was located at the same location in the water phantom of  $30 \times 30 \times 30 \text{ cm}^3$  to calculate the absorbed dose to the sensitive volume (i.e., air) of the ionization chamber,  $D_{\text{chamber}}$ . The beam quality conversion factor was determined as the ratio of  $[D_{\text{water}}/D_{\text{chamber}}]$  for the user beam of quality,  $Q$ , to  $[D_{\text{water}}/D_{\text{chamber}}]$  for the Co-60 beam as below:

$$k_Q = \frac{[D_{\text{water}}/D_{\text{chamber}}]_Q}{[D_{\text{water}}/D_{\text{chamber}}]_{\text{Co-60}}} \quad (2)$$

## 2.6. Magnetic Field Correction Factors

With the same geometry as described in section 2.5.,  $D_{\text{chamber}}$  and  $D_{\text{water}}$  in a magnetic field were calculated at an SSD of 100 cm for Co-60 and 6, 7, 10, and 15 MV photon beams, and of 133.5 cm for a 7 MV photon beam. The magnetic field correction factor,  $k_B^Q$ , was defined as the ratio of the  $k_Q$ -values with and without a magnetic field of  $B$  as below:

$$k_B^Q = \frac{[D_{\text{water}}/D_{\text{chamber}}]_Q^B}{[D_{\text{water}}/D_{\text{chamber}}]_Q} \quad (3)$$

A magnetic field of 0.35, 0.5, 1.0, and 1.5 T perpendicular or parallel to the incident beam direction was simulated. In all calculations, we assumed that the magnetic fields did not affect  $\bar{W}/e$ , the mean energy spent in air to produce an ion-electron pair. The EEMF macros introduced in Section 2.4. were used for all simulations in a magnetic field with the default parameters.

## 2.7. Dose Heterogeneity in the Sensitive Volume of Chamber under a Magnetic Field

In order to figure out dose heterogeneity within a parallel plate ionization chamber in a magnetic field, the sensitive volume of the Roos chamber (height of 0.2 cm and radius of 0.75 cm) was segmented into 128 pieces of equal volume. First,

the height of the chamber was divided into four layers of equal thickness. Each layer was divided into eight concentric pie-shaped parts of 45°. Finally, each part was further divided into four concentric pieces to make them the same volume. Doses to each piece were calculated for 6 and 15 MV photon beams at the four strengths of magnetic field perpendicular to the beam direction. Doses to each piece in a magnetic field were normalized by a mean dose to the whole sensitive volume without a magnetic field. In addition, the height and radius of the sensitive volume were changed from 0.2 cm to 0.1 or 0.4 cm and from 0.75 cm to 0.5 or 1.0 cm, respectively, in order to investigate the dependence of  $k_B^Q$  on the geometry and dimension of the chamber for Co-60 and 7 MV beams in the magnetic fields perpendicular to the beam direction.

## 3. Results

### 3.1. The Fano Cavity Tests

#### 3.1.1. EGSnrc

Figures 7 and 8 shows the results of the Fano cavity test using EGSnrc. Without a magnetic field, all of the results were within 0.1%. With a magnetic field, the results for EM ESTEPE of 0.02 (Figure 7(a)) and 0.01 (Figure 7(b)) under the default electromagnetic field macro varied within  $2.70 \pm 0.06\%$  and  $1.00 \pm 0.05\%$ , respectively, with a coverage factor  $k = 2$ . When EMULMT was changed from 0.02 to 0.001 (Figure 7(c)), the accuracy was within 0.1% except for 3.0 T; the simulations at 3.0 T terminated prior to running through the initial number of histories. The result for 0.01 MeV in this parameter setting exceeded 1% at 3.0 T. In a strong magnetic field (e.g., 3 T), low-energy electrons had highly-curved trajectories. This implied that the default EM macros with a small EMULMT value of 0.001 cannot correctly transfer low-energy electron in its deflection especially in a strong magnetic field, where the Larmor radius of the electron was comparable to the step size of electrons. However, if the EEMF macros were applied for the simulation in a magnetic field, the accuracy was within 0.1% for all situations investigated in this study; except for 3.0 T, the accuracy was within 0.2%. Figure 8 compared the results of the Fano cavity test in a magnetic field for the gas thickness of 0.2 cm and 2 cm. The relative differences between the dose to the gas region calculated by the MC simulation and the theoretical value were within  $\pm 0.2\%$  for all combinations of electron energies and magnetic field strengths. Statistical uncertainties of each simulation were below 0.06%. This implies that the `egs_chamber` code with the EEMF macros could

simulate radiation transport accurately in a uniform magnetic field. These results were also comparable to the previous data using the DOSRZnrc user code by Malkov and Rogers (34).

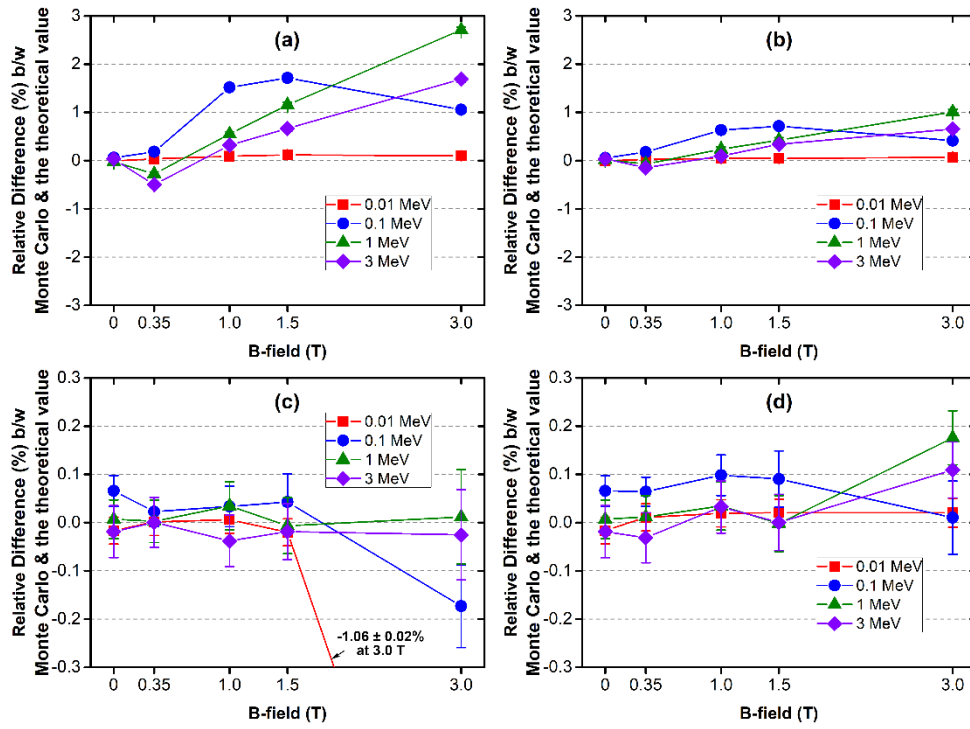


**Figure 7.** Results of the Fano cavity test using EGSnrc. The EM ESTEPE of 0.02 (a) and 0.01 (b), and the EMULMT of 0.001 (c) were used under the default electromagnetic field macro, `emf_macros.mortran`. The enhanced electromagnetic field (EEMF) macro (Malkov and Rogers, 2016), `EEMF_macros.mortran`, was applied (d).

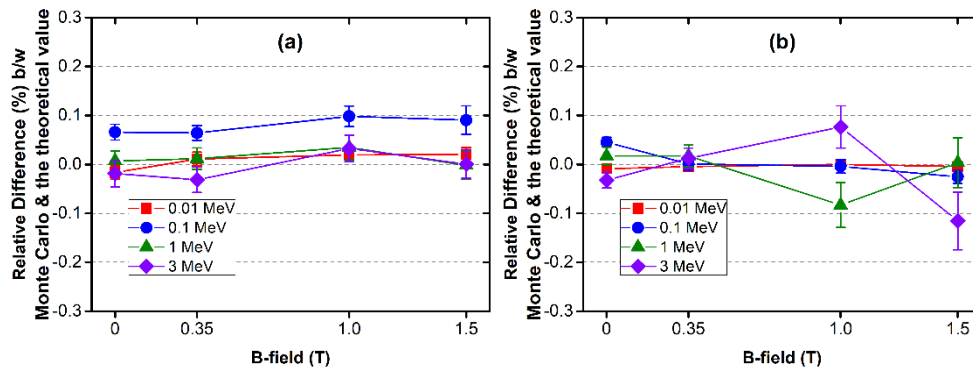


**Figure 8.** Results of Fano cavity test in a magnetic field for the gas thickness ( $t$ ) of 0.2 cm (a) and 2 cm (b). Relative differences in dose per particle between Monte Carlo simulation and theoretical value are shown as a function of magnetic field strength in Tesla for four electron energies. Statistical uncertainties are given with a coverage factor  $k = 1$ .

### 3.1.2. PENELOPE

Figure 9 illustrates the results of the Fano cavity test using PENELOPE. Without magnetic field, the results for 0.01, 0.1, 1, and 3 MeV (see Figures 9(a)-(c)) did not depend on DSMAX, and were  $0.00 \pm 0.02\%$ ,  $0.03 \pm 0.04\%$ ,  $0.30 \pm 0.05\%$ , and  $0.88 \pm 0.07\%$  varying on average, respectively. These results were comparable to a previous study (28). With magnetic field, the larger the step size (i.e., larger DSMAX) applied, the larger relative differences were shown, especially in 3.0 T. In general, the lower the electron energy was, the lesser the relative difference, regardless of the DSMAX values and magnetic field strengths. The relative differences of 0.01 MeV were within  $0.003 \pm 0.069\%$  for all situations implemented in this study. With DSMAX of 0.02 cm, the relative differences of 0.1 MeV exceeded 2% at 3.0 T. However, these became less than 0.03% after reducing DSMAX into 1  $\mu\text{m}$ . In the single scattering mode without a magnetic field, the relative difference of 0.01, 0.1, 1 and 3 MeV were  $0.00 \pm 0.12\%$ ,  $0.02 \pm 0.24\%$ ,  $0.23 \pm 0.39\%$ , and  $0.53 \pm 0.63\%$ , respectively. However, the simulation time of the single scattering mode needed 4.3 to 18.9 times that of the condensed history algorithm.

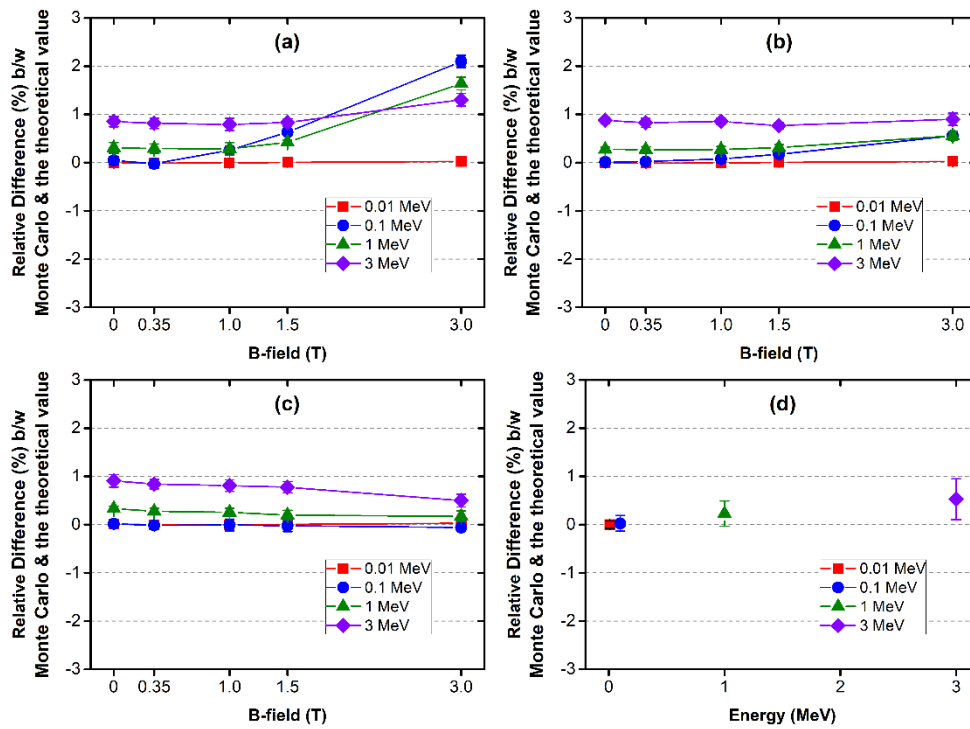


**Figure 9.** Results of the Fano cavity test using PENELOPE. Different DSMAX values of 0.02 cm (a), 0.01 cm (b), and 1  $\mu\text{m}$  (c) were applied. The other parameters were benchmarked with the previous study (Sempau and Andreo, 2006). A single scattering option without a magnetic field was also simulated for different energies of electrons (d). Statistical uncertainties were smaller than the symbol or shown as error bars with a coverage factor  $k = 2$ .

### 3.1.3. MCNP6

The results of the Fano cavity test using MCNP6.1 were shown in Figure 10. Some of the simulations at magnetic field strengths of 1.0, 1.5 and 3.0 T unexpectedly stopped with a bad trouble message when the default ESTEP value was applied. This was because the multi-collision condensed history theory started the breakdown of its application. These were caused by non-physical simulation because the number of electron substeps were not sufficient. If the default *efac* value of 0.917 was applied, the maximum relative difference exceeded 40% for 1 MeV at 3.0 T. Even without a magnetic field, Monte Carlo calculated doses for 1 and 3 MeV was about 10% less than the theoretical value. With the maximum value of *efac* (i.e., 0.99), the relative differences between Monte Carlo calculated doses and the theoretical value were reduced (Figure 10(c)). There were small differences less than 0.2% between ITS and the default energy indexing style except for 3.0 T (Figures 10(b)-(c)). However, Monte Carlo calculated doses for 1 MeV electrons at 3.0 T was 11% less than the theoretical value. Even without a magnetic field for 3 MeV electrons the calculated dose was 2.5% more than the theoretical value. In this parameter setting, the average numbers of electron substeps in the gas region for 0.01, 0.1, 1, and 3 MeV electrons were 382, 691, 0.2, and 0.09, respectively. By the rule of thumb in MCNP, an electron should generate at least ten substeps in any region of material (61). In order to satisfy this rule, the ESTEP values in the gas region for 0.01, 0.1, 1, and 3 MeV electrons should exceed 0.1, 8, 181, and 533, respectively. The relative differences were reduced after the increased ESTEP values were set. When the ESTEP was set to 80 for both 1 and 3 MeV electrons, the relative differences were within 0.7%. With the ESTEP values of 90 for 1 MeV and 70 for 3

MeV, the relative differences were found to be less than 0.4%. These optimized ESTEP values were less than the values calculated by the rule of thumb. Simulations after turning on a single scattering option showed small differences less than 0.1% for all electron energies with no magnetic field (Figure 10(f)). A single scattering option for electron energy less than 1 keV was turned off during the simulation with the default energy indexing algorithm.

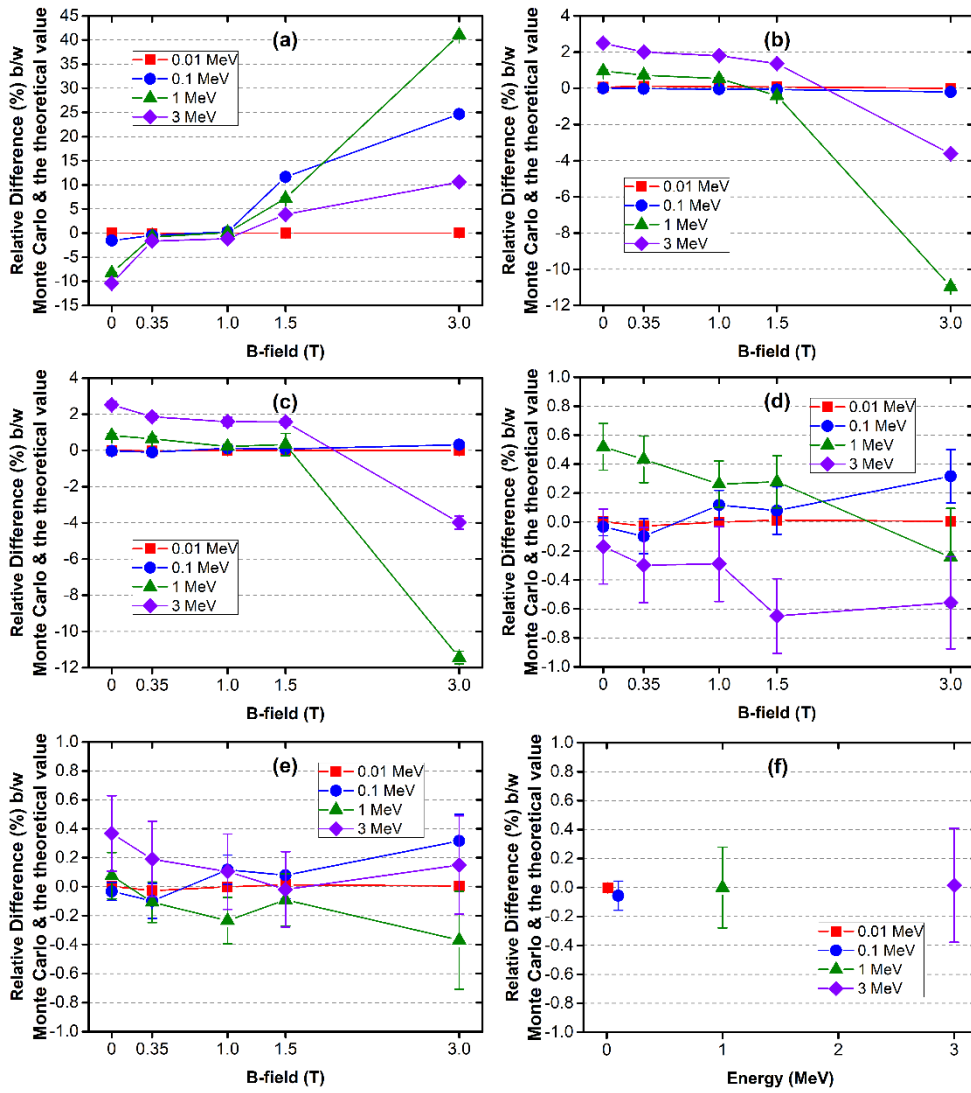


**Figure 10.** Results of the Fano cavity test using MCNP6 code. ITS energy indexing and two different  $efac$  values of 0.917 (a) and 0.99 (b). Default energy indexing and  $efac$  value of 0.99 were applied in (c). The default ESTEP value was used in (a)-(c). With the default energy indexing and  $efac$  value of 0.99, ESTEP of 80 for 1 and 3 MeV was applied in (d), and ESTEP of 90 for 1 MeV and ESTEP value of 70 for 3 MeV were applied in (e). A single scattering option was turned on without a magnetic field in (f). Statistical uncertainties were smaller than the symbol or shown as error bars with a coverage factor  $k = 2$ .

### 3.1.4. Geant4

Figure 11 displays the results of the Fano cavity test using Geant4. Without a magnetic field, the simulation results with the default parameters for 1 MeV and 3 MeV electrons showed differences larger than 8%, while implementing the strict parameters described in a previous study (33), the relative differences were within 1.4%. In the presence of magnetic field, the maximum relative difference using the default parameter was less than 1.6% except for 0.1 MeV electrons. The calculated dose for 0.1 MeV electrons at 3.0 T was somehow 30% smaller than the theoretical value. With the strict parameters except for 3.0 T, the maximum relative difference was within 1.7%. At 3.0 T, the calculated doses for 1 and 3 MeV electrons were 14.9% and 6.4% smaller than the theoretical value.

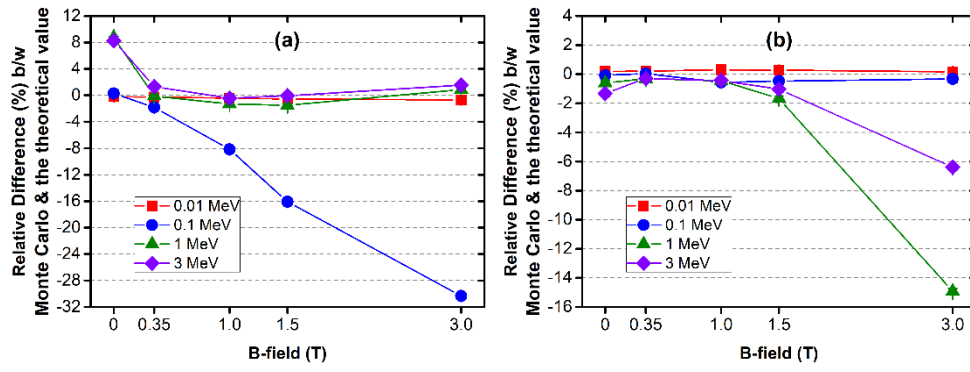


**Figure 11.** Results of the Fano cavity test using Geant4. The default parameters were used in (a), and the parameters from the previous study (O'Brien et al, 2016) were benchmarked in (b). Statistical uncertainties were smaller than the symbol or shown as error bars with a coverage factor  $k = 2$ .

### 3.2. Summary of the Fano Cavity Tests

The accuracy of the Monte Carlo simulations using four general-purpose codes in a magnetic field was evaluated by the adaptive Fano cavity tests for electron energies of 0.01 to 3 MeV and magnetic field strengths of 0 to 3 T. The relative difference between the dose calculated by Monte Carlo simulations and the theoretical value was regarded as the accuracy of Monte Carlo simulations. With default parameter options of each Monte Carlo code, an appropriate accuracy within 1% could not be achieved. However, each Monte Carlo code could enhance its accuracy of the simulations in a magnetic field by changing step size parameters or electromagnetic field macros. EGSnrc showed the best accuracy within 0.2% when the EEMF macros were applied, while the relative difference was exceeded more than 2% using the default electromagnetic macros and parameter settings. PENELOPE and MCNP6 could achieve the accuracy within 1.0% and 0.4%, respectively, after optimizing the step size parameters. The accuracy within 1.7% was obtained by Geant4 except for the simulations in 3.0 T after controlling the step size parameters. In that, EGSnrc with the EEMF macros was adopted in the following simulations.

### 3.3. Simulations of the Linac and Co-60 Beams and Beam Quality

#### Conversion Factors

The  $\%dd(10)_x$  of the Co-60 and 6, 7, 10, and 15 MV photon beams for a field size of  $10 \times 10 \text{ cm}^2$  at an SSD of 100 cm was determined 58.3%, 66.6%, 69.5%, 73.6%, and 76.8%, respectively. The  $\%dd(10)_x$  of the 7 MV photon beam of the Elekta™ MR-linac for a field size of  $10 \times 10 \text{ cm}^2$  at an SSD of 133.5 cm was 71.9%. Statistical uncertainties in all simulations were less than 0.2% with a coverage factor  $k = 1$ . The measured  $\%dd(10)$  of the 6, 10, and 15 MV photon beams performed by Sheikh-Bagheri and Rogers (62) was 66.6%, 73.6%, and 76.9%, respectively. In the previous studies for the MR-linac using the Geant4 code, the  $\%dd(10)_x$  of the 7 MV photon beam at an SSD of 133.5 and 142.5 cm were 71.4% and 72.6%, respectively (33, 45). Our  $\%dd(10)_x$  of the 7 MV photon beam of the MR-linac at an SSD of 100 cm was comparable to the previous result of 69.4% (62). The differences between our results and the published data were within 0.2% except for the 7 MV beam at an SSD of 133.5 cm.

The calculated  $k_Q$ -values of the NACP-02, Roos, and Exradin A11 are shown in Figure 12. The maximum difference in these  $k_Q$ -values of the NACP-02 and Roos from the data measured by Muir et al. (3) was 0.14%, while the corresponding difference of the Exradin A11 from the data calculated by Muir et al. (3) was 0.23%. Most of our results were in agreement with the previous data within statistical uncertainties (3). Consequently, the linac simulation and the collimated beam modeling based on the phase space were regarded as a reliable approach for estimating the  $k_Q$  and  $k_B^Q$ -values of the parallel plate ionization chambers.

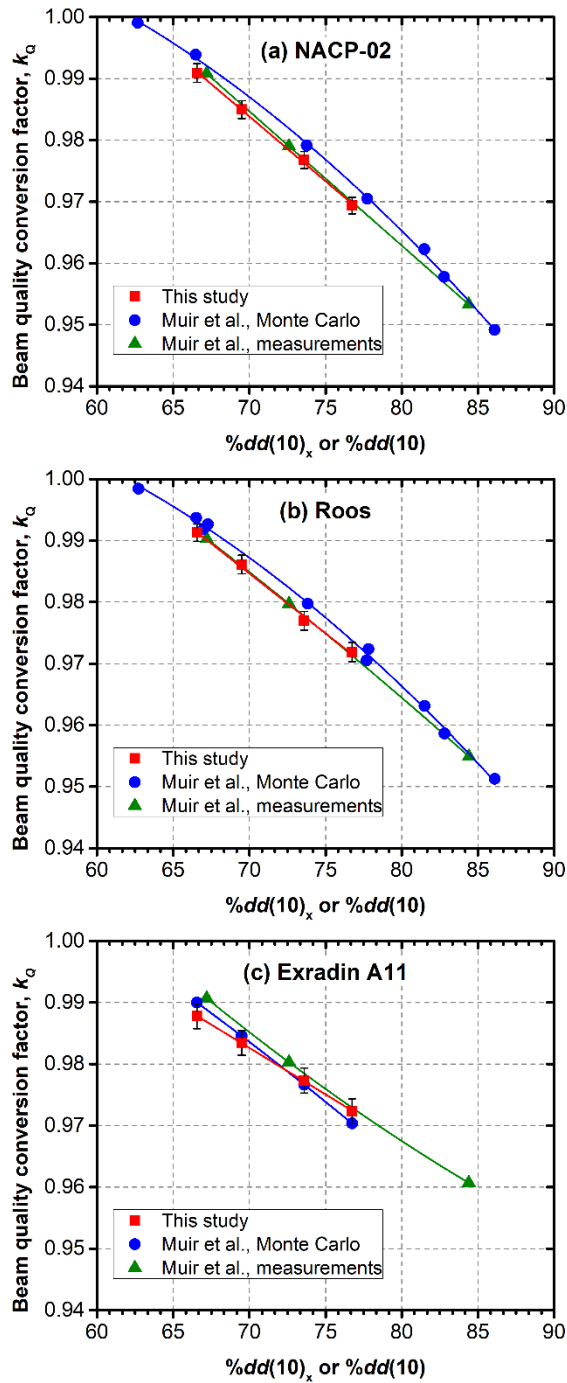


**Figure 12.** Monte Carlo calculated beam quality conversion factors ( $k_Q$ ) for the NACP-02 (a), Roos (b), and Exradin A11 (c). Statistical uncertainties are given with a coverage factor  $k = 1$ .

### 3.4. Response of Parallel Plate Ionization Chambers in a Magnetic Field and Magnetic Field Correction Factors

Figures 13 and 14 displays  $D_{\text{chamber}}$  and  $D_{\text{water}}$  of five beam energies in a magnetic field perpendicular to the beam direction as a function of magnetic field strengths. The values of  $D_{\text{chamber}}$  and  $D_{\text{water}}$  were normalized by the corresponding values of no magnetic field. After normalization, the dose responses of three ionization chambers were continuously increased by increasing the magnetic field strengths up to 1.0 T. In 1.5 T, the dose responses were decreased compared to the corresponding dose response in 1.0 T except the Co-60 beam. The maximum increase of  $D_{\text{chamber}}$  for the Co-60, and 6, 7, 10, and 15 MV beams were 17.3% of the NACP-02, and 11.5%, 10.5%, 9.0%, and 7.9% of the Roos, respectively. The lower the photon energy was, the more the normalized  $D_{\text{chamber}}$  was increased. On the contrary, the normalized  $D_{\text{water}}$  was slightly decreased with increasing the magnetic field strengths by 0.21% on average. The normalized  $D_{\text{water}}$  for a high-energy beam was decreased more than those for a low-energy beam. The amount of decrease in  $D_{\text{water}}$  was almost negligible for the Co-60, 6, and 7 MV beams. The maximum decrease of  $D_{\text{water}}$  was -1.1% at 15 MV and 1.5 T. Also note that with a magnetic field parallel to the beam direction,  $D_{\text{chamber}}$  and  $D_{\text{water}}$  varied by no more than 1%.

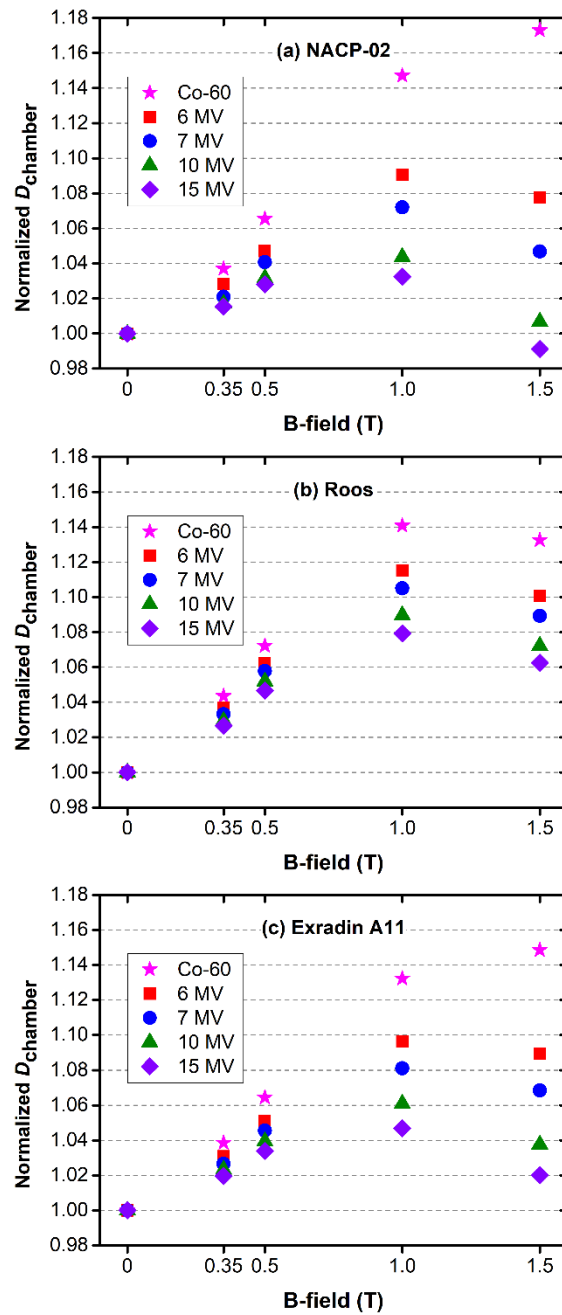


**Figure 13.** Doses to the sensitive volume of the chambers ( $D_{\text{chamber}}$ ) for the NACP-02 (a), Roos (b), and Exradin A11 (c). A magnetic field of 0.35, 0.5, 1.0 and 1.5 T was perpendicular to the incident beam direction of 5 different energies. All the responses were normalized by the corresponding values of no magnetic field. Statistical uncertainties were smaller than the symbols with a coverage factor  $k = 1$ .

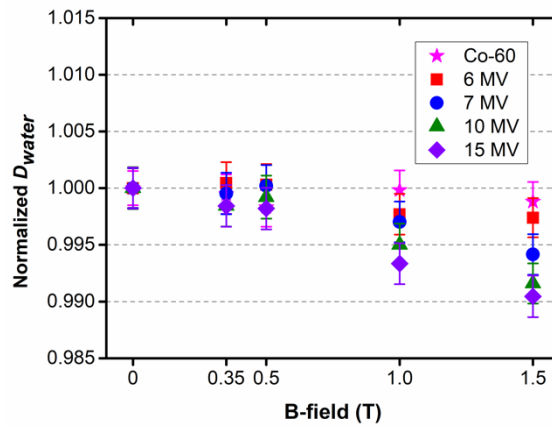


**Figure 14.** Doses to water ( $D_{water}$ ). A magnetic field of 0.35, 0.5, 1.0 and 1.5 T was perpendicular to the incident beam direction of 5 different energies. All the responses were normalized by the corresponding values of no magnetic field. Statistical uncertainties were given with a coverage factor  $k = 1$

Figure 15 shows the calculated  $k_B^Q$ -values for the four strengths of magnetic fields perpendicular (Figures 15(a), (c), and (e)) and parallel (Figures 15(b), (d), (f)) to the beam direction. Five beam energies were specified by their corresponding  $\%dd(10)_x$ . The statistical uncertainties were within 0.2% ( $k = 1$ ). The  $k_B^Q$ -values of the three parallel plate ionization chambers for the perpendicular orientation ranged from 0.85 to 0.99. In general, the magnetic field correction for the perpendicular orientation was increased with decreasing the photon energy and increasing the magnetic field strength. However, the magnetic field strength at which the lowest  $k_B^Q$ -value occurred was 1.0 T rather than 1.5 T, except for the Co-60 beam. The minimum  $k_B^Q$ -values of the NACP-02 and Exradin A11 for Co-60 beam occurred in 1.5 T. The  $k_B^Q$ -values of the three parallel plate ionization chambers varied noticeably by the magnetic field strength as well as the beam quality. When the magnetic field was parallel to the beam direction, all  $k_B^Q$ -values of the three parallel plate ionization chambers became larger than 0.99 for all cases investigated in this study (Figures 14(b), (d), and (f)). Since there was almost no Lorentz force in this orientation except for scattered electrons deflected in the water, the  $k_B^Q$ -values were close to 1.0. The differences in the  $k_B^Q$ -values of the NACP-02 and Roos between this study and the previous studies (40, 41) were summarized in Tables 5 and 6. These differences might be caused by subtle differences in the simulation geometries and dimensions of parallel plate ionization chambers used in the three studies.

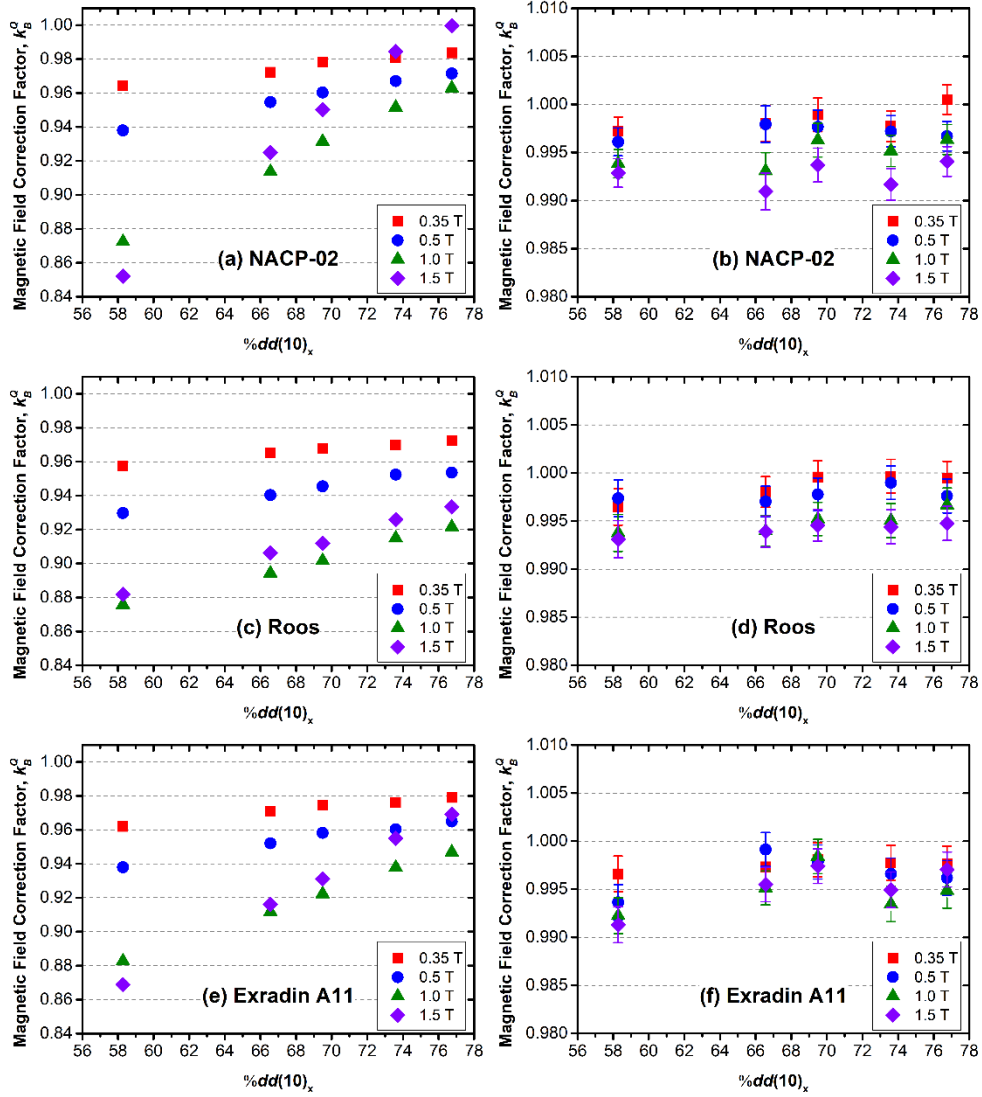


**Figure 15.** Correction factors ( $k_B^Q$ ) vs. photon beam energies for magnetic fields perpendicular to the beam direction ((a), (c), and (e)) and for magnetic fields parallel to the beam direction ((b), (d), and (f)). Statistical uncertainties were smaller than the symbols or given with a coverage factor  $k = 1$ .

**Table 5.** Comparison of magnetic field correction factors ( $k_B^Q$ ) for the NACP-02. Perpendicular and parallel magnetic field orientations to the beam direction were denoted as ‘ $\perp$ ’ and ‘ $\parallel$ ’, respectively.

NACP-02						
	Co-60 / 0.35 T		6 MV / 0.35 T		7 MV / 1.5 T	
B-field orientations	$\perp$	$\parallel$	$\perp$	$\parallel$	$\perp$	$\parallel$
Malkov and Rogers (40)	0.9644	0.9971	-	-	0.9445	0.9809
Pojtinger et al. (41)	-	-	0.9765	-	0.9372	-
This study	0.9667	0.9976	0.9723	0.9980	0.9587	0.9954
Diff. (%) - vs. Malkov and Rogers (40)	0.24	0.05	-	-	1.50	1.48
Diff. (%) - vs. Pojtinger et al. (41)	-	-	-0.43	-	2.29	-

**Table 6.** Comparison of magnetic field correction factors ( $k_B^Q$ ) for the Roos. Perpendicular and parallel magnetic field orientations to the beam direction were denoted as ‘ $\perp$ ’ and ‘ $\parallel$ ’, respectively.

B-field orientations	Roos					
	Co-60 / 0.35 T		6 MV / 0.35 T		7 MV / 1.5 T	
	$\perp$	$\parallel$	$\perp$	$\parallel$	$\perp$	$\parallel$
Malkov and Rogers (40)	0.9576	0.9970	-	-	0.9113	0.9849
Pojtinger et al. (41)	-	-	0.9651	-	0.9272	-
This study	0.9582	0.9970	0.9723	0.9980	0.9118	0.9946
Diff. (%) - vs. Malkov and Rogers (40)	0.06	0.00	-	-	0.05	0.98
Diff. (%) - vs. Pojtinger et al. (41)	-	-	-0.39	-	-1.66	-

### **3.5. Dose Heterogeneity within the Sensitive Volume of Chamber in a Magnetic Field**

In Figures 16 and 17, a photon beam was incident from back of the figure toward the front, and the magnetic field was along the +Y axis ( $90^\circ$ ) so that the Lorentz force on the secondary electrons was mainly directed to the +X axis ( $0^\circ$ ). Diagrams from left to right represent the four layers of the sensitive volume of the chamber divided by 0.05 cm height from the entrance of the beam to the exit. By the Lorentz force, the trajectories of secondary electrons were not straight forward in the sensitive volume so that doses to each piece in the sensitive volume were not uniform. Such dose heterogeneity in the sensitive volume was due to the helical drift motion of secondary electrons. As depositing their energies in the sensitive volume, the Larmor radii become larger even in the sensitive volume. Likewise, track lengths of secondary electrons within the sensitive volume strongly depend on where they are generated or where they entered into that volume. Figures 16 and 17 show such dose heterogeneity within the sensitive volume for the four magnetic field strengths for 6 and 15 MV beams, respectively. The dose heterogeneity in the chamber was increased as increasing the magnetic field strengths. Even within the same layer, the doses were non-uniform along the direction of the Lorentz force. The doses to the entrance layer (first columns in Figures 16 and 17) were higher than the doses of no magnetic field, while the doses to the exit layer (last columns in Figures 16 and 17) were lower. In general, the less photon beam energies were, the larger dose heterogeneities in the sensitive volume were.

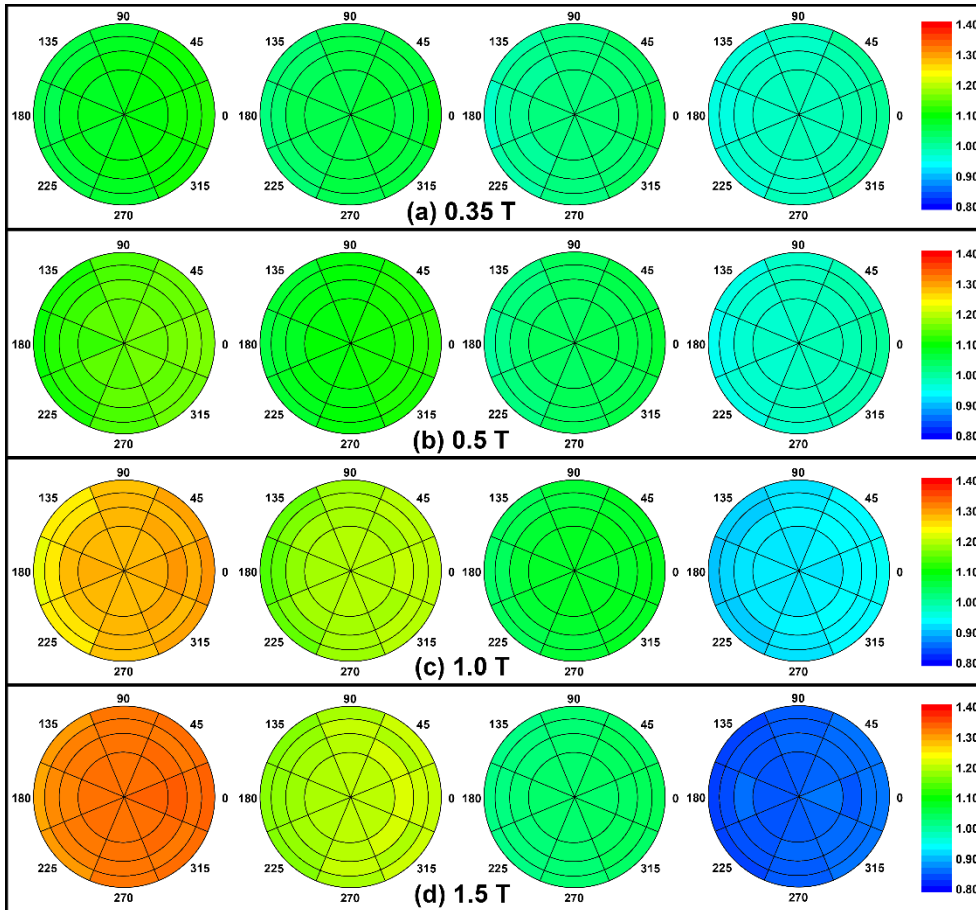


**Figure 16.** Relative dose distribution of 6 MV beam inside the sensitive volume of the Roos chamber for 0.35 T (a), 0.5 T (b), 1.0 T (c), and 1.5 T (d). Diagrams from left to right represent the four layers of the sensitive volume of the chamber from entrance of the beam to exit. A photon beam was incident from back of the figure toward the front, and a magnetic field was assumed to +Y axis (to  $90^\circ$ ) so that the Lorentz force of electrons was mainly directed to +X axis (to  $0^\circ$ ) in the figure. The average statistical uncertainty was 0.55%, and the maximum statistical uncertainty was 0.85% with a coverage factor  $k = 1$ .

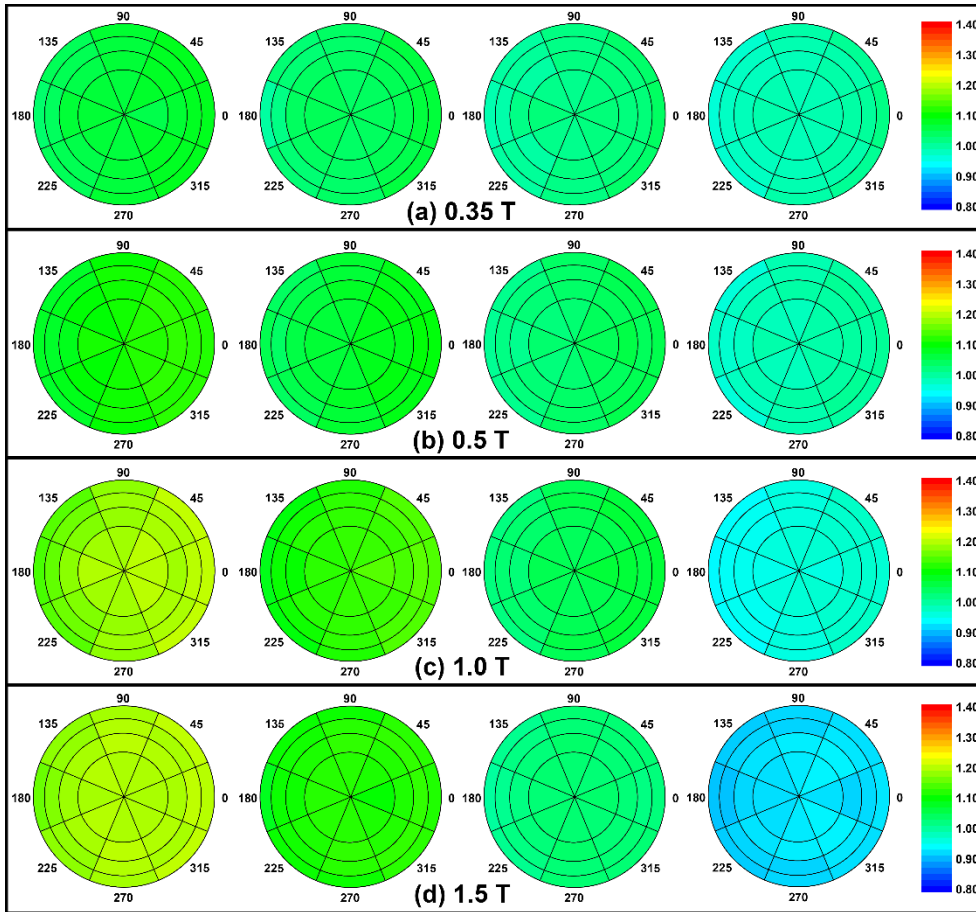


**Figure 17.** Same as Figure 15 but for a 15 MV beam. The average statistical uncertainty was 0.56%, and the maximum statistical uncertainty was 0.76% with a coverage factor  $k=1$ .

Figure 18 shows the variation of  $k_B^Q$ -values on different dimensions of the parallel plate ionization chambers in a perpendicular magnetic field of 1.5 T for Co-60 and 7 MV beams. The height and radius of the sensitive volume were changed from the original dimension of the Roos. The  $k_B^Q$ -values were not highly affected by change in the radius of the sensitive volume, while a significant variation of the  $k_B^Q$ -values was caused by change in the height of the sensitive volume. The smaller height of the sensitive volume was, the higher  $k_B^Q$ -values were except for 0.4 cm height in 1.5 T. The smaller radius of the sensitive volume was, the higher  $k_B^Q$ -values were. Even though the minimum  $k_B^Q$ -values of the three parallel plate ionization chambers occurred in 1.0 T, Figure 17 implies that these should strongly depend on the dimension of the sensitive volume.

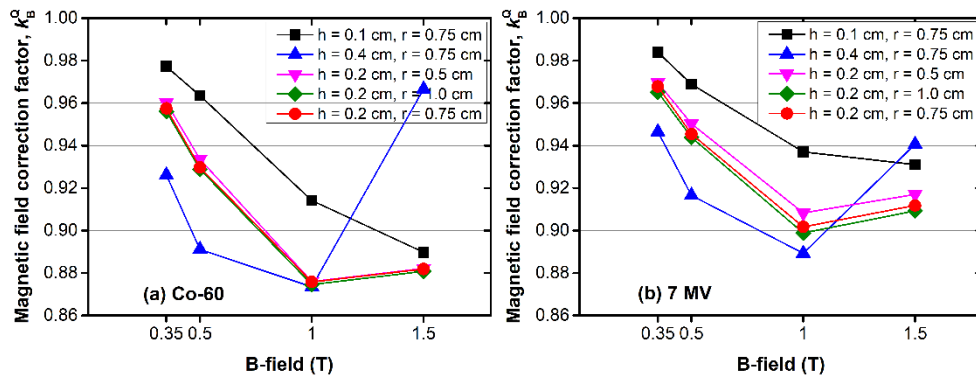


**Figure 18.** Variation of magnetic field correction factors,  $k_B^Q$  on different dimensions of the sensitive volume: height ( $h$ ) is 0.1, 0.2, and 0.4 cm, and radius ( $r$ ) is 0.5, 0.75, and 1.0 cm for Co-60 (a) and 7 MV (b) in four strengths of perpendicular magnetic fields. The Roos chamber has 0.2 cm height and 0.75cm radius (red solids).

## 4. Discussion

The Monte Carlo codes with their capability of magnetic field simulation can play a key role in estimating the magnetic field correction factor of ionization chambers. However, it was reported that the difference in the magnetic field correction factors calculated by EGSnrc and Geant4 was 0.4-1.2% (33, 34). Prior to the simulations of dose to the air cavity of an ionization chamber in a magnetic field, the accuracy of Monte Carlo codes should be verified according to the Fano cavity theorem.

Malkov and Rogers (34) developed the EEMF macros for the EGSnrc simulation with a magnetic field. They performed the Fano cavity test using the EEMF macros in DOSRZnrc user code, and achieved 0.1% of accuracy in a gas slab of 0.2 and 2 cm thicknesses using an adaptive integration mode which is the default setting of the EEMF macros. Instead of the DOSRZnrc user code (34), we used the `egs_chamber` code, which offers EGSnrc C++ class library, and the simulation results in the geometry of 0.2 cm slab were equivalent to the previous study. Spindeldreier et al. (36) employed a customized magnetic field macro provided by Kawrakow for the simulation in a magnetic field. The results of the Fano tests for 1.25 MeV electrons agreed to within 0.13% at 1.0 and 3.0 T. Also, Ghila et al. (55) calculated the depth dose and surface dose profile at 0.2 T. In this simulation, the default electromagnetic field macro of EGSnrc was applied while changing the EMULMT from 0.02 to 0.001. However, they just reported that the Fano cavity test was satisfied without mentioning details of the results. We performed a Fano cavity test with the same setting, and achieved 0.1% accuracy except for the simulations at

3.0 T. Statistical uncertainties at 3.0 T could not be achieved at 0.1% level at a single simulation because the simulations were stopped after negative  $u_{step}$  errors. This implied that the default EM macros of EGSnrc with a small EMULMT value cannot correctly transfer low-energy electrons especially in a strong magnetic field, where the Larmor radius of electrons was comparable to the substep size of electrons. However, we could achieve 0.1% of statistical uncertainties by the several uses of ‘restart’ option in EGSnrc. Based on the automatically terminated data, 0.01 MeV electrons at 3.0 T deposited the dose to the gas region 1% less than the theoretical value. We would not recommend to use the default electromagnetic field macro of EGSnrc at magnetic fields larger than 1.5 T.

Sempau and Andreo (28) designed the simplified geometry for the Fano cavity test without a magnetic field using PENELOPE. They achieved 0.4% accuracy with  $C1 = C2 = 0.02$  compared to the analogue simulation, not the theoretical values. In order to compare our results with this data, we additionally performed the single scattering mode by setting of  $C1 = C2 = W_{CC} = 0$  without a magnetic field. For 0.01, 0.1 and 1 MeV electrons, we achieved accuracy less than 0.1% in the analogue simulations, and these were almost equivalent to the previous data. However, the results of the Fano cavity test in the analogue simulations turned out to be within 0.5% compared to the theoretical values, which was comparatively larger than the results of EGSnrc. More studies are needed to figure out whether the boundary crossing algorithm or the condensed history algorithm affects the accuracy of PENELOPE. de Pooter et al. (32) tested mono-energetic electrons ranged from 0.5 to 4.0 MeV at 1.5 T, and reported that the accuracy of PENELOPE was within 0.3% on average and 1.0% in some cases. Especially for 1 and 3 MeV electrons, 0.1% and 0.6%

accuracy was achieved in their study, respectively. These are comparable to  $0.31 \pm 0.04\%$  and  $0.77 \pm 0.04\%$  accuracy of our results, respectively. Both studies showed that the larger electron energies were, the larger difference from the theoretical value of the Fano cavity theorem was found. Reynolds et al. (35) performed the Fano cavity test as a comparison between the results with and without a magnetic field. For 2 MeV electrons at 1.5 T, doses to the cylindrical ionization chamber increased by  $0.4 \pm 0.5\%$  compared to the corresponding doses without magnetic field. In this study for 1 and 3 MeV electrons at 1.5 T, the results of the Fano cavity test were  $-0.1 \pm 0.2\%$  and  $-0.1 \pm 0.4\%$ , respectively. These were because the simulation geometry was differed from each other: Reynolds et al. (35) used a cylindrical ionization chamber with the magnetic field parallel to the chamber axis and we selected a parallel plate ionization chamber with the magnetic field perpendicular to the chamber axis. Moreover, in this study the ionization chamber simulation in a magnetic field using PENELOPE needed a small DSMAX value, about  $1 \mu\text{m}$ , in order to achieve the similar results of the Fano cavity test without magnetic field. The values of C1 and C2 were set to 0.02 instead of the default value, 0.1, for comparison with the previous studies. When increasing the values of C1 and C2, the simulation efficiency was increased, however, the accuracy of the Fano cavity test was expected to decrease. The C1 and C2 were not sensitive to the results in this study. For 1 MeV electrons at 1.0 T, the accuracy of Fano cavity test with C1 = C2 = 0.1, 0.05, and 0.02 was  $0.27 \pm 0.02\%$ ,  $0.25 \pm 0.01\%$ , and  $0.26 \pm 0.04\%$ , respectively.

Up to now, there has been no comprehensive benchmark study to verify the accuracy of MCNP in a magnetic field. Koivunoro et al. (63) compared MCNP5 with EGSnrc and PENELOPE in the ionization chamber simulations without a magnetic

field, and the discrepancies were larger than 3% for electron energies less than 1 MeV. Even though they controlled the ESTEP values of 500, 2000, and 10000 for better accuracy, they concluded that the electron transport algorithm of MCNP5 was not accurate. However, we achieved an accuracy less than 0.4% in the Fano cavity test using MCNP6.1 after optimizing the ESTEP parameter. For 0.01 and 0.1 MeV electrons, the default ESTEP value of 3 for graphite was enough to pass 0.1% accuracy in the Fano cavity test. For 1 and 3 MeV electrons, we tried to find out the optimized ESTEP values because the default ESTEP value could not achieve an adequate accuracy. The results of the Fano cavity test were highly affected by the ESTEP value. When the  $efac = 0.99$ , the ESTEP of 90 for 1 MeV electrons and ESTEP of 70 for 3 MeV electrons achieved the highest accuracy of the Fano cavity test in the aforementioned geometries without and with a magnetic field of up to 3 T. The ESTEP value of 500 was too large to be achieved in the geometry and thus the Monte Carlo calculated doses were 9% smaller than the theoretical value.

A single scattering mode is available in MCNP6.1 only without a magnetic field. It is recommended to use the single scattering mode in the electron energies less than 1 keV as a default; however, it is also possible to apply the single scattering mode in the energies above 1 keV. A few studies compared the results from the single scattering mode of MCNP6 (64, 65) with the multiple scattering results. Like the previous studies, our results of the Fano cavity test using the single scattering mode showed better agreement within 0.1%. We additionally performed the simulations with the single scattering option turned on and off for energies less than 1 keV in the default energy indexing. There was negligible difference ( $< 0.03\%$ ) between two simulations.

Poon and Verhaegen (66) performed the simulations of an ionization chamber in water for 1.25 MeV photon beams without a magnetic field using Geant4. They controlled the step function parameters, such as the *dRoverRange* and *finalRange*. If the *dRoverRange* was set to 0.01, and the *finalRange* was set to 0.01  $\mu\text{m}$ , Fano cavity response was within 0.3%. O'Brien et al. (33) performed the Fano cavity test without a magnetic field and with a magnetic field of 1.5 T using Geant4. The simulation geometry was a cylindrical ionization chamber inside a spherical water phantom. The step function parameters, *dRoverRange* and *finalRange*, were set to 0.003 and 1 nm, respectively. The photon regeneration technique for eliminating scattered photons were used for polyenergetic photon source of the MR-linac. They compared the dose deposited in the cavity and the kerma in the wall. The relative differences between the dose to the Farmer-type ionization chamber and the kerma in the wall were within 0.1%. However, the deviations of our Fano cavity test without and with the magnetic field of 1.5 T using monoenergetic electrons from the theoretical value were within 1.4% and 1.7%, respectively. The Fano cavity response without a magnetic field for 1 MeV electrons was within 0.6%, which was comparable to the results from Poon et al. (27). The discrepancies between the previous and this studies can be attributed to the difference in the polyenergetic and monoenergetic electron sources used. The Fano cavity test with an isotropic electron line source per unit mass based on the reciprocal theorem would have better simulation uncertainties compared to the photon regeneration technique.

In general, helical trajectories of electrons by the Lorentz force increase the track lengths in the sensitive volume of ionization chamber, which in turn increase the chance of ionization and excitation in the volume. Accordingly, an ionization

chamber calibrated usually in no magnetic field needs a correction for this increases. The Larmor radii of helical trajectories were inversely proportional to the magnetic field strengths, and increased as increasing electron energies. However, the magnetic field strength that the maximum response of the three parallel plate ionization chambers occurred in this study was near 1.0 T rather than 1.5 T. The Farmer-type ionization chambers also revealed the maximum response at 0.8 to 1.0 T, depending on the radius of the sensitive volume (36, 39, 67). In principle, the track length of electron in the sensitive volume become a maximum when the Larmor radius of electron is equal to the height of the sensitive volume of parallel plate ionization chamber and to the radius of the sensitive volume of the Farmer-type ionization chamber. Thus, as seen in Figure 17, the magnetic field correction of ionization chambers strongly depends on the geometry and dimension of the chambers as well as the beam energy and magnetic field strength.

When the central axis of the central axis of ionization chambers, the beam direction, and the magnetic field are mutually orthogonal, the response of the parallel plate ionization chambers highly varied by the beam-quality. In 1.5 T, the  $k_B^Q$ -values of the NACP-02 for the Co-60, 6, and 10 MV beams ranged from 0.85 to 0.98, while those of the Farmer-type ionization chamber (NE2571) for the same beam qualities were between 0.98-0.99.14 The  $k_B^Q$ -values of the Farmer-type ionization chamber for a 7 MV photon beam in 1.5 T were 0.96-0.97 in the previous study (33), which was close to the  $k_B^Q = 0.96$  of the NACP-02 calculated in this study for the same configuration. However, for a 6 MV beam the  $k_B^Q$ -values of all three types of parallel plate ionization chambers in this study were lower than the values of the Farmer type

chamber, regardless of magnetic field strengths (36). This indicates that the parallel plate ionization chambers need more magnetic field correction than the Farmer-type ionization chambers. If the axis of the Farmer-type ionization chamber was aligned to the magnetic field direction, the  $k_B^Q$ -values for a Co-60 beam in 0.35 T and for the 7 MV beam in 1.5 T became larger than 0.98 (33, 40). However, there is a limitation on aligning the axis of the parallel plate ionization chamber along the magnetic field simultaneously perpendicular to the beam direction so that the magnetic field correction could not be reduced as much as in the Farmer-type ionization chamber. If the central axis of the Farmer-type and parallel plate ionization chambers was aligned with the beam direction simultaneously perpendicular to the magnetic field, the response of the Farmer-type ionization chambers was reduced by up to 12% for 6 MV beams (39), while that of parallel plate ionization chambers was increased by up to 12% for the same configuration. When the magnetic field direction was parallel to the beam direction, the  $k_B^Q$ -values of both Farmer-type and parallel plate ionization chambers were larger than 0.99 up to 1.5 T (33, 36, 40), which implied only a small correction i.e., less than 1% would be needed.

The collimated beams using photon energy spectra from the phase spaces used in this study were assumed to be uniform on the selected field size. However, real MR-linac systems have been developing using flattening filter free (FFF) beams in order to increase the dose rate (33). Recent study showed that the  $k_Q$ -values of the Farmer-type ionization chambers in a FFF beam were within 0.4% after a volume-averaging correction in the sensitive volume compared to those in a flattened beam (68).

## 5. Conclusions

In this study, the electron transport in a magnetic field using four general-purpose Monte Carlo codes (EGSnrc, PENELOPE, MCNP6 and Geant4) has been validated by the adapted Fano cavity theorem. Their accuracies for ionization chamber simulations in a magnetic field were evaluated using the adapted Fano cavity test. The accuracy of the adapted Fano cavity test was highly affected by the electron step size in all the codes, except for EGSnrc with the EEMF macros. EGSnrc with the EEMF macros implemented the adaptive multi-point integration algorithm, depending on the step size and introduced a specialized single scatter algorithm for the boundary crossing. With transport parameters carefully selected, PENELOPE and MCNP6 could achieve the adaptive Fano test accuracy of  $< 1\%$  for electron energies less than 1 MeV in the magnetic field strengths investigated in this study. Geant4 showed the adaptive Fano test accuracy of  $< 1.7\%$  except in 3.0 T. However, EGSnrc with the EEMF macros achieved the best accuracy among the four MC codes for the electron energies and the magnetic field strengths investigated in this study. Therefore, EGSnrc with the EEMF macros was recommended to simulate dose responses of ionization chambers in the presence of magnetic fields and used in the following MC simulations.

The responses and magnetic field correction factors of the three parallel plate ionization chambers in various magnetic field strengths were calculated for various photon beam energies. Unlike the Farmer-type ionization chambers, the  $k_B^Q$ -values of the parallel plate ionization chambers highly depended on the beam quality when the magnetic field was perpendicular to the beam direction. Such a large beam

quality dependence seemed to be caused by the thin-disk geometry of the sensitive volume accommodating curved trajectories of secondary electrons. Due to this large variation of  $k_B^Q$  on the beam quality, the parallel plate ionization chambers may not be recommended for reference dosimetry in a magnetic field perpendicular to the beam direction. However, the  $k_B^Q$ -values of the parallel plate ionization chambers in a magnetic field parallel to the beam direction were less than 1 % for the high-energy photon beams. The thin and flat geometry of parallel plate ionization chambers could be useful to measure the steep dose variation in the buildup region that may be even more perturbed in a magnetic field.

Owing to the high accuracy of MC codes, the magnetic field correction factors could be calculated as the beam quality conversion factors were calculated for the reference dosimetry of high-energy photon beams. These correction factors would be useful for radiation dosimetry in a magnetic field, especially for MRI-guided radiotherapy.

## **Appendix A. Feasibility of a Parallel Plate Ionization Chamber with Graphene Electrodes**

In this appendix, the feasibility of using graphene electrodes for a parallel plate ionization chamber was studied. However, the quality of the developed parallel plate ionization chambers with graphene electrodes was not enough to be a reference-class radiation dosimeter.

For the last few decades, various radiation dosimeters have been developed to measure absorbed doses and equivalents. They include ionization chambers (69), silicon semiconductor diodes (70), metal-oxide field effect transistors (MOSFET) (71), thermoluminescence dosimeters (TLDs) (72), and optically simulated luminescence dosimeters (OSLDs) (73). Among these dosimeters, air-filled ionization chambers have become a reference class dosimeter, which can measure the absorbed dose within a few-percent uncertainty using an appropriate calibration factor. Also, ionization chambers have a fairly uniform response to a wide range of radiation energy.

In the field of radiotherapy, the cylindrical ionization chamber is usually used for the reference dosimetry of electron beams with energies above 10 MeV, while the parallel plate ionization chamber is applicable at all electron energies (5, 74). For the reference dosimetry of photon beams, the use of cylindrical ionization chambers is mandatory; however, the parallel plate ionization chamber has an advantage of measuring the surface dose or depth dose curve due to its small size of the sensitive volume and thin entrance window. The international code of practice for dosimetry

IAEA TRS-398 recommends the use of parallel plate ionization chambers to measure photon percentage depth doses (74).

However, the physical size of ionization chambers limits the minimum depth of measurement in water and perturbs charge collection. In order to measure the absorbed doses using ionization chambers even in a magnetic field, an appropriate design and material of ionization chambers are needed. Although the design of parallel plate ionization chambers is sufficient to measure the surface doses and those in regions with sharp dose gradient, radiation fluence can be perturbed by their thickness of the entrance window. A small size of detectors would be preferable above all in the techniques of stereotactic radiotherapy, which operates on extremely little lesions by highly focused ionizing radiation beams. Or, a recently developing technique, MRI-guided radiotherapy also needs a small size of detectors to measure radiation dose in a magnetic field because electron trajectories highly affected by the Lorentz force should be tracked in a small step size with a high resolution (see Figure 18).

Usually, the electrodes of ionization chambers have been made of graphite due to its high electric conductivity and tissue-equivalence. The process of graphite is somewhat difficult because of its soft hardness. Some graphite was condensed for better hardness; however, high-density graphite could perturb radiation fluence more than normal-density graphite. Graphene is one of the most promising quasi-two-dimensional materials comprising a monolayer of  $sp^2$ -hybridized carbon atoms (75, 76). Graphene is in an emerging interest worldwide because of its astonishing physical properties (77), electron mobility (78), intrinsic strength (79), high thermal conductivity (80), optical absorption (81), impermeability to any gases (82), and

ability to sustain high densities of electric current (83). A thin layer of nano-scaled electrodes made of graphene could reduce the physical size of ionization chambers. With its electrical conductivity and affordable physical density, graphene can be an alternative to graphite as an electrode material of ionization chambers. These days, a monolayer of graphene is now commercially available and also can be produced in the laboratory (84, 85).

A thin layer of graphene has a low electrical conductivity compared to graphite. However, this low electrical conductivity does not matter for electrode material of ionization chambers because the collected charge from the ionization chambers in nano-coulomb unit cannot impact the applied voltage of electrometer in the ionization chamber region. A voltage drop in the graphene electrodes is almost negligible so that most of positive ions and electrons generated in the air cavity are collected by electrometer. Such being the case, the graphene electrodes in the ionization chambers can overcome the volume averaging effects caused by the relatively large sensitive volume of the ionization chambers.

A 3D printing technique has been advanced to develop complex devices. It enables small quantities of customized products to be fabricated at relatively low costs compared to mass customization or rapid prototyping (86). The products are built on a layer-by-layer basis using a plastic-based melting filament with a few hundred micrometers for each layer. Some filaments for 3D printing have an electrical conductivity, which can be applicable for electrodes and connecting wires. Therefore, it is possible to manufacture the customized parts of ionization chambers using a 3D printer.

Making a prototype using a 3D printer is cost effective compared to manufacturing by rapid computer numerical control (CNC) machining. While a 3D printer can cost as little as US Dollar \$10,000, a rapid prototype machine can cost as much as US Dollar \$500,000. Also, the production costs for the molds and casts are about a few thousand dollars, which can make only one product for each design. The total manufacturing cost for a graphene ionization chamber except for device purchasing costs in this study was expected as little as US Dollar \$100. It was much cheaper than buying a new parallel plate ionization chamber (\$4,000 in US Dollar). In that, it is very cost effective to develop a new device like a radiation detector using a 3D printing technique.

The purpose of this study is to develop an air-filled ionization chamber with monolayer graphene electrodes. Utilizing a 3D-printing technique, the frame of the ionization chamber was conveniently fabricated in user-specific designs, which cost much less than rapid prototyping technique using CNC machining and mold-and-cast methods. According to the main chapter in this thesis, an appropriate size and design of ionization chambers would be developed for dosimetry of MRI-guided radiotherapy. The prototype development of an ionization chamber with graphene electrodes using a 3D printer can optimize the design of ionization chambers inexpensively at laboratory level. With these manufacturing advantages, dosimetric characteristics of the graphene ionization chambers were investigated in comparison with a commercial graphite ionization chamber.

A parallel plate ionization chamber consists of two electrodes separated by a certain distance typically less than or equal to 0.2 cm. The gap between two electrodes is filled with gas or liquid in which ion pairs are created under radiation

and defines the sensitive volume of the chamber. A voltage is applied between the electrodes to generate an electric field in the gas region. When an ionizing radiation beam is incident to an ionization chamber, ion pairs are created, and the positive ions and electrons move to the electrodes under the influence of the electric field. The collected ions generate an ionization current, and are measured by an electrometer. The amount of accumulated charge is proportional to the number of ion pairs created as well as the radiation dose.

The parallel plate ionization chambers developed in this study have the outer wall and entrance window made of polylactic acid and graphene or carbon-loaded polyethylene collecting electrodes. These ionization chambers were benchmarked with the NACP-02 model (IBA dosimetry, Schwarzenbruck, Germany). The outer wall of the NACP-02 is composed of Poly(methyl methacrylate) (PMMA). It has a cylindrical outer shape with a radius of 1.5 cm and a height of 1.0 cm. The sensitive volume of NACP-02 model has also a cylindrical shape with a radius of 0.5 cm and a height of 0.2 cm, which has the sensitive volume of  $0.157 \text{ cm}^3$ . Its electrode and guard ring are made of graphite. It can be observed in Figure A1.

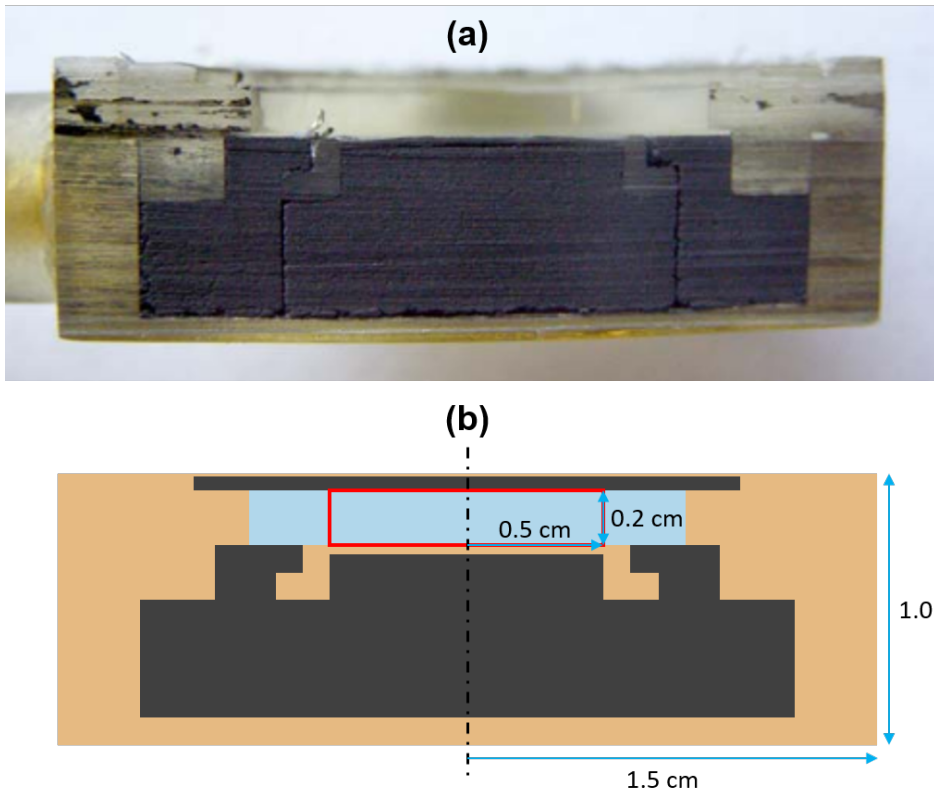
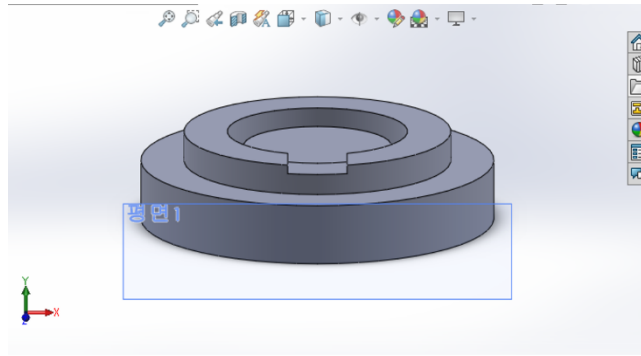
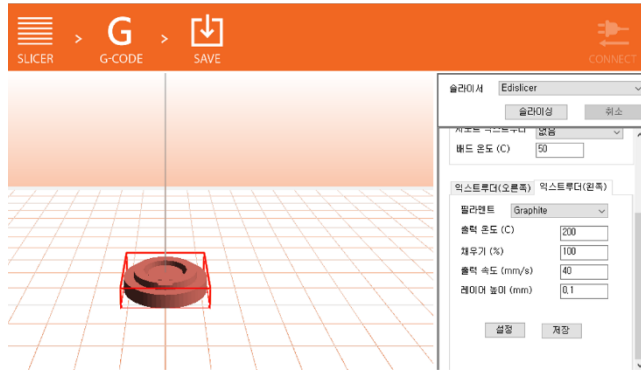


**Figure A1.** Cutting plane (a) and schematic diagram (b) of the NACP-02 geometry. The light orange parts are made of poly(methyl methacrylate) (PMMA), and the dark gray parts are made of graphite. The light blue color is an air cavity, and the red rectangle is the sensitive volume of the NACP-02. For the water-proof, a thin resin polyethylene terephthalate (PET) film covers the top of the entrance window.

A 3D printing allows the capability to construct a user-specific geometry. This study describes the feasibility of manufacturing an ionization chamber for radiation dosimetry. Each part of the parallel plate ionization chamber was drawn by a computer-aided design (CAD) tool, and the design was exported into a stereolithography (STL) file, which described the surface geometry of the three-dimensional object without color and texture. This format is the standard of 3D printing. Each STL file was converted into a G-code and x3g file for 3D printing using CreatorK software (Rokit, Seoul, Republic of Korea). A 3D printing was performed via fused deposition modeling (FDM) (87) on the 3DISON AEP model (Rokit, Seoul, Republic of Korea) (Figure A2). Polylactic acid (PLA, density 1.24 g/cm<sup>3</sup>) was used as a material of the outer chamber wall, electrode support, and entrance window (Rokit, Seoul, Republic of Korea). The guard ring was made of a conductive graphene PLA filament, which was the mixture of PLA and graphite (Black Magic 3D, Calverton, NY). The volume resistivity of the conductive graphene PLA filament was 0.6 Ohm·cm. The extruder temperatures for PLA and conductive graphene PLA filaments were 210°C and 200°C, respectively. The heat platform was warmed up at 75°C for the PLA filament and 50°C for the conductive graphene PLA filament. A printing speed was 40-60 mm/s.



(a) CAD (STL file)



(b) 3D printing software  
(gcode/x3g file)



(c) 3D printing

**Figure A2.** 3D printing process: Computer-aided design (CAD) for generating STL file (a), G-code generator for 3D printing (b), and fused deposition modeling (FDM) 3D printing (c).

Figures A3 and A4 describe the process to make the graphene electrodes for the parallel plate ionization chambers. First, a monolayer graphene on copper foil was grown in a chemical vapor deposition (CVD) system, consisting of a tubular quartz reactor and a furnace (84, 88). A layer of poly (methyl methacrylate) (PMMA) was deposited on the graphene layer by spin coating. The copper coil was etched away by an ammonium persulfate solution. The graphene-PMMA bilayer was scooped with a polyethylene terephthalate (PET) slide, and then transferred on a water to remove residual ammonium persulfate. The PMMA layer was removed by acetone. Using shadow masks, a patterned copper layer was deposited on the graphene layer by vacuum thermal evaporation (Figure A5).

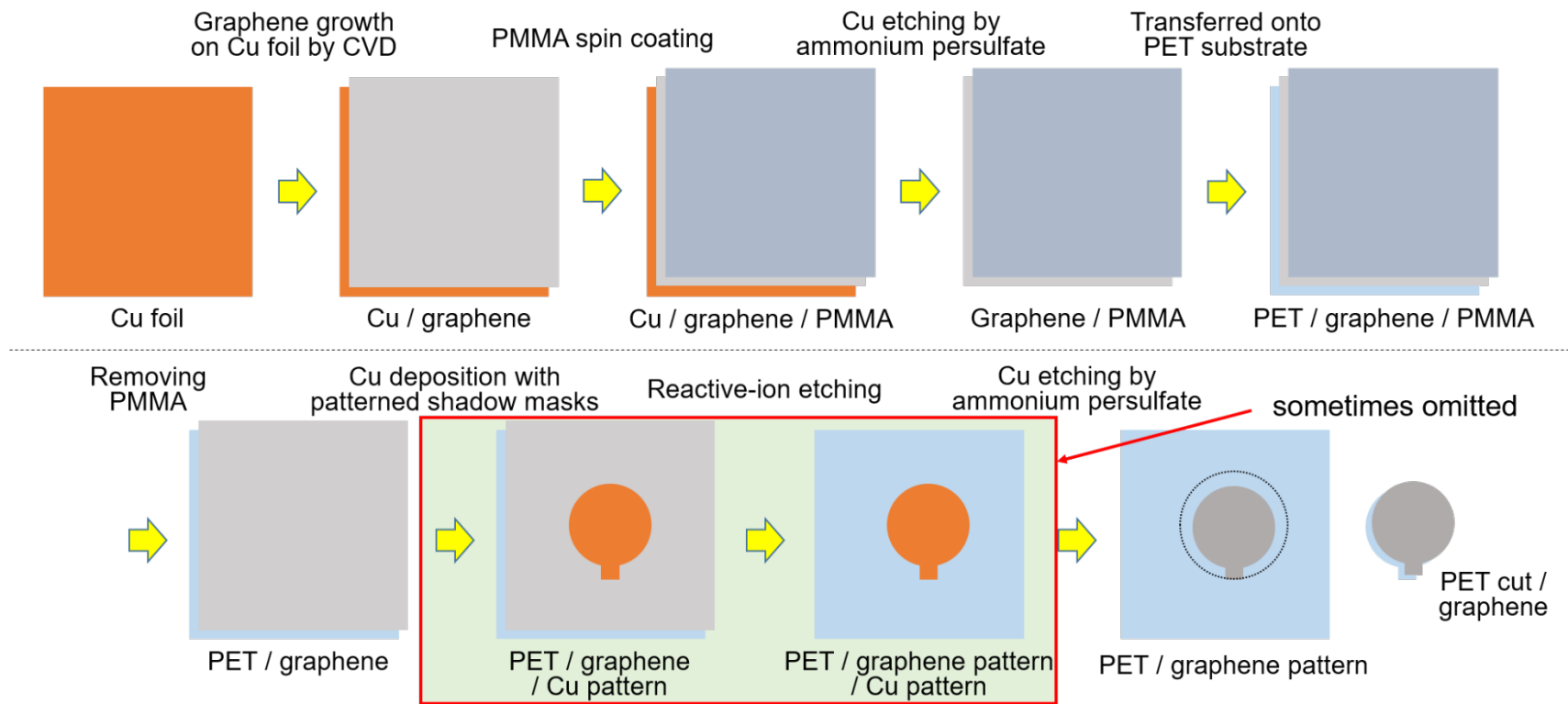


**Figure A3.** Schematic image of a patterned monolayer graphene.

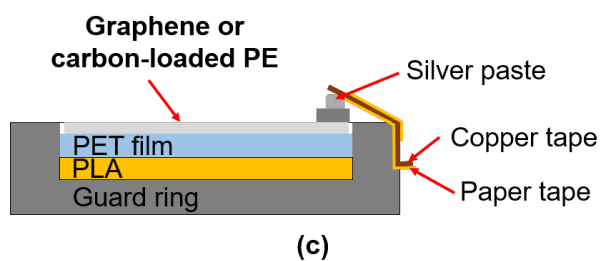
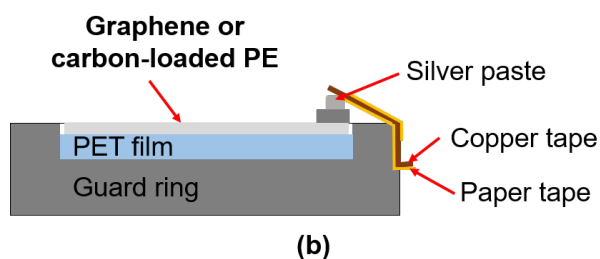
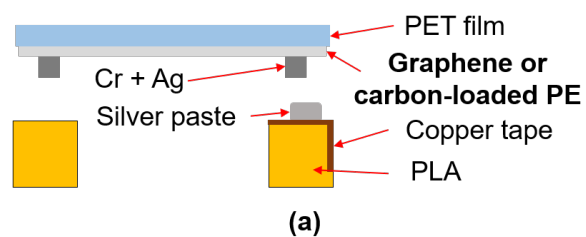


**Figure A4.** Diagram of top electrode (a), bottom electrodes (b)-(c) of the hand-made ionization chambers with graphene and carbon-loaded polyethylene electrodes.

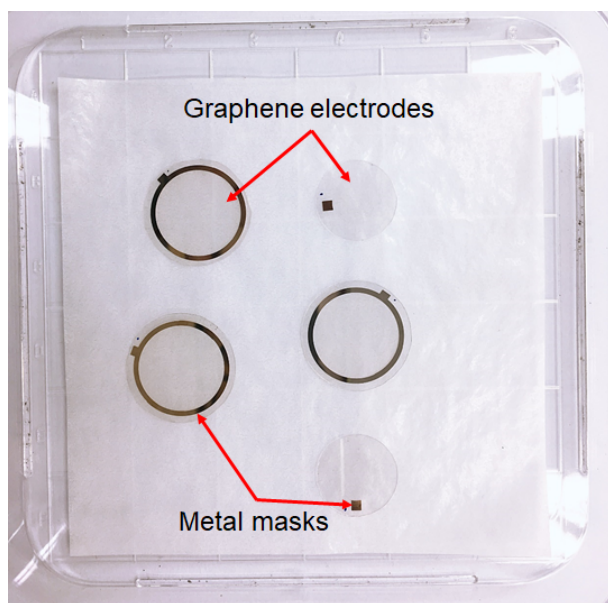


**Figure A5.** Graphene electrodes on a polyethylene terephthalate (PET) plate after metal coating using shadow masks for a wire connection.

In order to compare the performance between the graphene ionization chamber and the ionization chambers with a different material of the electrodes, we also fabricated the ionization chambers with the electrodes made of carbon-loaded polyethylene, which has a surface resistivity of 250 ohms-per-square (LINQSTAT XVCF 200 Ohms/sq 3.5 mil Conductive Film, Caplinq, USA). All dimensions of this ionization chamber were same as the graphene ionization chamber except for electrode material. The thickness of this conductive polyethylene film was 0.09 mm, and the specific gravity was 1.10-1.18.

Three thin wires of 0.2 mm diameter with sheath were used for the connection between the electrodes and guard ring. A copper tape was attached for a tight connection between the graphene electrodes and wires. Each strand of the wires was connected to the Belden 9222 tri-axial cable (Pomona Electronics Inc., WA, United States). A BNC (Bayonet Neill-Concelman)-type connector was used for the connection between the ionization chamber and electrometer. The inner conductor of the cable was connected to the bottom electrode of the graphene ionization chamber. The inner and outer shield layers were connected to the guard ring and top electrode of the graphene chamber, respectively. Each component of the 3D printed walls was assembled without glue. For developing the water-proof chamber, the gap between the tri-axial cable and wall of the ionization chamber was filled out using a glue gun. Figure A6 showed a full assembly of the graphene ionization chamber.

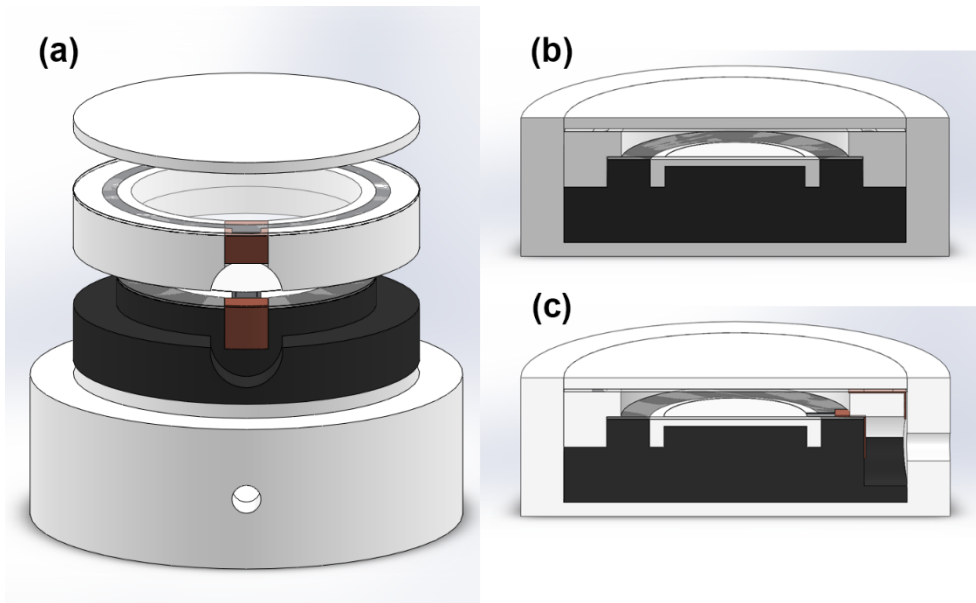


**Figure A6.** Assembly diagram of the 3D-printed graphene ionization chamber (a); the front view of the ionization chamber (b); the side view of the ionization chamber (c).

For radiation measurements, three types of the ionization chambers were used; the NACP-02 with graphite electrodes, ionization chambers with either graphene or carbon-loaded polyethylene electrodes. The performances of the ionization chambers were compared to each other.

The X-RAD 320 irradiator was used for a kilo voltaic energy beam (Precision X-Ray Inc., North Branford, CT) (Figure A7(a)). The x-ray tube in the X-RAD 320 provides a high output and uniform beam with a maximum output of 4,000 watts delivering up to 16 Gy per minute at a source to surface distance (SSD) of 50 cm. The X-RAD 320 was operated at 200 kVp and 20 mA with a 2.0-mm aluminum filter. The X-RAD 320 irradiator was calibrated at an SSD of 50 cm. Solid water slabs of 5 cm were piled up for the prevention of backscattered radiation, which is set up at an SSD of 50 cm. The ionization chamber was located upon the solid water slabs. The field size was a  $10 \times 10 \text{ cm}^2$  at the phantom surface.

The medical linear accelerator of Clinac<sup>®</sup> iX (Varian medical system, Palo Alto, CA) was also used to irradiate 6 and 10 MV photon and 6 and 9 MeV electron beams (Figure A7(b)). The ionization chamber was deposited on solid water slabs of 5 cm, located at an SSD of a 100 cm. The same field size as the kilo voltaic energy beam of  $10 \times 10 \text{ cm}^2$  at the phantom surface was used. The default dose rate was 600 monitor units (MUs) per minute.

The ionization chamber was connected to the UNIDOS<sup>®</sup> E electrometer (Physikalish-Technische Werkstätten (PTW), Freiburg, Germany) biased at +300 V to measure the charges generated by radiation in the sensitive volume of the ionization chamber. Each measurement was performed by more than 3 times for reliability. A leakage current was measured without radiation exposure and during a

time interval of 3 to 5 minutes. A dose linearity of the ionization chamber response was measured at a fixed dose rate of 20 mAs for the X-RAD 320 irradiator or 600 MUs per minute for the Clinac<sup>®</sup> iX in a field size of 10×10 cm<sup>2</sup>. The ionization chamber responses were evaluated in a range of 30 to 90 seconds for the X-RAD 320 irradiator and 100 to 300 MUs for the Clinac<sup>®</sup> iX. The dose rate dependence was also evaluated in the same set-up in a range of 5 to 20 mAs for the X-RAD 320 irradiator and 100 to 600 MUs per minute for the Clinac<sup>®</sup> iX. The polarity correction factors ( $P_{\text{pol}}$ ) and ion recombination correction factors ( $P_{\text{ion}}$ ) for pulsed beams were calculated as follows:

$$P_{\text{pol}} = \left| \frac{(M_{\text{raw}}^+ - M_{\text{raw}}^-)}{2M_{\text{raw}}} \right|, \quad (\text{A1})$$

and

$$P_{\text{ion}} = \frac{1 - V_{\text{H}}/V_{\text{L}}}{M_{\text{raw}}^{\text{H}}/M_{\text{raw}}^{\text{L}} - V_{\text{H}}/V_{\text{L}}}, \quad (\text{A2})$$

respectively, where the  $M_{\text{raw}}^+$  and  $M_{\text{raw}}^-$  are the raw electrometer readings at positive and negative voltage, respectively, and the  $M_{\text{raw}}^{\text{H}}$  and  $M_{\text{raw}}^{\text{L}}$  are the raw electrometer readings at high and low voltages, respectively, and the  $V_{\text{H}}$  and  $V_{\text{L}}$  are the high and low voltages, respectively. The  $M_{\text{raw}}^+$  and  $M_{\text{raw}}^-$  were measured at an applied voltage of +300 V and -300 V, respectively. Also, we selected  $V_{\text{H}} = +300$  V and  $V_{\text{L}} = +150$  V.

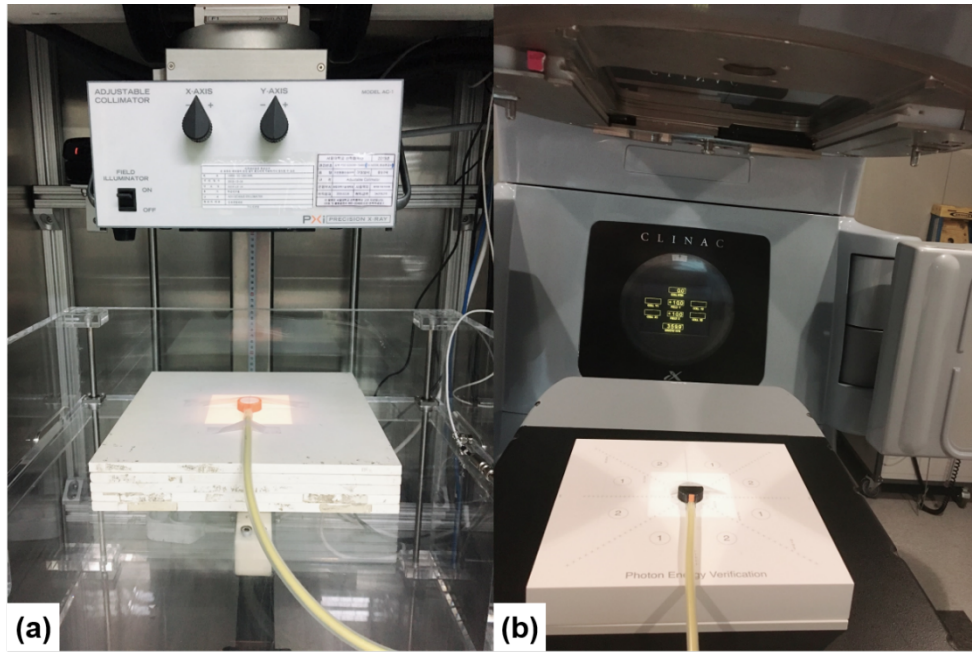


**Figure A7.** X-RAD 320 irradiator for a kilo voltaic x-ray beam (a) and Clinical medical linear accelerator for mega voltaic photon and electron beams (b).

The performance of the ionization chambers developed in this study was verified by the characterization tests of: leakage current without irradiation, dose linearity, dose rate dependence, saturation, polarity effect, and ion recombination effect.

The IEC 60731 (IEC, International Electrotechnical Commission (89)) recommends a limit of 0.5% of the highest measured value during an irradiation for the leakage current test. The developed ionization chambers showed twice or three times higher leakage current compared to the NACP-02 without zeroing process. However, the leakage current of each developed ionization chamber was within the expected limit after zeroing (Figure A8).

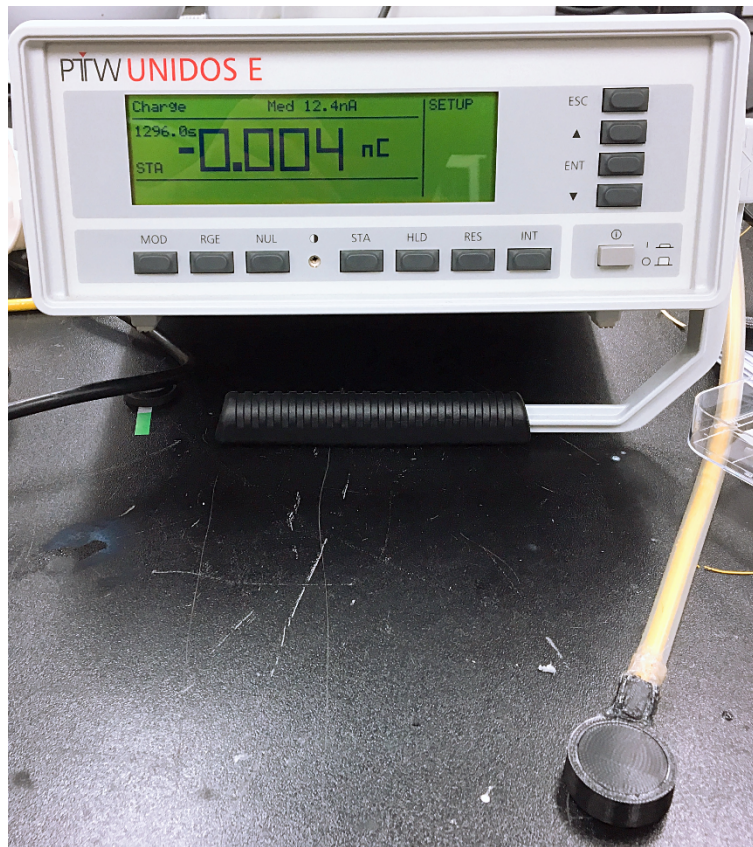


**Figure A8.** Leakage current of the graphene ionization chamber at an applied voltage of +300 V after zeroing during 50 seconds. It was almost negligible for the collected charge.

Figures A9 and A10 showed the linearity between the responses of the ionization chambers and absorbed dose. All of the ionization chambers had a good dose linearity to be applied to radiation dosimetry with a single dose calibration factor. All of the coefficient of determination ( $R^2$ ) for the linear least-squares fitting were 1.000. The collected charges of the home-made ionization chambers were 0.92 to 5.3 times for a kilo voltaic x-ray beam and 1.4 to 2.4 times for mega voltaic photon and electron beams larger than the collected charges of the NACP-02.

There might be some possible causes of different radiation sensitivity. Some graphene ionization chambers used a circular PET plate cut by hand in order to fit the size of the 3D-printed guard ring. The different size of graphene on the PET plate made different sensitive volumes of the ionization chambers (Figures A9(a)-(b) and A10(a)-(b)). The second cause is the resistance between electrodes and the electrometer. There could be a voltage drop on the wire connection because we simply inserted thin wires into each layer of the tri-axial cable. The sensitivity of one carbon-loaded polyethylene ionization chamber for a 200 kVp beam was similar to that of the NACP-02, while it was increased by 1.4 to 2.0 times higher than those of the NACP-02 for mega voltaic photon and electron beams (Figures A9(c) and A10(c)). If each electrode was not tightly connected to the tri-axial cable, the sensitivity of the ionization chambers was decreased. The other possible cause is dose enhancement by the copper tape and silver paste at the junction between the electrode and wire. The thin coated layers of chrome and silver at the top and bottom electrodes was not effective due to their thin thickness of 100 nm; however, the copper tape of 50  $\mu\text{m}$  and a lump of silver paste can generate more electrons by Compton and photoelectric effects compared to the graphene and chamber wall for

a kilo voltaic beam. The fringing electric field at the edges of the electrode may also increase the sensitivity of ionization chambers if the guard ring cannot prevent electrons to enter the sensitive volume. The volume of total air cavity in the ionization chambers was 2.56 times larger than the sensitive volume of the ionization chambers. It was similar to the sensitivity enhancement by the developed ionization chambers for mega voltaic photon and electron beams. The electrons entering into the air cavity on the guard ring could be collected by the electrodes due to the irregular electric field. In that, we could guess this sensitivity enhancement was caused by the malfunction of the guard ring. Further study is needed to figure out which is the main reason to affect the sensitivity of ionization chambers.

There was almost no dose rate dependence on the NACP-02; however, some graphene or carbon-loaded polyethylene chambers showed small dose rate dependence (Figures A11 and A12).

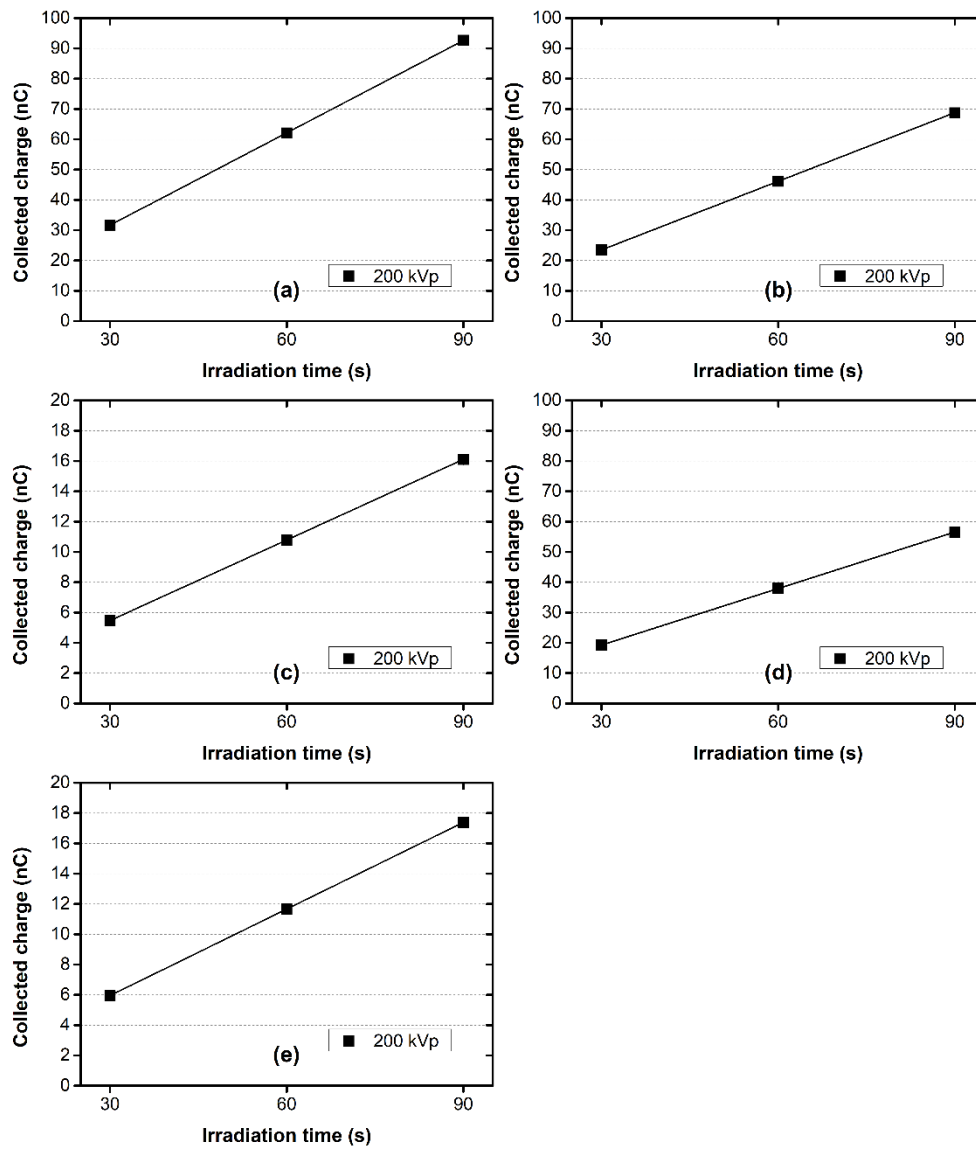


**Figure A9.** Linearity between the absorbed dose and the collected charge of the ionization chambers with graphene electrodes (a)-(b) and with carbon-loaded polyethylene electrodes (c)-(d), and the NACP-02 (e) for a kilo voltaic x-ray beam of 200 kVp.

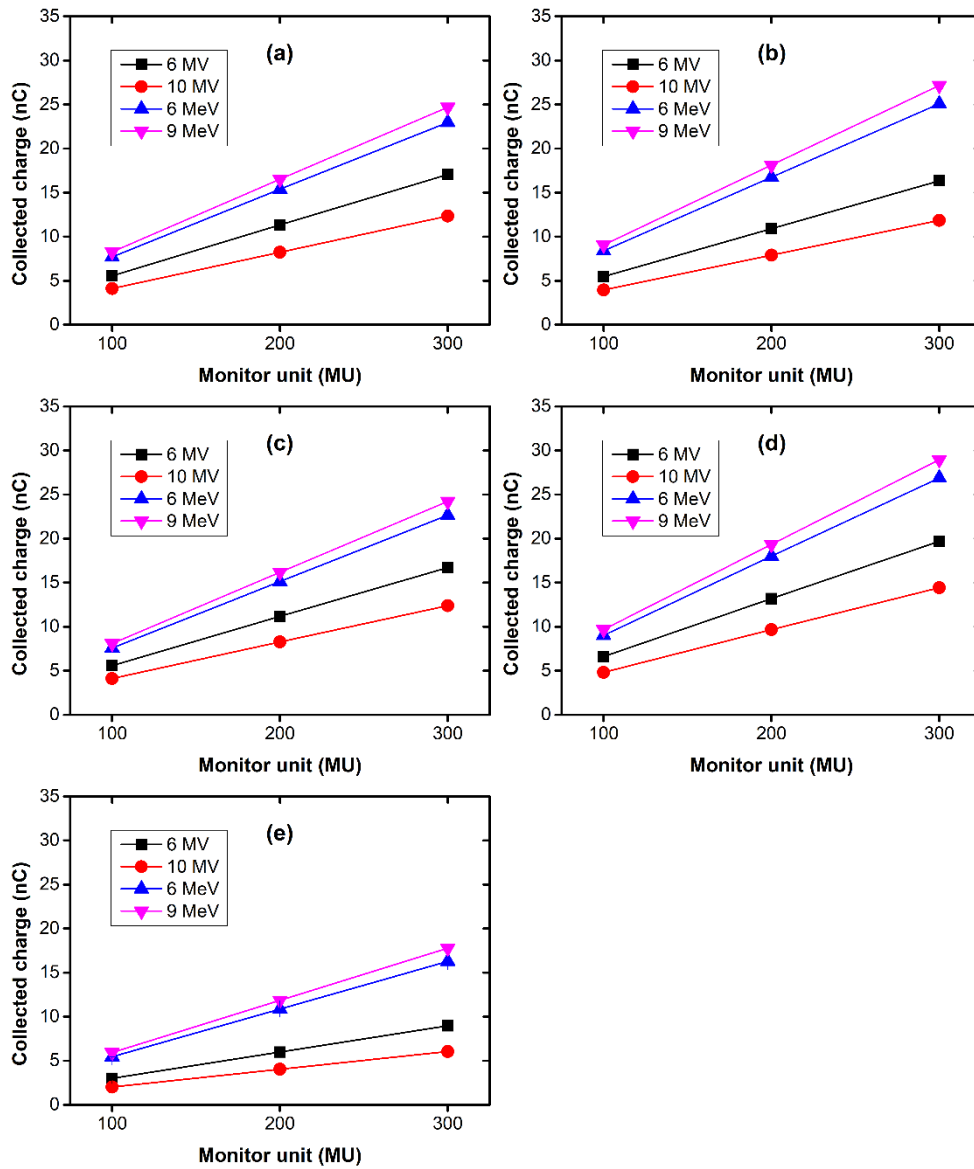


**Figure A10.** Linearity between the absorbed dose and the collected charge of the ionization chambers with graphene electrodes (a)-(b) and with carbon-loaded polyethylene electrodes (c)-(d), and the NACP-02 (e) for mega voltaic photon and electron beams.

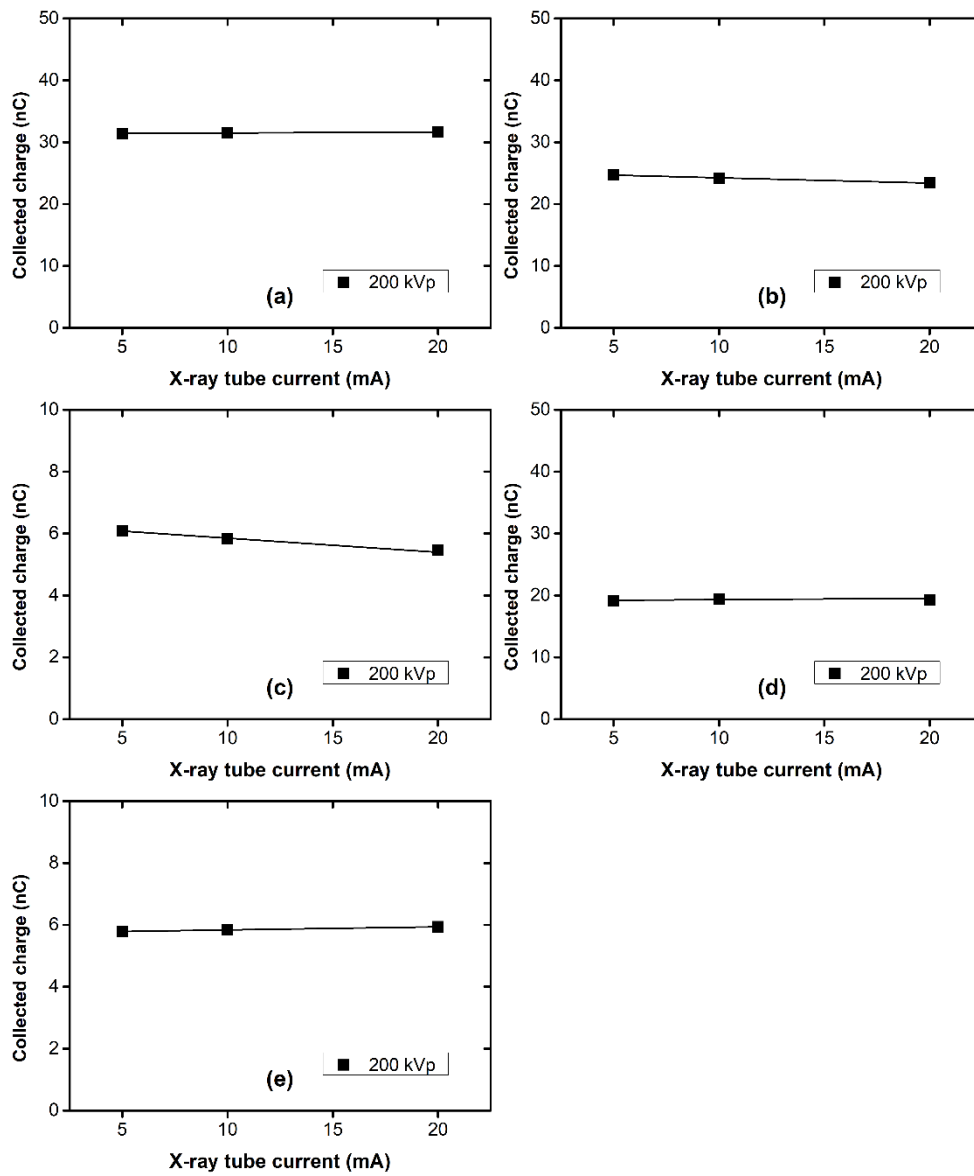


**Figure A11.** Dose rate dependence of the ionization chambers with graphene electrodes (a)-(b) and with carbon-loaded polyethylene electrodes (c)-(d), and the NACP-02 (e) for a kilo voltaic x-ray beam of 200 kVp.

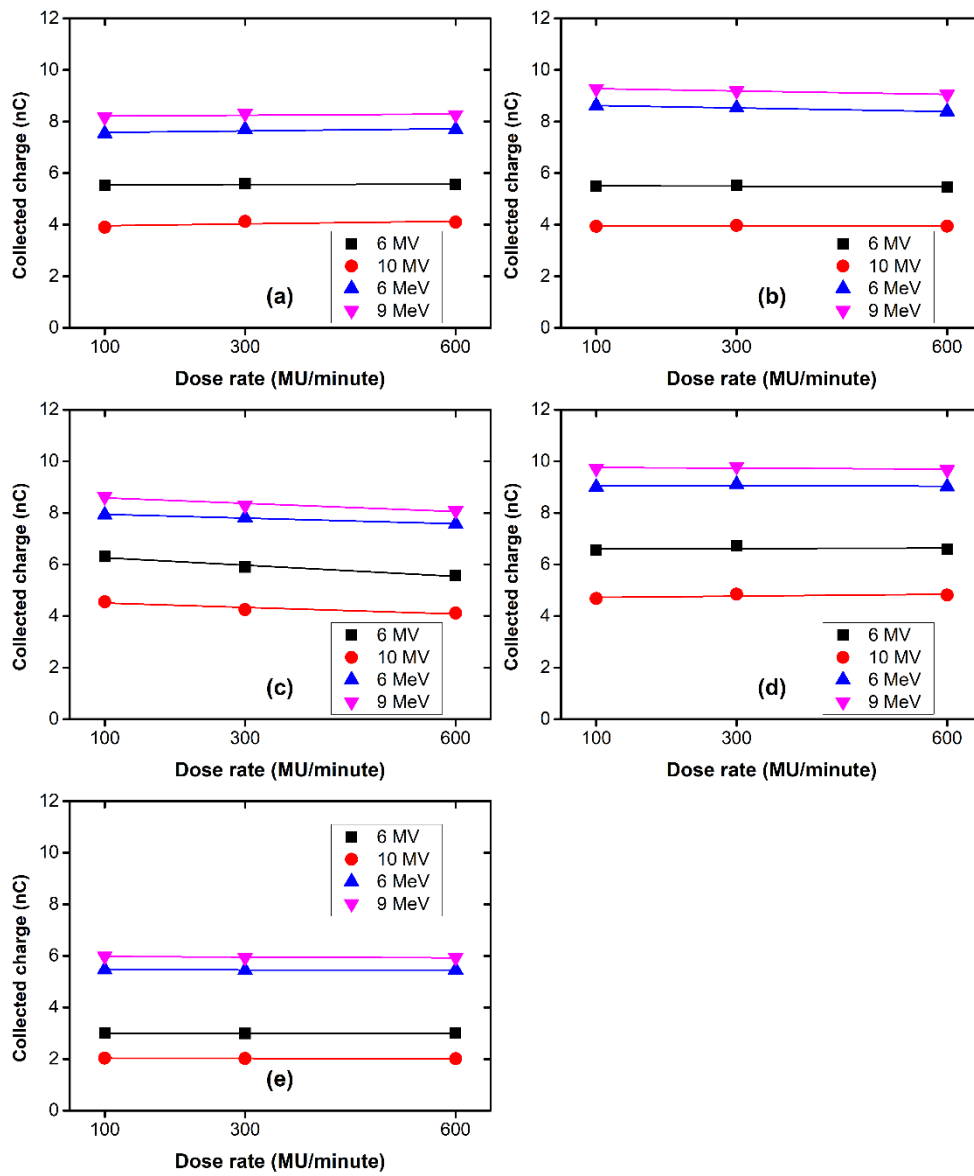


**Figure A12.** Dose rate dependence of the ionization chambers with graphene electrodes (a)-(b) and with carbon-loaded polyethylene electrodes (c)-(d), and the NACP-02 (e) for mega voltaic photon and electron beams.

Figures A13 and A14 showed the current-voltage characteristics of the ionization chambers with graphene and carbon-loaded polyethylene electrodes, and the NACP-02. The charges produced by radiation were collected after applying an applied voltage ranged from -400 V to +400 V. The dots at an applied voltage of 0 V were also added to estimate how many charges were collected without an electric field. Unlike commercialized ionization chambers like the NACP-02 model, the graphene and carbon-loaded polyethylene ionization chambers have unflatten regions in the ionization chamber region. Both types of home-made ionization chambers were not saturated even at 400 V, which is the voltage limitation of the electrometer we used. Generally, the ionization chamber reading was saturated in the ionization chamber region ranged from 100 V to 400 V; however, the collected charges of the hand-made ionization chambers were not saturated even at an applied voltage of 400 V.

As increasing the applied voltage of electrodes in the ionization chamber region, the collected charge could reach its saturation value of ionization. The Jaffé plots of the developed ionization chambers showed a linear trend (Figure A15) (90). If a strong deviation from this linearity occurred at the highest voltage, the saturation curve does not correspond to a true saturation curve. The fitting lines in the Jaffé plots have a positive gradient in the graph. This indicates that the ion collection efficiency increases with increasing the applied voltage, and keeps approaching the saturated value. Also, some home-made ionization chambers in the previous studies showed the saturation region at an applied voltage larger than 300 or 500 V (91-93).

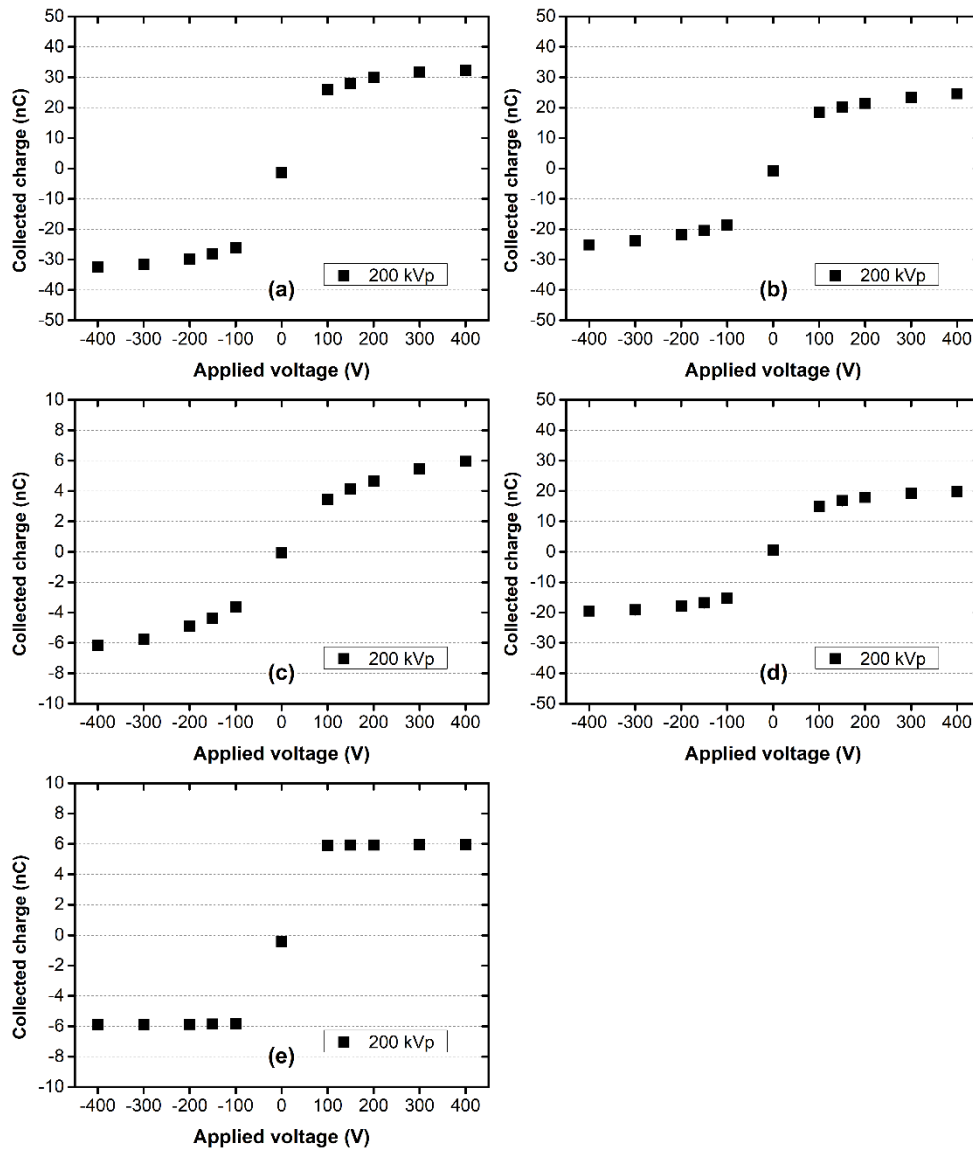


**Figure A13.** Current-voltage characteristics of the ionization chambers with graphene electrodes (a)-(b) and with carbon-loaded polyethylene electrodes (c)-(d), and the NACP-02 (e) for a kilo voltaic x-ray beam of 200 kVp.

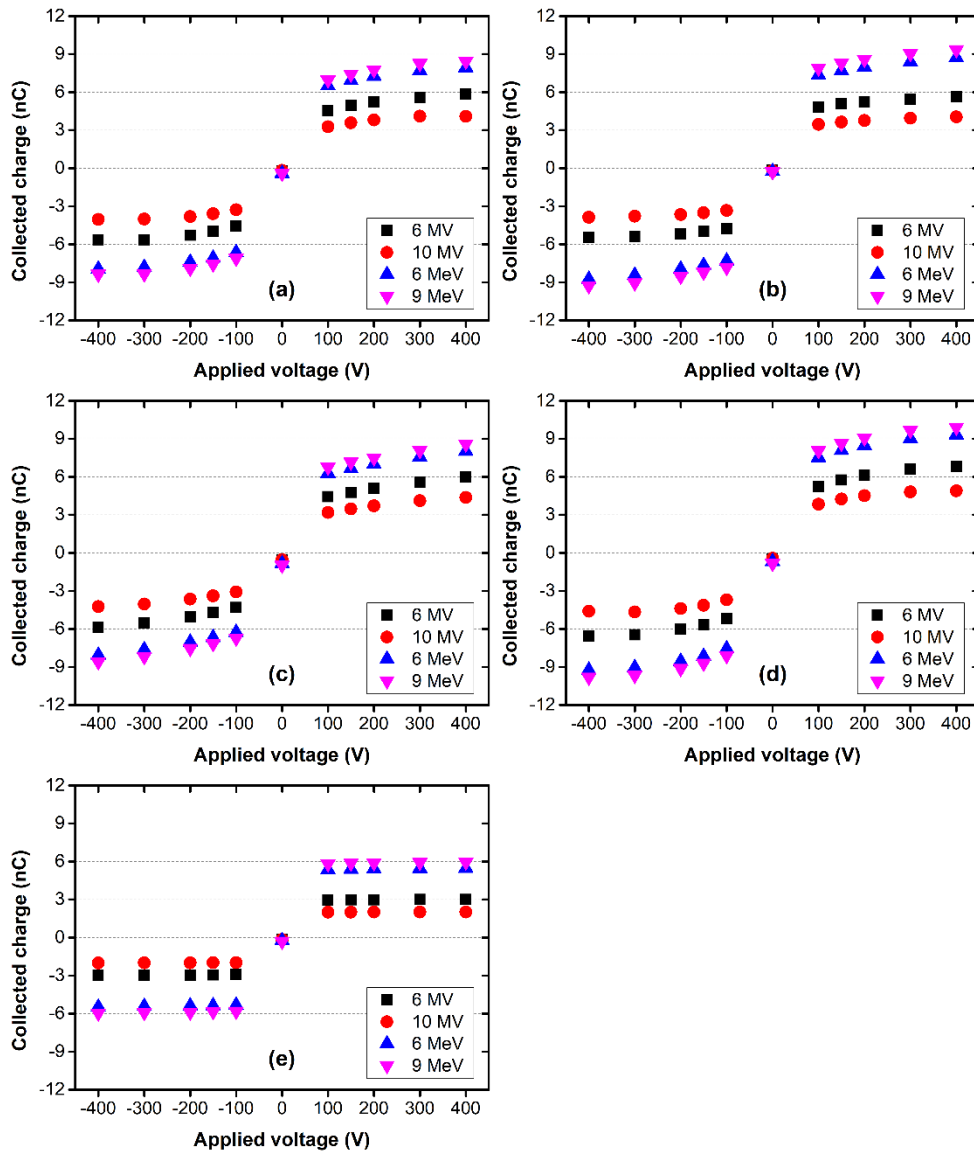


**Figure A14.** Current-voltage characteristics of the ionization chambers with graphene electrodes (a)-(b) and with carbon-loaded polyethylene electrodes (c)-(d), and the NACP-02 (e) for mega voltaic photon and electron beams.

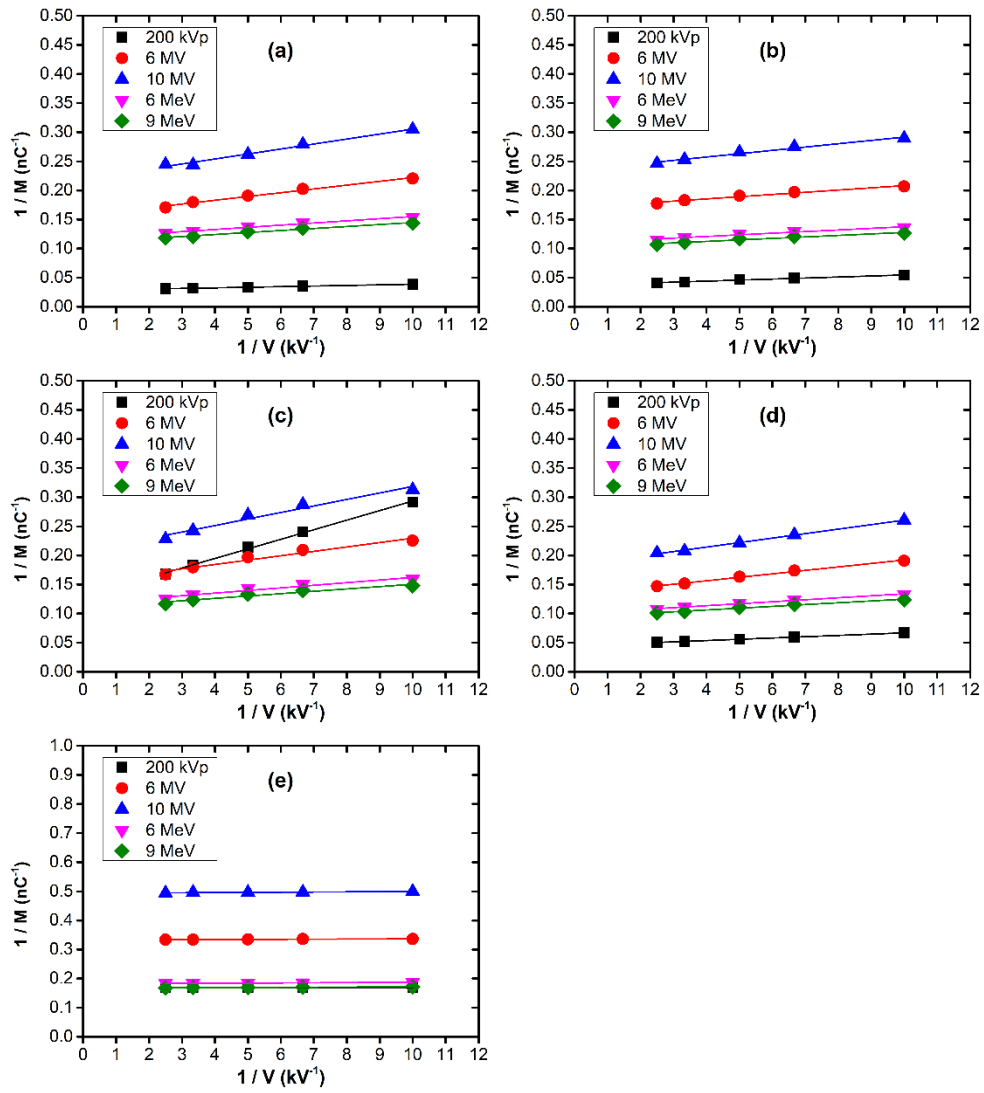


**Figure A15.** Jaffé plots of the ionization chambers with graphene electrodes (a)-(b) and with carbon-loaded polyethylene electrodes (c)-(d), and the NACP-02 (e).

Tables A1 and A2 showed the polarity and ion recombination correction factors for the ionization chambers with graphene electrodes and carbon-loaded polyethylene electrodes, and the NACP-02. The home-made ionization chambers with graphene and carbon-loaded polyethylene electrodes showed reasonable polarity correction factors less than 2.7% for all kinds of beam energies. However, the ion recombination correction factors for these developed ionization chambers had larger values than the polarity correction factors. The graphene ionization chambers showed  $P_{\text{ion}}$  of 8.3-18.8%, while the carbon-loaded polyethylene ionization chambers showed  $P_{\text{ion}}$  of 13.0-45.5%. This phenomenon may be caused by the heterogeneous electric field between two electrodes. It was hard to handle a very thin graphene layer, so the sizes of graphene electrodes were not fit to the guard ring located just outside of the bottom electrode. There may be the gap between the bottom electrode and guard ring, which generates the fringing electric field at the edge of the electrode. If the collected charge reaches its saturation value at the applied voltage of 500 to 1000 V, this large ion recombination effect could be reduced. The NACP-02 has both the polarity and ion recombination correction factors less than 2%.

**Table A1.** Polarity correction factors ( $P_{\text{pol}}$ ) for the ionization chambers with graphene electrodes and with carbon-loaded polyethylene electrodes, and the NACP-02.

	$P_{\text{pol}}$				
	200 kVp X-ray	6 MV photon	10 MV photon	6 MeV electron	9 MeV electron
Graphene electrodes	$1.000 \pm 0.005$	$1.007 \pm 0.026$	$0.982 \pm 0.029$	$1.008 \pm 0.006$	$1.001 \pm 0.014$
	$1.009 \pm 0.013$	$0.993 \pm 0.007$	$0.979 \pm 0.027$	$1.003 \pm 0.003$	$1.000 \pm 0.004$
Carbon-loaded polyethylene electrodes	$1.027 \pm 0.015$	$0.997 \pm 0.016$	$0.986 \pm 0.027$	$1.004 \pm 0.002$	$1.003 \pm 0.015$
	$1.002 \pm 0.004$	$0.989 \pm 0.004$	$0.983 \pm 0.004$	$1.002 \pm 0.002$	$0.999 \pm 0.003$
NACP-02	$0.995 \pm 0.012$	$0.995 \pm 0.002$	$0.995 \pm 0.000$	$0.997 \pm 0.003$	$0.998 \pm 0.002$

**Table A2.** Ion recombination correction factors ( $P_{\text{ion}}$ ) for the ionization chambers with graphene electrodes and with carbon-loaded polyethylene electrodes, and the NACP-02.

	$P_{\text{ion}}$				
	200 kVp X-ray	6 MV photon	10 MV photon	6 MeV electron	9 MeV electron
Graphene electrodes	$1.146 \pm 0.008$	$1.142 \pm 0.010$	$1.183 \pm 0.016$	$1.129 \pm 0.008$	$1.128 \pm 0.002$
	$1.188 \pm 0.005$	$1.083 \pm 0.002$	$1.094 \pm 0.003$	$1.097 \pm 0.003$	$1.101 \pm 0.001$
Carbon-loaded polyethylene electrodes	$1.455 \pm 0.007$	$1.198 \pm 0.005$	$1.230 \pm 0.007$	$1.160 \pm 0.001$	$1.148 \pm 0.002$
	$1.158 \pm 0.003$	$1.173 \pm 0.002$	$1.155 \pm 0.001$	$1.130 \pm 0.003$	$1.136 \pm 0.001$
NACP-02	$1.002 \pm 0.005$	$1.006 \pm 0.001$	$1.002 \pm 0.001$	$1.013 \pm 0.001$	$1.010 \pm 0.000$

The prototype parallel plate ionization chambers with monolayer graphene or carbon-loaded polyethylene electrodes have been successfully developed. The hand-made ionization chambers can be applied to measure the absorbed dose for a x-ray beam of a kilo voltaic energy and photon and electron beams of mega voltaic energies. With the nano-scaled thin electrodes made of graphene, there is a potential to reduce the perturbation by the entrance window or wall and the physical limitation of the surface dose measurements. Most parts of the hand-made ionization chambers were fabricated by a 3D printing technique. This is an important trial because it allows the development of ionization chambers with a customized dimension, which can improve a spatial resolution. Also, it would satisfy adequate purposes of radiation measurements like dosimetry of MR-linac. With relatively cheap developing costs, it may be efficiently used for radiation dosimetry as well as biological experiments.

## Bibliography

1. Podgorsak EB. *Radiation oncology physics: a handbook for teachers and students*. Vienna: International Atomic Energy Agency; 2005.
2. *SSDL NETWORK CHARTER. THE IAEA/WHO NETWORK OF SECONDARY STANDARDS DOSIMETRY LABORATORIES*. 2nd ed. Vienna: INTERNATIONAL ATOMIC ENERGY AGENCY; 2017.
3. Muir BR, McEwen MR, Rogers DWO. Beam quality conversion factors for parallel-plate ionization chambers in MV photon beams. *Med Phys*. 2012;39(3):1618-1631.
4. Abdel-Rahman W, Seuntjens JP, Verhaegen F, Deblois F, Podgorsak EB. Validation of Monte Carlo calculated surface doses for megavoltage photon beams. *Med Phys*. 2005;32(1):286-298.
5. Almond PR, Biggs PJ, Coursey BM, Hanson W, Huq MS, Nath R, et al. AAPM's TG-51 protocol for clinical reference dosimetry of high-energy photon and electron beams. *Med Phys*. 1999;26(9):1847-1870.
6. Lagendijk JJ, Raaymakers BW, Raaijmakers AJ, Overweg J, Brown KJ, Kerkhof EM, et al. MRI/linac integration. *Radiother Oncol*. 2008;86(1):25-29.
7. Fallone BG, Murray B, Rathee S, Stanescu T, Steciw S, Vidakovic S, et al. First MR images obtained during megavoltage photon irradiation from a prototype integrated linac-MR system. *Med Phys*. 2009;36(6):2084-2088.
8. Mutic S, Dempsey JF. The ViewRay system: Magnetic resonance-guided and controlled radiotherapy. *Semin Radiat Oncol*. 2014;24(3):196-199.
9. Keall PJ, Barton M, Crozier S. The Australian magnetic resonance imaging–linac program. *Semin Radiat Oncol*. 2014;24(3):203-206.

10. Baillie D, Aubin JS, Fallone BG, Steciw S. Feasibility of producing a short, high energy s-band linear accelerator using a klystron power source. *Med Phys.* 2013;40(4):041713.
11. Baillie D, Aubin JS, Fallone B, Steciw S. FEM design and simulation of a short, 10 MV, S-band Linac with Monte Carlo dose simulations. *Med Phys.* 2015;42(4):2044-2053.
12. Baillie D, Fallone BG, Steciw S. Design and simulation of a short, variable-energy 4 to 10 MV S-band linear accelerator waveguide. *Med Phys.* 2017;44(6):2124-2131.
13. Ye S-J, Brezovich IA, Pareek P, Naqvi SA. Benchmark of PENELOPE code for low-energy photon transport: dose comparisons with MCNP4 and EGS4. *Phys Med Biol.* 2004;49(3):387-397.
14. Vilches M, Garcia-Pareja S, Guerrero R, Anguiano M, Lallena A. Monte Carlo simulation of the electron transport through thin slabs: A comparative study of PENELOPE, GEANT3, GEANT4, EGSnrc and MCNPX. *Nucl Instrum Methods Phys Res B.* 2007;254(2):219-230.
15. Vilches M, Garcia-Pareja S, Guerrero R, Anguiano M, Lallena A. Monte Carlo simulation of the electron transport through air slabs: A comparative study of PENELOPE, GEANT3, Geant4 and EGSnrc Monte Carlo codes. *IEEE Trans Nucl Sci.* 2008;55(2):710-716.
16. Nettelbeck H, Takacs GJ, Rosenfeld AB. Effect of transverse magnetic fields on dose distribution and RBE of photon beams: comparing PENELOPE and EGS4 Monte Carlo codes. *Phys Med Biol.* 2008;53(18):5123-5137.
17. Yoriyaz H, Moralles M, de Tarso Dalledone Siqueira P, da Costa Guimarães C, Belonsi Cintra F, Dos Santos A. Physical models, cross sections, and numerical approximations used in MCNP and GEANT4 Monte Carlo codes for photon and electron absorbed fraction calculation. *Med Phys.* 2009;36(11):5198-5213.

18. Maigne L, Perrot Y, Schaart D, Donnarieix D, Breton V. Comparison of GATE/GEANT4 with EGSnrc and MCNP for electron dose calculations at energies between 15 keV and 20 MeV. *Phys Med Biol*. 2011;56(3):811-827.
19. Champion C, Incerti S, Perrot Y, Delorme R, Bordage M-C, Bardiès M, et al. Dose point kernels in liquid water: an intra-comparison between GEANT4-DNA and a variety of Monte Carlo codes. *Appl Radiat Isot*. 2014;83:137-141.
20. Archambault JP, Mainegra-Hing E. Comparison between EGSnrc, Geant4, MCNP5 and Penelope for mono-energetic electron beams. *Phys Med Biol*. 2015;60(13):4951-4962.
21. Kawrakow I, Rogers DWO. *The EGSnrc code system: Monte Carlo simulation of electron and photon transport*. National Research Council Canada. NRCC Report PIRS-701, 2000.
22. Baro J, Sempau J, Fernández-Varea J, Salvat F. PENELOPE: an algorithm for Monte Carlo simulation of the penetration and energy loss of electrons and positrons in matter. *Nucl Instrum Methods Phys Res B*. 1995;100(1):31-46.
23. Pelowitz DB, Goorley JT, Fensin ML, McKinney GW, James MR, Forster RA, et al. *MCNP6™ User's Manual Version 1.0*. Los Alamos National Laboratory. LA-CP-13-00634, 2013.
24. Agostinelli S, Allison J, Amako K, Apostolakis J, Araujo H, Arce P, et al. GEANT4—a simulation toolkit. *Nucl Instrum Methods Phys Res A*. 2003;506(3):250-303.
25. Fano U. Note on the Bragg-Gray cavity principle for measuring energy dissipation. *Radiat Res*. 1954;1(3):237-240.
26. Kawrakow I. Accurate condensed history Monte Carlo simulation of electron transport. II. Application to ion chamber response simulations. *Med Phys*. 2000;27(3):499-513.

27. Poon E, Seuntjens J, Verhaegen F. Consistency test of the electron transport algorithm in the GEANT4 Monte Carlo code. *Phys Med Biol.* 2005;50(4):681-694.
28. Sempau J, Andreo P. Configuration of the electron transport algorithm of PENELOPE to simulate ion chambers. *Phys Med Biol.* 2006;51(14):3533-3548.
29. Yi CY, Hah SH, Yeom MS. Monte Carlo calculation of the ionization chamber response to Co60 beam using PENELOPE. *Med Phys.* 2006;33(5):1213-1221.
30. Bouchard H, Bielajew A. Lorentz force correction to the Boltzmann radiation transport equation and its implications for Monte Carlo algorithms. *Phys Med Biol.* 2015;60(13):4963-4971.
31. Bouchard H, de Pooter J, Bielajew A, Duane S. Reference dosimetry in the presence of magnetic fields: conditions to validate Monte Carlo simulations. *Phys Med Biol.* 2015;60(17):6639-6654.
32. De Pooter JA, De Prez LA, Bouchard H. Application of an adapted Fano cavity test for Monte Carlo simulations in the presence of B-fields. *Phys Med Biol.* 2015;60(24):9313-9327.
33. O'Brien DJ, Roberts DA, Ibbott GS, Sawakuchi GO. Reference dosimetry in magnetic fields: formalism and ionization chamber correction factors. *Med Phys.* 2016;43(8):4915-4927.
34. Malkov VN, Rogers DWO. Charged particle transport in magnetic fields in EGSnrc. *Med Phys.* 2016;43(7):4447-4458.
35. Reynolds M, Rathee S, Fallone BG. Ion Chamber Angular Dependence in a Magnetic Field. *Med Phys.* 2017;44(8):4322-4328.
36. Spindeldreier CK, Schrenk O, Bakenecker A, Kawrakow I, Burigo L, Karger CP, et al. Radiation dosimetry in magnetic fields with Farmer-type ionization chambers: determination of magnetic field correction factors for different magnetic field strengths and field orientations. *Phys Med Biol.* 2017;62(16):6708-6728.

37. Meijssing I, Raaymakers BW, Raaijmakers AJE, Kok JGM, Hogeweg L, Liu B, et al. Dosimetry for the MRI accelerator: the impact of a magnetic field on the response of a Farmer NE2571 ionization chamber. *Phys Med Biol.* 2009;54(10):2993-3002.
38. Smit K, Van Asselen B, Kok JGM, Aalbers AHL, Lagendijk JJW, Raaymakers BW. Towards reference dosimetry for the MR-linac: magnetic field correction of the ionization chamber reading. *Phys Med Biol.* 2013;58(17):5945-5957.
39. Reynolds M, Fallone BG, Rathee S. Dose response of selected ion chambers in applied homogeneous transverse and longitudinal magnetic fields. *Med Phys.* 2013;40(4):042102.
40. Malkov VN, Rogers DW. Monte Carlo study of ionization chamber magnetic field correction factors as a function of angle and beam quality. *Med Phys.* 2017;45(2):908-925.
41. Pojtinger S, Dohm OS, Kapsch R-P, Thorwarth D. Ionization chamber correction factors for MR-linacs. *Phys Med Biol.* 2018;63(11):11NT03.
42. Carlone M, Tadic T, Keller H, Rezaee M, Jaffray D. Enhancing the surface dose using a weak longitudinal magnetic field. *Med Phys.* 2016;43(6Part1):2927-2932.
43. Chibani O, Moftah B, Ma CMC. On Monte Carlo modeling of megavoltage photon beams: A revisited study on the sensitivity of beam parameters. *Med Phys.* 2011;38(1):188-201.
44. Kawrakow I, Rogers DWO, Walters BRB. Large efficiency improvements in BEAMnrc using directional bremsstrahlung splitting. *Med Phys.* 2004;31(10):2883-2898.
45. Ahmad SB, Sarfehnia A, Paudel MR, Kim A, Hissoiny S, Sahgal A, et al. Evaluation of a commercial MRI linac based monte carlo dose calculation algorithm with GEANT4. *Med Phys.* 2016;43(2):894-907.

46. Mora GM, Maio A, Rogers DWO. Monte Carlo simulation of a typical  $^{60}\text{Co}$  therapy source. *Med Phys*. 1999;26(11):2494-2502.
47. Muir B, Xiong G, Selvam TP, Rogers DWO.  *$^{60}\text{Co}$  phase-space files generated using BEAMnrc*. Physics Department, Carleton University. CLRP-09-01, 2009.
48. Williams AJ, McEwen MR, DuSautoy AR. *A Calculation of the water to graphite perturbation factor ratios for the NACP type 02 ionisation chamber using Monte Carlo techniques*. National Physics Laboratory. NPL Report CIRM 13, 1998.
49. Panettieri V, Sempau J, Andreo P. Chamber-quality factors in  $^{60}\text{Co}$  for three plane-parallel chambers for the dosimetry of electrons, protons and heavier charged particles: PENELOPE Monte Carlo simulations. *Phys Med Biol*. 2008;53(21):5917-5926.
50. Erazo F, Brualla L, Lallena AM. Electron beam quality  $k_Q, Q_0$  factors for various ionization chambers: a Monte Carlo investigation with penelope. *Phys Med Biol*. 2014;59(21):6673-6691.
51. Gomà C, Andreo P, Sempau J. Monte Carlo calculation of beam quality correction factors in proton beams using detailed simulation of ionization chambers. *Phys Med Biol*. 2016;61(6):2389-2406.
52. Kawrakow I, Mainegra-Hing E, Tessier F, Walters BRB. *The EGSnrc C++ class library*. National Research Council Canada. NRCC Report PIRS-898, 2018.
53. Berger MJ, Coursey JS, Zucker MA, Chang J. *ESTAR, PSTAR, and ASTAR: Computer programs for calculating stopping-power and range tables for electrons, protons, and helium ions (version 2.0.1)* Gaithersburg, MD: National Institute of Standards and Technology; 2017. Available from: <https://www.nist.gov/pml/stopping-power-range-tables-electrons-protons-and-helium-ions>.
54. Jenkins TM, Nelson WR, Rindi A. *Monte Carlo Transport of Electrons and Photons*. New York: Plenum Press; 1988.

55. Ghila A, Steciw S, Fallone BG, Rathee S. Experimental verification of EGSnrc Monte Carlo calculated depth doses within a realistic parallel magnetic field in a polystyrene phantom. *Med Phys*. 2017;44(9):4804-4815.
56. Hughes HG. *Improved logic for sampling Landau straggling in MCNP5*. Mathematics and Computation, Supercomputing, Reactor Physics and Nuclear and Biological Applications; 2005 Sep 12-15; Avignon, France. LaGrange Park, IL: American Nuclear Society; 2005.
57. Reynaert N, Palmans H, Thierens H, Jeraj R. Parameter dependence of the MCNP electron transport in determining dose distributions. *Med Phys*. 2002;29(10):2446-2454.
58. Bull JS, Hughes HG, Walstrom PL, Zumbro JD, Mokhov NV. Magnetic field tracking with MCNP5. *Radiat Prot Dosim*. 2005;116(1-4):307-311.
59. Wulff J, Zink K, Kawrakow I. Efficiency improvements for ion chamber calculations in high energy photon beams. *Med Phys*. 2008;35(4):1328-1336.
60. Muir BR, Rogers DWO. Monte Carlo calculations of  $k_Q$ , the beam quality conversion factor. *Med Phys*. 2010;37(11):5939-5950.
61. Briesmeister JF. *MCNP<sup>TM</sup>-A general Monte Carlo N-particle transport code Version 4C*. Los Alamos National Laboratory. LA-13709-M, 2000.
62. Sheikh-Bagheri D, Rogers D. Monte Carlo calculation of nine megavoltage photon beam spectra using the BEAM code. *Med Phys*. 2002;29(3):391-402.
63. Koivunoro H, Siiskonen T, Kotiluoto P, Auterinen I, Hippeläinen E, Savolainen S. Accuracy of the electron transport in mcnp5 and its suitability for ionization chamber response simulations: a comparison with the egsnrc and penelope codes. *Med Phys*. 2012;39(3):1335-1344.
64. Poškus A. Evaluation of computational models and cross sections used by MCNP6 for simulation of electron backscattering. *Nucl Instrum Methods Phys Res B*. 2016;368:15-27.

65. Antoni R, Bourgois L. Evaluation of the new electron-transport algorithm in MCNP6. 1 for the simulation of dose point kernel in water. *Nucl Instrum Methods Phys Res B*. 2017;412:102-108.
66. Poon E, Verhaegen F. Accuracy of the photon and electron physics in GEANT4 for radiotherapy applications. *Med Phys*. 2005;32(6):1696-1711.
67. Agnew J, O'Grady F, Young R, Duane S, Budgell GJ. Quantification of static magnetic field effects on radiotherapy ionization chambers. *Phys Med Biol*. 2017;62(5):1731-1743.
68. Czarnecki D, Poppe B, Zink K. Monte Carlo-based investigations on the impact of removing the flattening filter on beam quality specifiers for photon beam dosimetry. *Med Phys*. 2017;44(6):2569-2580.
69. Attix FH, Roesch WC, Tochilin E. *Radiation dosimetry*: Academic Press; 1966.
70. Rikner G, Grusell E. General specifications for silicon semiconductors for use in radiation dosimetry. *Phys Med Biol*. 1987;32(9):1109-1117.
71. Butson MJ, Rozenfeld A, Mathur JN, Carolan M, Wong TP, Metcalfe PE. A new radiotherapy surface dose detector: the MOSFET. *Med Phys*. 1996;23(5):655-658.
72. McKeever S, Moscovitch M. On the advantages and disadvantages of optically stimulated luminescence dosimetry and thermoluminescence dosimetry. *Radiat Prot Dosim*. 2003;104(3):263-270.
73. Ken K. Optically stimulated luminescence dosimeters. *Health Phys*. 2001;81(2):108-109.
74. Andreo P, Burns DT, Hohlfeld K, Huq MS, Kanai T, Laitano F, et al. *Absorbed dose determination in external beam radiotherapy: an international code of practice for dosimetry based on standards of absorbed dose to water*. International Atomic Energy Agency. Vienna. Technical Report Series No. 398, 2000.

75. Novoselov KS, Geim AK, Morozov SV, Jiang D, Zhang Y, Dubonos SV, et al. Electric field effect in atomically thin carbon films. *Science*. 2004;306(5696):666-669.
76. Novoselov KS, Geim AK, Morozov S, Jiang D, Katsnelson M, Grigorieva I, et al. Two-dimensional gas of massless Dirac fermions in graphene. *Nature*. 2005;438(7065):197-200.
77. Neto AC, Guinea F, Peres NM, Novoselov KS, Geim AK. The electronic properties of graphene. *Rev Mod Phys*. 2009;81(1):109.
78. Mayorov AS, Gorbachev RV, Morozov SV, Britnell L, Jalil R, Ponomarenko LA, et al. Micrometer-scale ballistic transport in encapsulated graphene at room temperature. *Nano Lett*. 2011;11(6):2396-2399.
79. Lee C, Wei X, Kysar JW, Hone J. Measurement of the elastic properties and intrinsic strength of monolayer graphene. *Science*. 2008;321(5887):385-388.
80. Balandin AA. Thermal properties of graphene and nanostructured carbon materials. *Nature Mater*. 2011;10(8):569-581.
81. Nair RR, Blake P, Grigorenko AN, Novoselov KS, Booth TJ, Stauber T, et al. Fine structure constant defines visual transparency of graphene. *Science*. 2008;320(5881):1308-1308.
82. Bunch JS, Verbridge SS, Alden JS, Van Der Zande AM, Parpia JM, Craighead HG, et al. Impermeable atomic membranes from graphene sheets. *Nano Lett*. 2008;8(8):2458-2462.
83. Moser J, Barreiro A, Bachtold A. Current-induced cleaning of graphene. *Appl Phys Lett*. 2007;91(16):163513.
84. Bae S, Kim H, Lee Y, Xu X, Park J-S, Zheng Y, et al. Roll-to-roll production of 30-inch graphene films for transparent electrodes. *Nature Nanotechnol*. 2010;5(8):574.

85. Cha S, Cha M, Lee S, Kang JH, Kim C. Low-temperature, dry transfer-printing of a patterned graphene monolayer. *Sci Rep.* 2015;5:17877.
86. Berman B. 3-D printing: The new industrial revolution. *Bus Horiz.* 2012;55(2):155-162.
87. Crump SS, inventor. Apparatus and method for creating three-dimensional objects. U.S. Patent 5,121,329. 1992 Jun 9.
88. Li X, Cai W, An J, Kim S, Nah J, Yang D, et al. Large-area synthesis of high-quality and uniform graphene films on copper foils. *Science.* 2009;324(5932):1312-1314.
89. International Electrotechnical Commission. *Medical Electrical Equipment-Dosimeters with ionization chambers as used in radiotherapy.* International Electrotechnical Commission. Geneva, Switzerland. IEC Report No. 60731, 1997.
90. Andreo P, Almond P, Mattsson O, Nahum A, Roos M. *The use of plane parallel ionization chambers in high energy electron and photon beams. An international code of practice for dosimetry.* International Atomic Energy Agency. Stockholm, Sweden. IAEA Technical Report Series No. 381, 1995.
91. Park S, Kim Y, Kim H, Kang S, Ha J. Characteristics of the saturation curve of the ionization chambers in overlapping pulsed beams. *Nucl Instrum Methods Phys Res A.* 2006;566(2):706-712.
92. Funaro M, Sarno M, Ciambelli P, Altavilla C, Proto A. Real time radiation dosimeters based on vertically aligned multiwall carbon nanotubes and graphene. *Nanotechnol.* 2013;24(7):075704.
93. Kim HS, Park SH, Ha JH, Kim YK, Kim JK, Cho SY, et al. Operational characteristics of ionization chambers for a radiation monitoring. *J Nucl Sci Technol.* 2008;45(sup5):387-390.

## Abstract in Korean

방사선량 측정은 엑스레이의 발견 이후 중요한 문제로 여겨져 왔다. 요즘에는 PSDL 및 국제기구(예: IAEA, WHO)가 SSDL 네트워크를 통해 국제 교정 표준을 사용자에게 보급하고 있다. 이를 위해 다양한 선량계 및 장비가 교정 추적성 및 정확성의 품질을 보증하기 위해 개발되었다. 그 중에서 이온전리함은 높은 정밀성과 신뢰성으로 인해 방사선량의 측정에 가장 적합한 선량계가 되었다. 따라서 이온전리함은 방사선치료를 위한 기준 선량 교정을 제공하는데 사용되고 있다.

자기공명영상유도 방사선치료를 위한 선량측정은 의료방사선 분야에서 떠오르는 주제가 되었다. 현재 개발 중인 자기공명영상유도 방사선치료 장비는 입사 광자 빔에 수직 또는 평행한 0.35 - 1.5 T의 자기장을 갖는 Co-60 또는 펄스 엑스레이를 채택했다. 자기장은 로렌츠 힘의 작용을 통해 이차 하전 입자의 궤적에 영향을 미치므로 이온전리함 유효 부피 내의 방사선 분포가 변화될 수 있다. PSDL 또는 SSDL은 자기장 없이 이온전리함을 교정하기 때문에 자기장이 있는 환경에서 이온전리함을 이용한 방사선량 측정은 추가적인 자기장 보정 인자가 필요하다. 자기공명영상유도 방사선치료가 아직 개발 중이기 때문에 이러한 자기장 보정 인자들은 종종 전자기 모듈과 통합된 몬테카를로 방사선 전달 코드를 사용하여 계산된다.

0.35 에서 3.0 T의 정자기장에서 몬테카를로 코드의 전자 전달 알고리즘의 정확성을 평가하기 위해 0.01에서 3 MeV의 단일 에너지 전자에

대해 Fano 공동 정리를 테스트했다. 네 가지 범용 몬테카를로 코드들 (EGSnrc, PENELOPE, MCNP6, Geant4)이 검증되었다. PENELOPE와 MCNP6는 전달 매개 변수를 신중하게 선택할 경우 각각 1.0%와 0.4%의 정확도를 달성할 수 있었다. Geant4는 3.0 T를 제외하고는 1.7%이내의 정확도를 보였다. 향상된 전자기장 매크로를 가진 EGSnrc의 정확도는 0.2%이내였다. 이 뛰어난 정확도로 인해, 이 연구의 다음 시뮬레이션에서는 향상된 전자기장 매크로를 가진 EGSnrc가 사용되었다.

이 연구의 목적은 광자 빔의 다양한 에너지와 입사 광자 빔에 수직 또는 평행한 다양한 자기장 세기의 조합에 대한 이온전리함의 자기장 보정 인자를 계산하는 것이다. 평판형 이온전리함은 일반적으로 방사선치료를 위한 저에너지 빔에서 물 흡수선량을 측정하는데 사용된다. 이는 표면 물 흡수선량과 높은 선량 경사 범위의 선량을 측정하고 간편한 맞춤형 설계 및 제작에 유리하다. 세 종류의 상용화 평판형 이온전리함이 자기장이 있는 환경에서 반응 변화를 시뮬레이션 하기 위해 선택되었다. 여기에는 IBA사 NACP-02, PTW사 Roos(34001 타입) 및 Exradin A11이 포함되었다. 이 전리함들은 높이가 같지만 다른 반경의 유효 부피를 가진다. 방사선원의 경우 Co-60 빔을 위해 Eldorado 6와 6, 10 및 15 MV 광자 빔들을 위해 Varian사 Clinac<sup>®</sup> 시리즈가 채택되었다. 이전 연구에서 채택된 7 MV 광자 빔에 대한 스펙트럼 선원도 시뮬레이션 되었다. 자기장의 세기는 0.35 T에서 1.5 T로 광자 빔에 수직이거나 평행했다.

자기장이 있는 환경에서 평판형 이온전리함의 반응은 자기장이 없는

경우에 비해 최대 18% 증가했다. 평판형 이온전리함의 자기장 보정 인자는 0.85에서 1.0 사이였다. 수직 방향 자기장의 경우 큰 빔 선질 의존성 및 변동이 발생했다. 빔 선질이 클수록 작은 양의 자기장 보정이 필요했다. Co-60 빔을 제외하고 가장 큰 자기장 보정은 이 연구의 가장 큰 자기장 세기인 1.5 T가 아닌 약 1.0 T에서 발생했다. 수평 방향의 자기장의 경우 단지 1% 미만의 작은 자기장 보정이 필요했다.

이온전리함의 유효 부피를 분할한 몬테카를로 계산은 유효 부피 내 이차전자의 나선형 운동때문에 흡수 선량의 큰 이질성을 보여주었다. 유효 부피와 자기장 보정과의 관계를 파악하기 위해 Roos 챔버의 유효 부피 반경 또는 높이를 인위적으로 절반 또는 두 배로 수정하였다. 작은 유효 부피의 이온전리함이 자기장의 영향을 덜 받았다.